LEVEL

USAFA - TR - 78 - 6

AIR FORCE ACADEMY

AERONAUTICS DIGEST - SPRING 1978

JULY 1978

FINAL REPORT

APPROVED FOR PUBLIC RELEASE: DISTRIBUTION UNLIMITED

DEPARTMENT OF AERONAUTICS

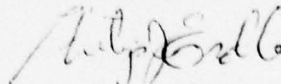DEAN OF THE FACULTY

UNITED STATES AIR FORCE ACADEMY

COLORADO 80840

78 10 19 057

This document is presented as a compilation of monographs worthy of publication. The United States Air Force Academy vouches for the quality of research, without necessarily endorsing the opinions and conclusions of the authors.

This digest has been cleared for open publication and/or public release by the appropriate Office of Information in accordance with AFR 190-17 and DODD 5230.9. There is no objection to unlimited distribution of this digest to the public at large, or by DDC to the National Technical Information Service.

This digest has been reviewed and is approved for publication.

PHILIP J. ERDLE, Colonel, USAF
Vice Dean of the Faculty

REPORT DOCUMENTATION PAGE		READ INSTRUCTIONS BEFORE COMPLETING FORM
1. REPORT NUMBER USAFA-TR-78-6	2. GOVT ACCESSION NO.	3. RECIPIENT'S CATALOG NUMBER
4. TITLE (and Subtitle) Air Force Academy Aeronautics Digest Spring 1978		5. TYPE OF REPORT & PERIOD COVERED Final Report.
		6. PERFORMING ORG. REPORT NUMBER
7. AUTHOR(s)		8. CONTRACT OR GRANT NUMBER(s)
9. PERFORMING ORGANIZATION NAME AND ADDRESS Department of Aeronautics United States Air Force Academy, CO 80840		10. PROGRAM ELEMENT, PROJECT, TASK AREA & WORK UNIT NUMBERS
11. CONTROLLING OFFICE NAME AND ADDRESS		12. REPORT DATE July 1978
		13. NUMBER OF PAGES
14. MONITORING AGENCY NAME & ADDRESS(if different from Controlling Office) 139 p.		15. SECURITY CLASS. (of this report)
		15a. DECLASSIFICATION/DOWNGRADING SCHEDULE

16. DISTRIBUTION STATEMENT (of this Report)

Approved for Public Release; Distribution Unlimited

D D C
OCT 23 1978
RECEIVED
F

17. DISTRIBUTION STATEMENT (of the abstract entered in Block 20, if different from Report)

18. SUPPLEMENTARY NOTES

19. KEY WORDS (Continue on reverse side if necessary and identify by block number)

Aerodynamics, Fluid Mechanics, Thermodynamics

20. ABSTRACT (Continue on reverse side if necessary and identify by block number)

This digest covers unclassified research in aeronautics performed at the
United States Air Force Academy during the 6 months ending 1 July 1978.
This report includes individual technical contributions in the specific
areas of Aerodynamics, Fluid Mechanics, and Thermodynamics and Heat Transfer.

PREFACE

This report is the first issue of the Air Force Academy Aeronautics Digest.
Future plans call for publication of the Digest twice a year. The contributions
represent recent work reported in a concise, scholarly and timely manner by students
and faculty of the Department of Aeronautics, members of other Academy departments
and F. J. Seiler Research Laboratory, researchers directly or indirectly connected
with USAFA-sponsored projects and authors in fields of interest to the USAFA. In
addition to complete papers, the Digest will include, when appropriate, abstracts of
lengthier reports and articles published in other formats. The editors will consider
for publication contributions in the general field of aeronautics, including:

> -Aeronautical Engineering
> --Flight Mechanics
> --Propulsion
> --Structures
> -Fluid Mechanics
> -Thermodynamics and Heat Transfer

Papers on other topics will also be considered on an individual basis. Contributions
should be sent to:

> Editor, Aeronautics Digest
> DFAN
> USAF Academy, CO   80840

In this first issue it seems appropriate to mention why publication of this digest
was started. As part of the normal Aeronautical Engineering curriculum, the Depart-
ment of Aeronautics sponsors a tremendous number of student projects. Many of these
projects are well worth permanent documentation for possible use in future research
programs. We also feel that the preparation of work in a concise, journal style is
conceptually valuable for those students whose work is worthy of publication. No
other outlet for student papers in aeronautics now exists.

In the Aeronautics Department, and, in fact, the U.S. Air Force Academy, many
faculty members are involved in formal research, and others work on academic problems
for use in the classroom or for personal clarification of some principle. In many
cases the formal researchers have acquired minor, secondary or preliminary results but
have not come to the point of preparing a project report. In the case of those invest-
igators of academic problems, many of their studies represent original work not prev-
iously published. While the extent of these studies may not warrant submission to a
professional journal, it is, nevertheless, important to retain a permanent record for
future use.

In discussing these points with Capt Donald Bishop of the Department of History, he suggested that the Aeronautics Department would do well to start its own journal. At the time the statement seemed humorous, but, as time passed, the idea seemed to make more and more sense. The result of Don's suggestion you now see before you. We hope that this issue will be the first of many more to come.

The Aeronautics Digest is edited by Capt E. J. Jumper, PhD and Capt M. J. Tower, PhD with the cooperation of the Department of English. In particular, the Digest would like to thank Capt K. E. Stevenson, Jr. who served as liaison officer from DFENG, gave many helpful suggestions and provided the final editorial review.

USAFA-TR-78-6

CONTENTS

SECTION I

AERODYNAMICS

AERODYNAMICS OF A TUMBLING REENTRY VEHICLE

Michael M. Tower[*]

Bertram Conroy[**]

Steven H. Slick[**]

Abstract

Experimental wind tunnel data is presented for a right conical blunt nosed model at angles of attack of $90°$, $135°$, and $180°$, through a mach number range of 1.2 to 3.0. The axial and normal force coefficients obtained from the tunnel data acquisition system are converted to lift and drag coefficients and extends the theoretical data published by the National Aeronautics and Space Administration, NASA, beyond the zero to $90°$ range. The results of this paper could be included in the aerodynamic routines of a ballistic trajectory reentry vehicle computer code for more accurate trajectory predictions of a tumbling reentry vehicle.

I. Introduction

With the advent of Intercontinental Ballistic Missiles, ICBM, to world political confrontation, defense of the continental United States becomes tremendously complex and expands the frontiers of technology. This paper addresses a small portion of the ICBM defense problem.

Consider the scenario of a first strike attack by Russia on the United States. Early warning radar will detect and tract the Russian ICBM's near their trajectory apogee, and linked with high speed computers with trajectory prediction codes, can determine point of impact in a matter of milliseconds. The known ballistic trajectory can then be integrated with an Antiballistic Missile, ABM, guidance control system to launch and intercept the ICBM. However, it is likely that several high altitude precursor nuclear weapons will be detonated to disrupt communications and blind radar. Added to this ABM detonations will further clutter the atmospheric war zone.

At first glance these air bursts should not bother the ABM system, since the trajectory of the ICBM was already determined by our early warning radars and trajectory predictions; unfortunately, associated with the atmospheric bursts are shock waves with pressure and density discontinuities. If a time staggered ICBM happens to intersect the shock waves of a previous detonation the trajectory will be significantly altered.

The ICBM reentry vehicle can skip off the high pressure behind the shock wave and

---

[*] Captain, USAF, Assistant Professor of Aeronautics, DFAN

[**] CIC, USAF Academy

unintentionally extend its range similar to the NASA fears that the Apollo Spacecraft
returning from the moon might skip off the Earth's dense atmosphere and be plummeted into
outer space. Alternatively, at the correct intersection angle and with the increased
drag due to the higher density, the reentry vehicle will fall short of its desired
target, see Figure 1.
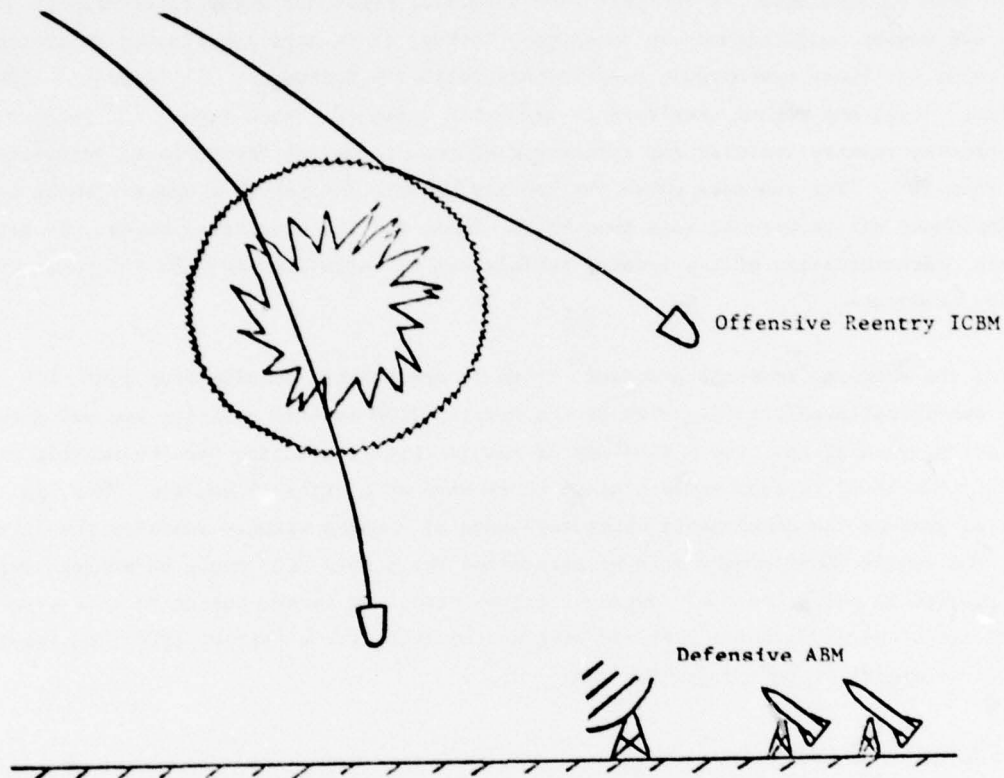
Figure 1. Modified Ballistic Trajectories due to Encounter with a
Nuclear Shock Wave

This signficantly complicates the ABM's guidance control. The ICBM's trajectory
has been modified (like a maneuverable ICBM) such that the ABM system can no longer
predict an intercept point. So   work has been done at the Air Force Weapons Laboratory,
Kirtland AFB, NM to couple a six-degree-of-freedom trajectory code with an atmospheric
nuclear burst model to predict modified trajectories for reentry vehicles that had
intersected the burst shock wave (Ref. 1). Good results were obtained in predicting
Circular Error Probabilities, CEP, for reentry vehicles passing through the influence
of a nuclear burst.

A key to any trajectory code is the vehicle aerodynamics. Accurate calculations of
lift, drag, and pitching moments are imperative. These parameters can alter the re-
entry angle and range. The lift, drag, and moment coefficients can be determined

theoretically or experimentally for a given shape as a function of angle of attack, Mach number and Reynolds number.

In the course of time, position stepping a trajectory code, angles of attack, Mach number and Reynolds number are known at the previous time interval and all parameters can be then extrapolated to the next time interval. Mach and Reynolds effects on lift, drag, and moment coefficients can be scaled, however it is more complicated theoretically to predict how these aerodynamic coefficients vary with incidence. It is well documented how lift, drag, and moment coefficients vary with angle of attack from $\pm 85^\circ$ (Ref. 2). For spinning reentry vehicles the gyroscopic effect limits the incidence to generally less than 10°. For the case where the reentry vehicle intersects a nuclear shock wave, the incidence will always be less than 90°. Thus, for the trajectory codes, the aerodynamic characteristics of the reentry vehicle can be calculated and the ballistic trajectory predicted.

For the original scenario proposed, there is one further complication that this paper specifically addresses. Many of the Russian ICBM reentry vehicles are not gyroscopically spinning and have a tendency to tumble (even a spinning reentry vehicle could possibly tumble if it encounters a blast shock wave at a critical angle). Thus, in order to predict the aerodynamic characteristics of Russian reentry vehicles the lift, drag, and moment coefficients must be determined for a full 360° angle of attack, rather than the widely published $\pm 85^\circ$ angle of attack data. It is the intent of this paper to relate experimental data for lift and drag coefficients for a Russian type ICBM reentry vehicle at angles of attack greater than $\pm 85^\circ$.

II. Experimental Approach

In order to obtain lift and drag coefficients from 90° to 180° incidence, solid aluminum models were designed and these were constructed by the Air Force Academy Instructional Technology Division. The model dimensions are depicted in Figure 2. The shapes are typical of the Russians SS-9 ICBM.
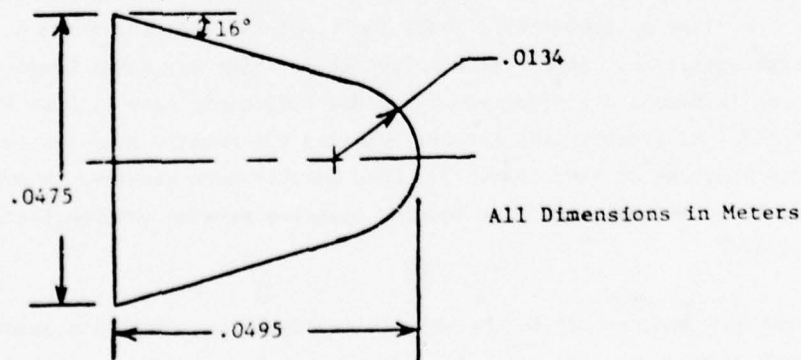
Figure 2: General Model Shape

4

The models were tested in the Air Force Academy Trisonic Wind Tunnel at various
incidences and Mach numbers. The sting in the tunnel is limited to $\pm 15°$ angle of attack,
thus it was necessary to attach the model at various angles while maintaining the sting
at a fixed horizontal orientation. The angles tested were $90°$, $135°$, and $180°$. See
Figures 3-5, which illustrate the reentry vehicle model orientations. The sting was
attached to a 75 lb_f balance that can measure lift, drag, and pitching moments. The
size of the models were governed by the balance limitations rather than wind tunnel test
section size, which is 1 ft by 1 ft.

Figure 3: Model orientation, $\alpha = 90°$.

To determine model size it was assumed that the greatest drag (axial) force would be
encountered for the $180°$ angle of attack, in other words, oriented rearwards into the
free stream. The base area of the model can be chosen by using the standard drag
equation:

$$D = C_D \; \tfrac{1}{2} \rho \, V^2 \, S \tag{1}$$

where   D = drag

C_D = drag coefficient

ρ = density

V = test section velocity

S = base reference area

Figure 4: Model orientation, $\alpha = 135°$

Figure 5: Model orientation, $\alpha = 180°$

6

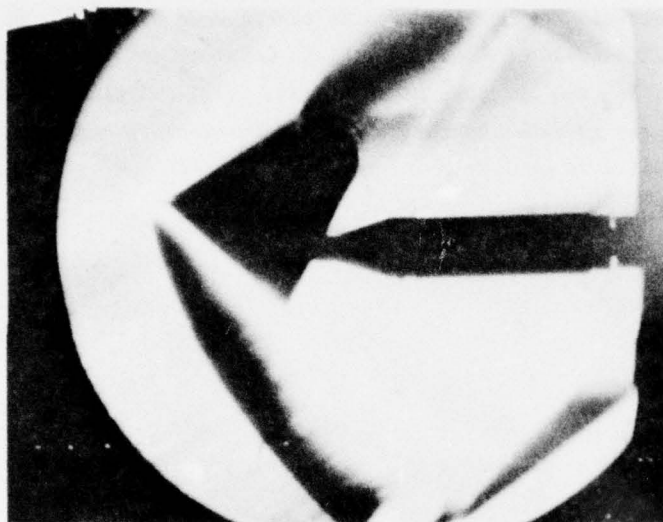Using the flat plate approximation for the base, the literature suggests a drag coefficient of 1.60 (Ref. 3). The drag was taken as 60% of the maximum allowable axial load of the balance, which is 334 N. The dynamic reference pressure, $\frac{1}{2} \rho V^2$, is established by tunnel operating conditions and can be obtained from a chart in the tunnel operation manual (Ref. 4) for the worst case, which was 91 KN/m^2. This determined a model base area of 0.177 square meters.

Testing was conducted at four Mach numbers for each of the three angles of attack. The Mach numbers tested were over the full supersonic range of the Trisonic Wind Tunnel from 1.2 to 3.0. The typical Mach number profile of a Russian SS-9 reentry vehicle is Mach 20 at 100 KM down to Mach one at impact. Thus the tests covered the low altitude reentry phase. Data was collected with the assistance of Fred Jayne during November 1977. The balance data was collected and automatically reduced by the Hewlett-Packard Data Acquisition System in conjunction with the Burroughs TC-500 computer.

III. Discussion of Results

The theoretical NASA data is tabulated for a sharp-nosed right cone at Mach 9.6. The NASA data thus had to be corrected for Mach effects and for cone bluntness to be compared with our model data. The following discussion and equations correct the data for Mach and geometric effects.

The axial and normal force coefficients, C_A and C_N, respectively, for the cone are plotted at Mach 9.6 and a stagnation pressure coefficient of 2.0 according to Newtonian Drag Theory. A better approximation for the stagnation pressure coefficient can be made for low supersonic Mach numbers, i.e., $M < 3$ by the following equation, (Ref. 2):

$$C_{p_{max}} = \frac{\gamma + 3}{\gamma + 1} \left(1 - \frac{2}{(\gamma + 3) M^2} \right) \tag{2}$$

where $\gamma - 1.4$ for air

M - free stream Mach number

To modify the tabulated NASA axial and normal force coefficients for Mach effects, each number is multiplied by the ratio:

$$\frac{C_{p_{max}}}{2} \tag{3}$$

where the numerator is determined from equation 2.

A blunt cone can be generated by superimposing the axial and normal force coefficents of a sharp right cone and a hemispherical shape. The superposition can be

7

achieved by the following equations (Ref. 2):

$$C_A = C_{A_{cone}} \left(1 - \frac{h}{a}^2\right) + C_{A_{sphere}} \left(\frac{h}{a}\right)^2 \sec^2 \theta_c \tag{4}$$

$$C_N = C_{N_{cone}} \left(1 - \frac{h}{a}^2\right) + C_{N_{sphere}} \left(\frac{h}{a}\right)^2 \sec^2 \theta_c \tag{5}$$

where C_A - axial force coefficient of sharp cone and hemisphere

 C_N - normal force coefficient of sharp cone and hemisphere

h, a and θ_c are given by figure 6.
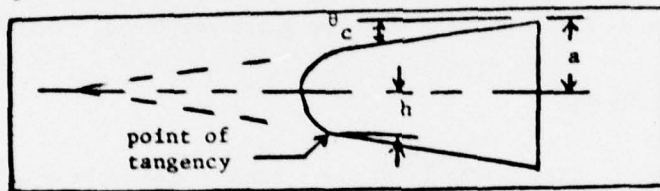
Figure 6: Definition of h, a, and θ_c

Once the axial and normal coefficients have been modified to reflect the blunt cone geometry, they can be resolved into lift and drag coefficients, C_L and C_D, respectively, by the following equations:

$$C_D = C_A \cos \alpha + C_N \sin \alpha \tag{6}$$

$$C_L = - C_A \sin \alpha + C_N \cos \alpha \tag{7}$$

where α - angle of attack.

The wind tunnel results are plotted in figures 7-13 along with the corrected theoretical data provided by NASA (Ref. 2). The theoretical data is plotted for angles of attack from zero to 85° and then the experimental data extends the curves from 90° to 180°. Both lift and drag coefficient data are presented.

The experimental data blends in quite well with the NASA theoretical data. The experimental data shows the highest drag when the model is pointed rearward into the flow which is what one would expect. The drag drops somewhat near the 90° incidence which is also plausible due to a reduction in base drag.

Figure 7: Drag coefficient versus angle of attack for Mach = 1.2

Figure 8: Drag coefficient versus angle of attack for Mach = 2.0

9

Figure 9: Drag coefficient versus angle of attack for Mach = 2.45

Figure 10: Drag coefficient versus angle of attack for Mach = 3.0

Figure 11: Lift coefficient versus angle of attack for
Mach = 1.2

Figure 12: Lift coefficient versus angle of attack for
Mach = 2.0

C_L

.4

.3

.2
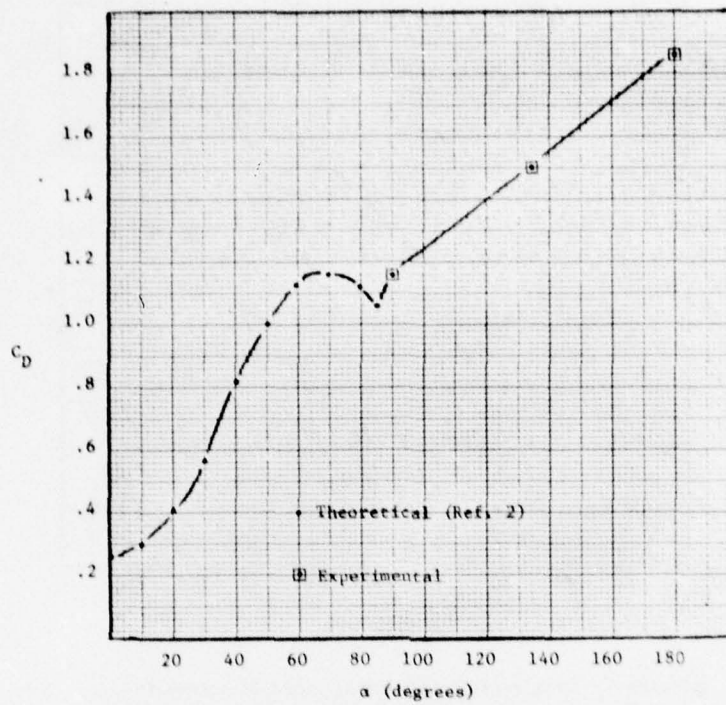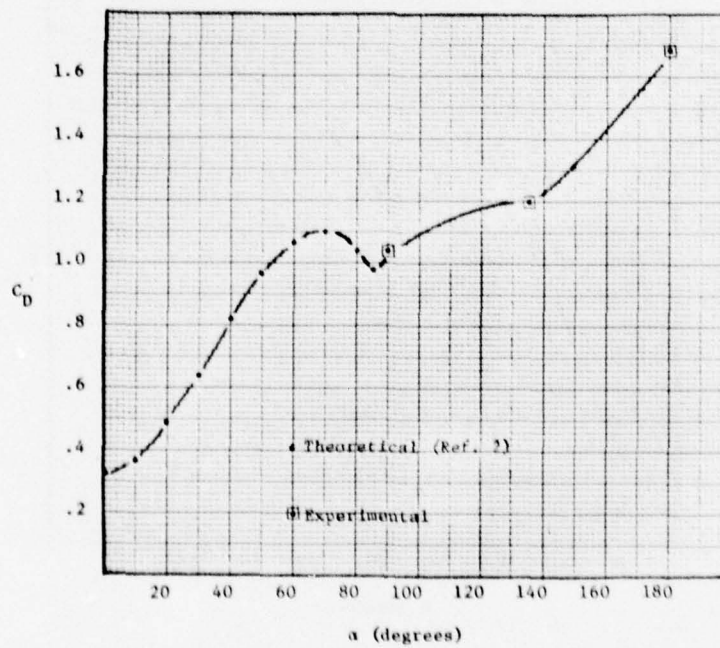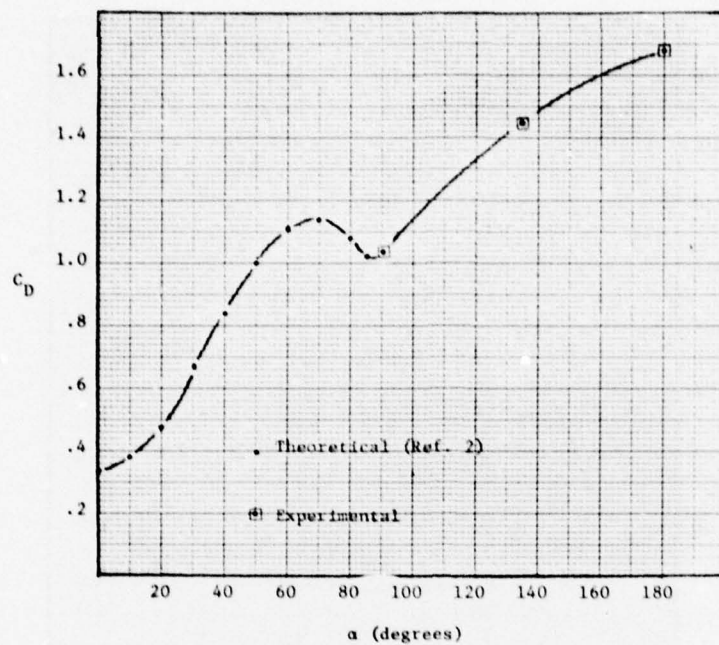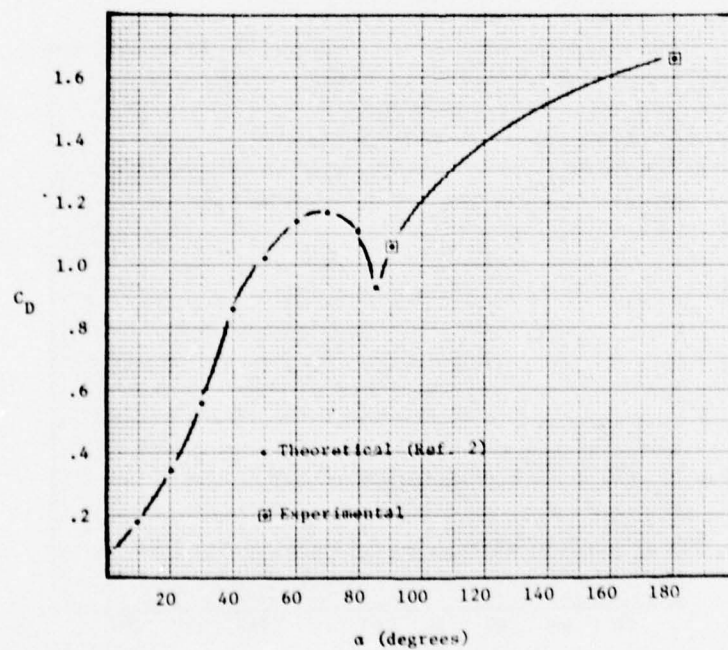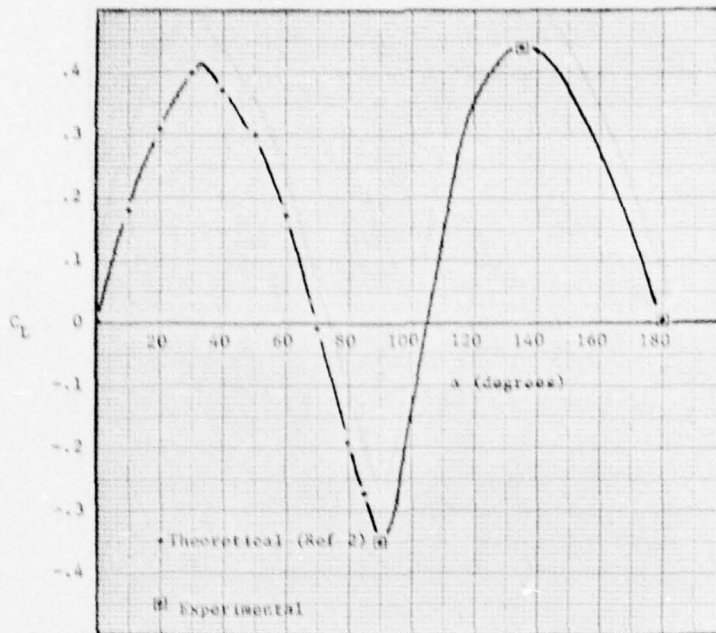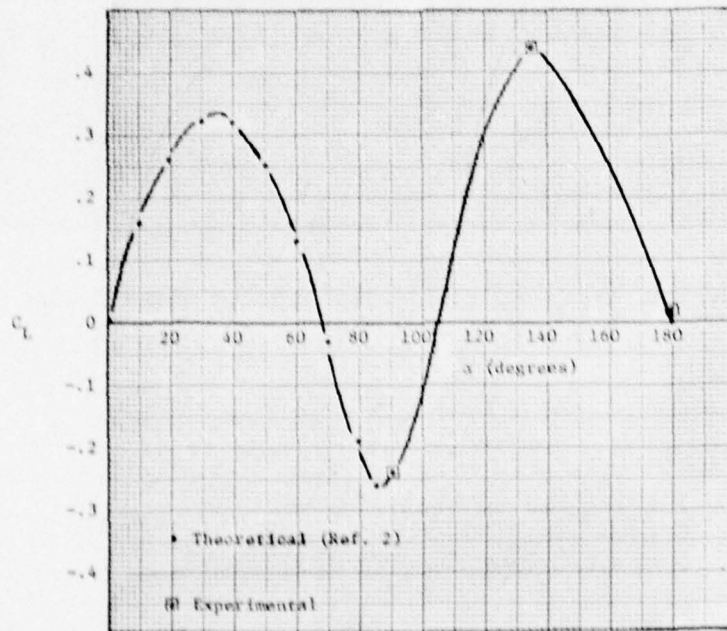
.1

0

-.1

-.2

-.3

-.4

20 40 60 80 100 120 140 160

α (degrees)

• Theoretical (Ref. 2)

⊞ Experimental
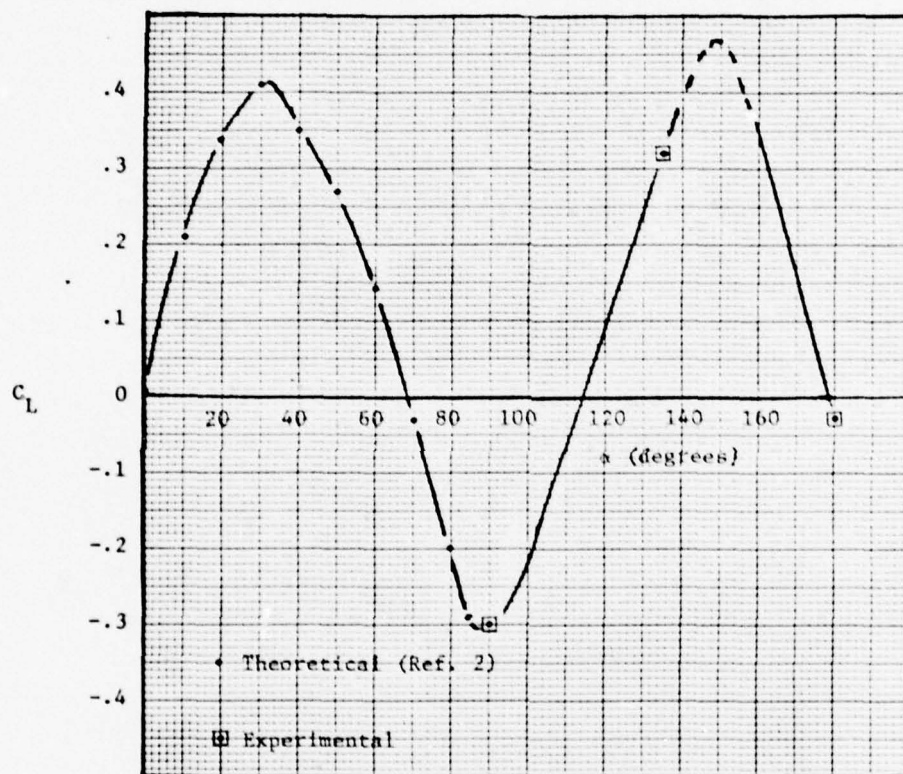
Figure 13: Lift coefficient versus angle of attack for
Mach = 3.0

The lift coefficient reaches a maximum near 135° angle of attack. This is a result of the large flat plate area of the base being exposed to the free stream. The lift coefficient is expected to return to zero at 180° incidence because of axial symmetry; the experimental data confirms this requirement.

IV. Conclusions

Although only three incident angles at four Mach numbers were tested, general conclusions can be drawn since we expect the experimental portion of the curves, plotted in figures 7-13, to join smoothly with NASA's theoretical data and to be drawn smoothly between points. The highest values of lift coefficients occur near 135° and the highest drag coefficients are obtained for a rearward orientation, 180° incidence.

The data contained in this paper can be used to predict lift and drag coefficients for a tumbling reentry vehicle. With a proper curve fit to the data, the results can be incorporated into the aerodynamic subroutine of a ballistic trajectory reentry code. More accurate results can then be obtained by including the reentry vehicle's orientation through a full 360°.

In the way of recommendations for further studies, more data points should be tested in the full range of angle of attack from zero to 180°, along with many more Mach numbers. Higher Mach number testing is required for the higher altitude portion of reentry where the Mach number is near 20.

References

1. Tower, M. M., "Ballistic Reentry Vehicle Trajectory Codes Coupled with the Low Altitude Multiple Burst (LAMB) Model", AFWL-DYT-TN-75-6, Kirtland AFB, NM, June 1975.

2. Wells, W. R. and Armstrong, W. O., "Tables of Aerodynamic Coefficients Obtained from Developed Newtonian Expressions for Complete and Partial Conic and Spheric Bodies at Combined Angles of Attack and Sideslip with some Comparisons with Hypersonic Experimental Data", NASA TR-R-127, Langley Research Center, Langley Station, VA, 1962.

3. Dommasch, D. O., Sherby, S. S., and Connolly, T. F., Airplane Aerodynamics , Pitman Publishing Company, New York, NY, 1957, pg 190.

4. "Subsonic and Trisonic Wind Tunnel Facilities", Department of Aeronautics, Air Force Academy, CO, 1976, pg 21.

DRAG REDUCTION THROUGH HIGHER WING LOADING
David L. Kohlman[*]

Abstract

Drag reduction of typical light aircraft is discussed in this paper. The principle means of drag reduction can be achieved by reducing the wing area, thus reducing parasite drag. Reducing wing area naturally involves other modifications if the aircraft is expected to have the same or better performance. The modification constraints and related configuration changes are addressed here, such as reduced span or chord, full span Fowler flaps, and the use of the recently developed general aviation airfoil developed by Whitcomb.

I. Introduction

The wing typically accounts for almost half of the wetted area of today's production light airplanes and approximately one-third of the total zero-lift or parasite drag. Thus the wing should be a primary focal point of any attempts to reduce drag of light aircraft with the most obvious configuration change being a reduction in wing area. Other possibilities involve changes in thickness, planform, and airfoil section.

This paper will briefly discuss the effects of reducing wing area of typical light airplanes, constraints involved, and related configuration changes which may be necessary.

II. Constraints and Benefits

The wing area of current light airplanes is determined primarily by stall speed and/or climb performance requirements. Table 1 summarizes the resulting wing loading for a representative spectrum of single-engine airplanes. The maximum lift coefficient with full flaps, a constraint on wing size, is also listed. Note that wing loading (at maximum gross weight) ranges between about 10 and 20 psf, with most 4-place models averaging between 13 and 17. Maximum lift coefficient with full flaps ranges from 1.49 to 2.15.

Clearly if $C_{L_{max}}$ can be increased, a corresponding decrease in wing area can be permitted with no change in stall speed. If total drag is not increased at climb speed, the change in wing area will not adversely affect climb performance either and cruise drag will be reduced.

Though not related to drag, it is worthy of comment that the range of wing loading in Table 1 tends to produce a rather uncomfortable ride in turbulent air, as every light-

---

[*]Professor, University of Kansas

14

Table 1

WING LOADING AND $C_{L_{max}}$ FOR TYPICAL SINGLE-ENGINE AIRCRAFT

Aircraft	W/S – PSF	$C_{L_{max}}$
Cessna 150	10.2	1.73
Cessna 172	13.2	2.15
Cessna 182	16.9	2.03
Cessna 210	21.7	2.01
Beech C23	16.8	1.89
Beech V35B	18.8	1.85
Grumman Tiger	17.1	1.92
Bellanca 300A	20.6	1.64
Mooney M20E	15.4	1.85
Piper PA-28-140	13.4	1.73
Piper PA-28-180	14.4	1.51
Piper PA-28-200R	15.6	1.49
Piper PA-32	19.5	1.92

Table 2

WING LOADING AND $C_{L_{max}}$ FOR TYPICAL TWIN-ENGINE AIRCRAFT

Aircraft	W/S – PSF	$C_{L_{max}}$
Beech Baron	25.6	1.42
Beech Duke	31.8	1.64
Beech Queen Air	29.9	1.78
Cessna 310	30.7	2.02
Cessna 402	32.2	2.02
Cessna 421	35.2	1.86
Piper Seneca II	21.9	1.80
Piper Navaho PA-31-350	30.6	1.66
Piper Navaho PA-31P-425	34.1	1.93

15

plane pilot is well aware. The only way to reduce this gust sensitivity is to increase wing loading.

Typically, wing loading tends to increase as performance (cruise speed) increases. This is particularly evident in Table 2 which presents data for twin-engine aircraft. But gust response is proportional to the ratio of calibrated cruise speed to wing loading $[V_c/(W/S)]$ and thus improvements in ride due to higher wing loading are partially, if not completely, offset by higher cruise speed.

It is also evident in Table 2 that even though wing loading is higher than for single-engine aircraft, it is translated directly into higher stall speeds. Twin-engine high lift systems produce virtually the same $C_{L_{max}}$ as shown in Table 1 for single-engine airplanes. Thus there appears to be an equal potential for reduction in wing area of single and twin-engine aircraft by employing improved high lift systems. How to achieve higher $C_{L_{max}}$ for light aircraft is discussed later.

But, assuming for a moment that improvements in $C_{L_{max}}$ are available, making higher wing loading possible for a given airplane or class of airplanes, it is important to consider how the wing area should be reduced. The easiest and most tempting way is by reducing span. Not only does this leave the inboard wing structure, mechanisms, and wing-body junction unchanged, but it reduces wing bending moments making possible a lighter wing. But reducing the span increases the span loading, thus reductions in parasite drag through a decrease in wing area are countered by an increase in induced drag.

On the other hand, reducing wing area by a decrease in wing chord decreases parasite drag almost in direct proportion to chord decrease, and if span remains constant there is virtually no change in induced drag. From an aerodynamic point of view this is most desirable, but it introduces possible structural and weight problems because aspect ratio increases while spar thickness and internal volume decrease if the same airfoil section is used.

To understand the potential and the constraints of drag reduction through wing area reduction, consider the following simplified analysis.

Assuming that the parasite drag coefficient and span efficiency factor remain unchanged, the parasite drag is directly proportional to wing area and induced drag is inversely proportional to the square of the span. Then the wing drag at any given flight condition may be written as:

$$D_W = D_{P_R} \frac{b\,c}{b_R c_R} + (D_{W_R} - D_{P_R}) \frac{b_R^2}{b^2} \tag{1}$$

16

where D_{P_R} is the reference wing profile drag; D_{W_R} is the total drag of the reference wing. The span and chord are denoted as b and c with a subscript R indicating reference values. For simplicity an untapered wing is assumed. Normalizing equation (1) with respect to the original reference wing drag, D_{W_R}, gives:

$$D = \frac{D_W}{D_{W_R}} = P \frac{bc}{b_R c_R} + (1 - P) \frac{b_R^2}{b^2} \tag{2}$$

where $P = \dfrac{D_{P_R}}{D_{W_R}}$, the ratio of parasite drag to total drag.

If only the wing chord is reduced, then the change in total normalized wing drag is

$$dD = P \frac{dc}{c_R} \tag{3}$$

Thus the percent reduction in total wing drag is equal to the percent reduction in chord length times the original ratio of parasite to total wing drag. Clearly, the benefits of wing area reduction increase with air speed.

Consider a typical light airplane with the following characteristics:

        Gross weight = 2800 pounds

        Aspect ratio = 7.4

        Wing area = 174 ft^2

        Drag coefficient of body and empennage, $C_{D_{o_{BVH}}}$ = 0.017

        Wing parasite drag coefficient, $C_{D_{o_W}}$ = 0.009

        Airplane efficiency factor, e = 0.75

        Cruise altitude = 8,000 ft

If only the chord is reduced, then, as shown in Reference 1, the resulting normalized total airplane drag, D_T, is shown in Figure 1. Although substantial drag reductions are possible, constraints are imposed by the requirement to cruise at a reasonably low lift coefficient and stall margin, and to keep stall speeds low enough for good take-off and landing performance. Even with these constraints, however, significant reductions in wing area, cruise drag, and gust response are possible for today's general aviation fleet.
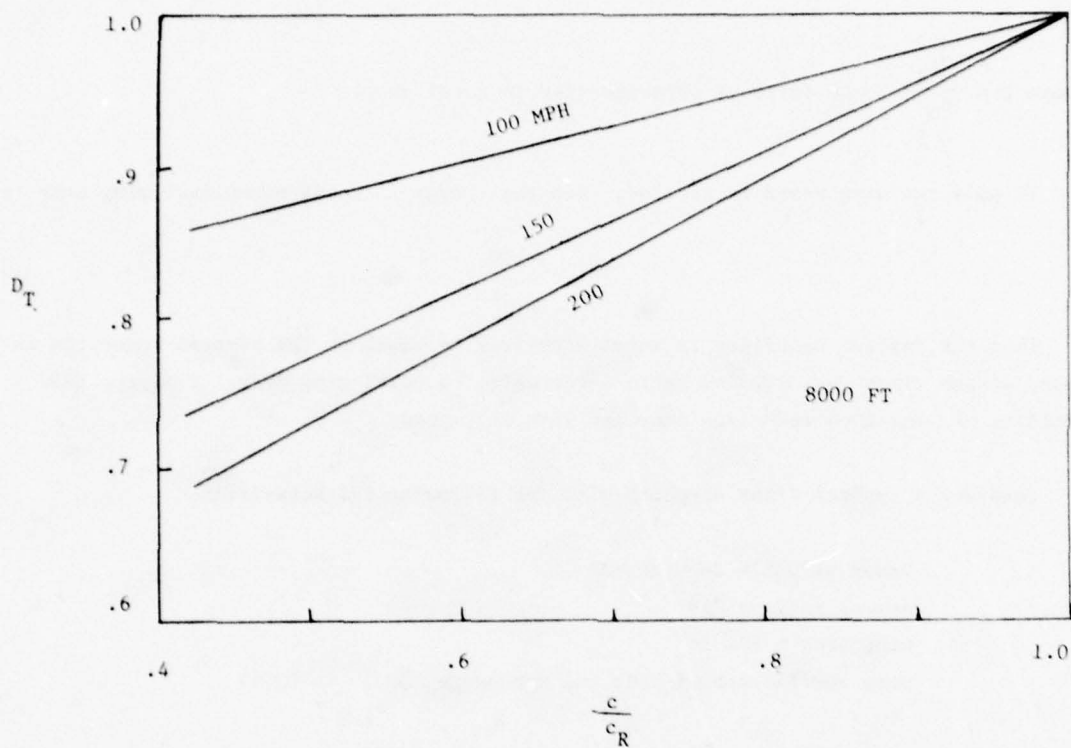
Figure 1. Effect of wing chord reduction on total drag
of a typical single-engine light aircraft.

To analyze the effect of reducing span while holding chord constant, differentiate equation (2) with respect to span b. Then

$$dD = \frac{1}{b_R} \left[P - 2 (1 - P) \frac{b_R^{\,3}}{b^3} \right] db \tag{4}$$

For decrease in span to result in a net decrease in drag the condition $\frac{dD}{db} > 0$ for $b * b_R$ must be satisfied.

This is true only if

$$P > \frac{2}{3} \tag{5}$$

In other words, a reduction in drag by reducing span can be achieved only if parasite drag is more than double the induced drag at the flight condition in question. While this may be satisfied during high speed cruise, it is rarely true during a climb. And when $P < 2/3$ a reduction in span increases induced drag more than it decreases parasite drag. For a tapered wing, P must be even larger than the value given in (5) to achieve drag reduction.

The limit to favorable span reduction is found by solving for the value of $\frac{b}{b_R}$ which yields $\frac{dD}{dB} = 0$, assuming $P > 2/3$. Again from equation (4) it is easily shown that

$$\frac{dD}{db} = 0$$

when $\left(\frac{b}{b_R} \right)^3 = \frac{2 (1 - P)}{P} \tag{6}$

Equation (6), plotted in Figure 2, establishes the boundary of favorable span reduction of a constant chord wing as a function of the reference wing parasite drag ratio, P.

III. Technical Developments

It is clear that wing area reduction can be achieved only if corresponding increases in $C_{L_{max}}$ can be designed into light airplanes in a practical manner. Several recent developments indicate that this is a very real possibility.

One promising development is a new family of general aviation airfoil sections. Two members of the family, the GA(W)-1 and GA(W)-2, have been defined at this time.
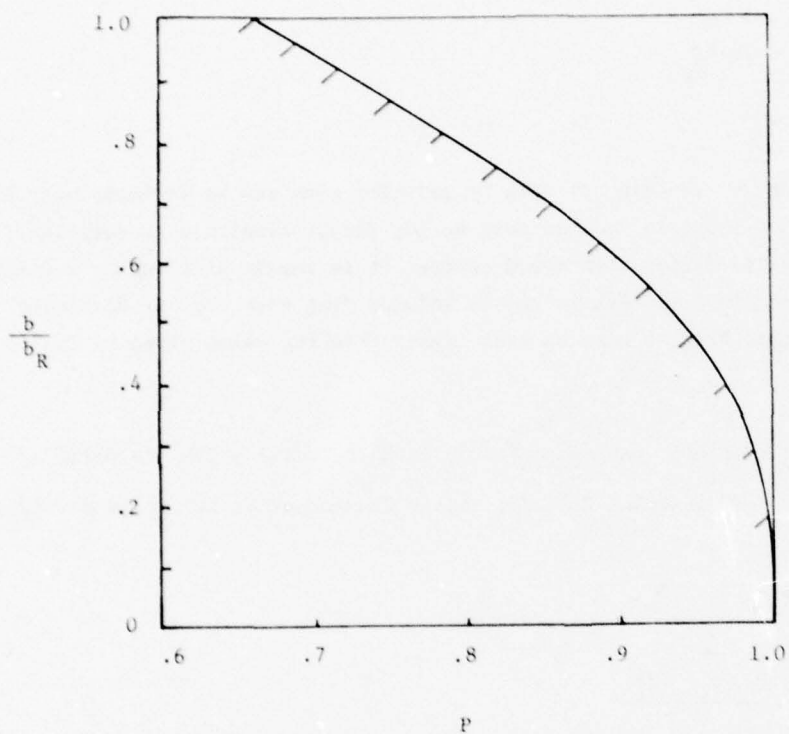
19

Figure 2. Limit of span reduction to decrease
drag as a function of parasite drag ratio.

As shown in Reference 2, the characteristics of these airfoils are:

- high $C_{L_{max}}$ compared to conventional airfoils (see Figure 3)
- gentle stall characteristics
- fairly thick section. The GA(W)-1 is 17% thick. This helps to maintain spar depth with reduced chord lengths.
- very little increase in C_{D_o} at climb lift coefficients (see Figure 4). This combined with decreased wing area offers the potential of significant increase in single-engine climb performance of twins.

Another interesting development is the recognition of the efficiency of spoilers for roll control on light airplanes. Among other features, spoilers permit the use of full-span, or at least increased span, flaps. This will increase $C_{L_{max}}$ with no change in airfoil or flap geometry. Several light airplanes are now using this concept: the advanced technology light twin (ATLIT), a modified Seneca; the Redhawk, a modified Cessna Cardinal; the RSTOL Seneca, a modification kit developed by Robertson Aircraft Corporation; and the Mitsubishi MU-2.

Another method of increasing $C_{L_{max}}$ is to increase the Fowler action of conventional single-slotted flaps. This can be done with very little increase in complexity or weight. Figure 5 shows the very large values of $C_{L_{max}}$ (2-D) which can be obtained with a GA(W)-1 airfoil using a 30% chord single-slotted Fowler flap.

IV. Flight Test Results

Additional confirmation of the ability to increase $C_{L_{max}}$ through both airfoil design and flap design has been demonstrated in the Redhawk and ATLIT programs.

Table 3 , from Reference 3, shows maximum lift coefficients obtained on the Redhawk by using a 30% chord single-slotted Fowler flap. Note that the flap covers only 47% of the wing span.

The ATLIT, using full-span, 30% chord single-slotted flaps, and a GA(W)-1 basic airfoil, generated the high lift data shown in Table 4 . Clearly, significant increases in $C_{L_{max}}$ are possible for this class of airplane.

Finally, Table 5 shows drag data generated during flight test of the Redhawk. The most significant result is that parasite drag was reduced 10.5% by reducing wing area, thickness, and span. This is a significant reduction, and it illustrates in flight that a reduction in wing area can be an effective and practical means of reducing drag.

21
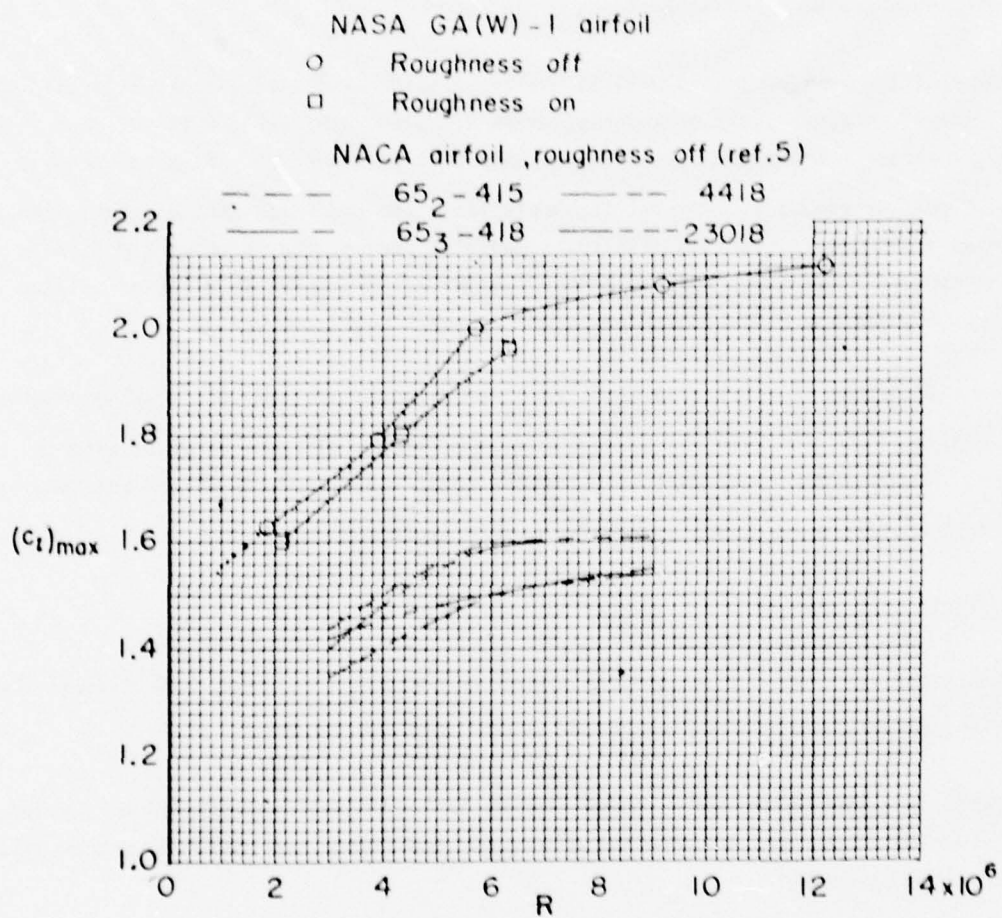
Figure 3. Variation of maximum section lift coefficeint with Reynolds number for various airfoils without flaps. M = 0.15.

NASA GA(W)-1 airfoil
   O   NASA standard roughness
   □   NACA standard roughness

NACA airfoil, NACA standard roughness (ref.5)
   — $65_2 - 415$
   — $65_3 - 418$
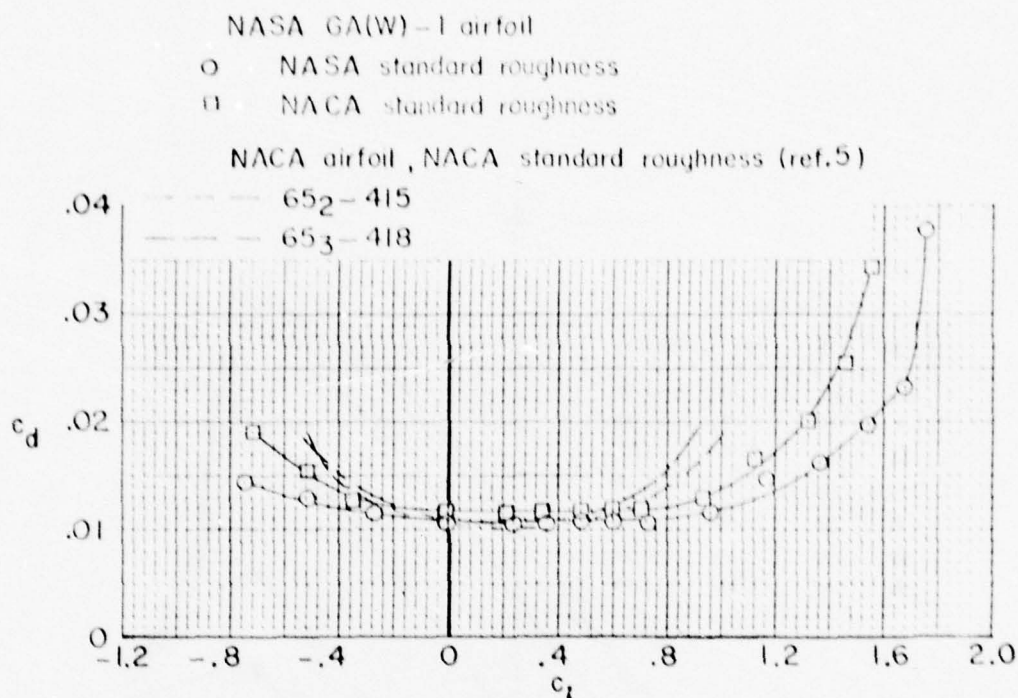
Figure 4. Comparison of section drag characteristics of NASA GA(W)-1 airfoil and NACA 65_2-415 and 65_3-418 airfoils. M = 0.20; R = 6 × 10⁶.

Table 3

COMPARISON OF STALL SPEEDS AND MAXIMUM LIFT COEFFICIENTS

Configuration	Redhawk		Cardinal	
	V_s, mph	$C_{L_{max}}$	V_s, mph	$C_{L_{max}}$
Cruise	79.6	1.40	64.7	1.35
Kruger flaps only	69.8	1.82	–	
Fowler flaps 10°	71.2	1.75	–	
Fowler flaps 10° and Kruger flaps	62.8	2.25	–	
Fowler flaps 40° (30° for Cardinal)	64.4	2.14	55.0	1.84
Fowler flaps 40° and Kruger flaps	56.0	2.83	–	

Notes: 1. Gross weight = 2500 lb

            2. Redhawk c.g. location 7.2% m.a.c. (109 in.)

            3. Cardinal c.g. location 19% m.a.c. (109.3 in.)
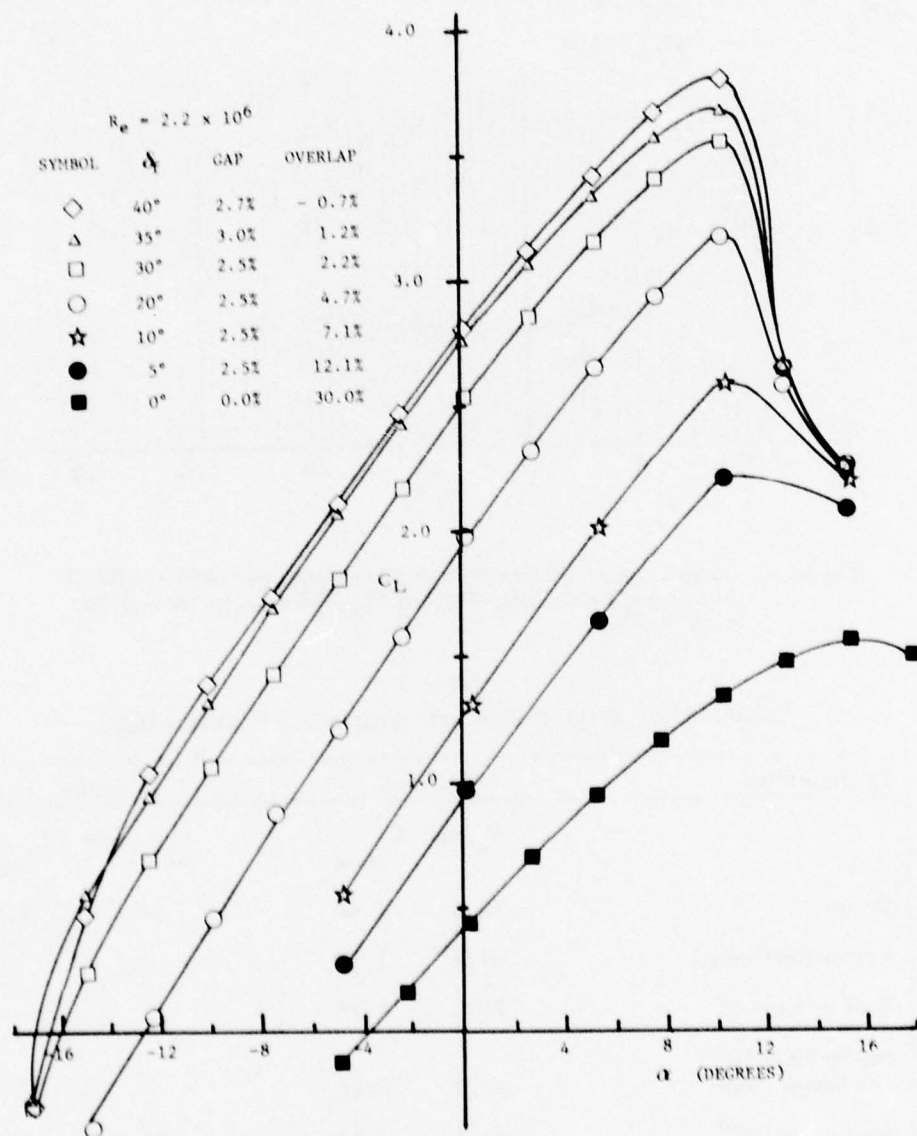
Figure 5. Lift performance of a 30% chord single-slotted Fowler flap on a GA(W)-1 airfoil.

24

Table 4

ATLIT PRELIMINARY STALL DATA

f	$V_{S_o} \sim MPH$	$C_{L_{max}}$
0	76	1.81
10°	66	2.40
20°	61.5	2.77
30°	59.3	2.98
40°	59.4	2.97

Gross weight = 4200 lb

Aft c.g. location

Table 5

COMPARISON OF DRAG CHARACTERISTICS DETERMINED FROM FLIGHT TEST

		C_{D_p}	$C_{D_p} S_w$
Cardinal	Cruise	0.0267	4.67
	Full Flaps	0.0462	8.08
Redhawk	Cruise	0.0380	4.18
	Full Fowler and Kruger Flaps	0.0788	8.67

References

1. Roskam, Jan, "Opportunities for Progress in General Aviation Technology," AIAA Paper No. 75-292, presented at AIAA 11th Annual Meeting and Technical Display, Washington, D. C., February 24-26, 1975.

2. McGhee, R. J., and Beasley, W. D., "Low Speed Aerodynamic Characteristics of a 17-Percent-Thick Airfoil Section Designed for General Aviation Applications, "NASA TN D-7428, December 1973.

3. Kohlman, David L., "Flight Test Results for an Advanced Technology Light Airplane Wing," SAE Paper No. 740368, presented at Business Aircraft Meeting, Wichita, Kansas, April 2-5, 1974.

TAKEOFF GROUND ROLL PERFORMANCE MODEL

Fred H. Porter III[*]

Abstract

An acceleration-during-takeoff-roll model is developed using two unknowns, a takeoff drag coefficient and a rolling friction coefficient. The unknown coefficients are then estimated using linear regression on acceleration versus velocity data obtained from four different takeoffs with varying thrust, weight and environmental conditions. Finally the model is used to predict acceleration, time and distance as a function of ground velocity for standard thrust, weight and environmental conditions.

I. Introduction

Traditionally the standard takeoff performance data of an aircraft has been evaluated

by applying individual, first-order corrections for non-standard power setting, weight,

temperature, pressure, and headwind. This method of evaluation provided an estimate of

performance on a sea level standard day for a specified power setting and aircraft con-

figuration. If performance was necessary under other than standard conditions the same

process was applied and, although tedious, produced reasonable results (Ref. 1).

By choosing a general linear model for takeoff acceleration as a function of ground

velocity, we can simplify the traditional procedure. Unknown drag and rolling friction

coefficients can be determined by using a least squares fit on test data for several

different takeoff conditions. We can determine the unknowns (drag coefficient and

rolling friction coefficient) in a general takeoff model. With these coefficients the

model may be used, within the limitations of the assumptions, to determine takeoff

acceleration, time, and distance quickly and explicity for any set of conditions.

II. The Linear Model

A. Assumptions

The model incorporates several assumptions as follows:

1. The aircraft remains at a constant lift and drag coefficient throughout the

ground roll. Constant landing-gear strut extension fixes the aircraft attitude and

---

[*]Lt Col, USAF, Assistant Professor of Aeronautics, DFAN

angle of attack, therefore it is not unreasonable to assume the operating point on the drag polar stays the same.

2. The runway slope is zero. (Test data used in this paper were taken on a zero-slope runway which simplified the regression; however, the model may be modified to accommodate runway slope.)

3. Net thrust is parallel to the velocity and remains constant throughout the take-off roll. Any dependence of thrust on velocity was assumed to be slight and was absorbed in the regression coefficients.

4. Aircraft weight and configuration remain constant throughout the takeoff roll.

5. Wind, ambient pressure and temperature remain constant throughout takeoff roll. Any side force component is negligible.

Figure 1. Forces During Takeoff Roll.
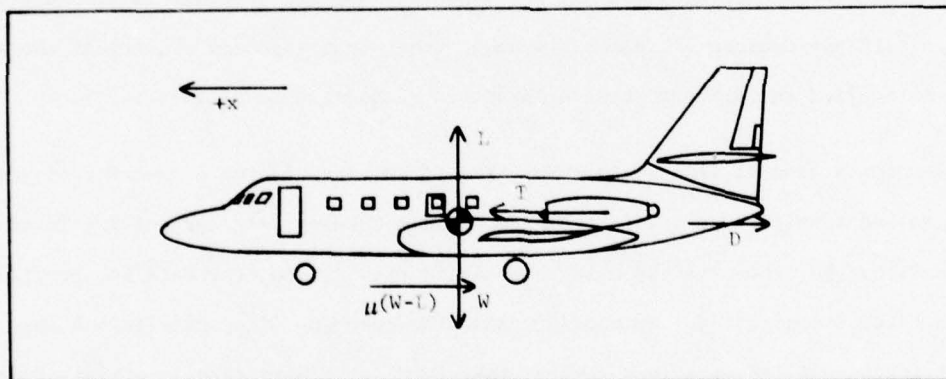
B. Equations

Under the assumptions of part A, the significant forces affecting an aircraft during takeoff roll are shown in Figure 1, where T is the net thrust, L is the lift, D is the drag, W is the aircraft weight, μ is the rolling friction coefficient, and x is the distance.

Summing the forces horizontally yields:

$$\frac{W}{g} \ddot{x} = T - D - \mu (W - L) \tag{1}$$

28

Using the usual definitions for lift and drag, Eqn (1) is solved for acceleration, $\ddot{x}$, yielding:

$$\ddot{x} = \frac{g}{W} \left(T - C_D \tfrac{1}{2} \rho V^2 S - \mu W + \mu C_L \tfrac{1}{2} \rho V^2 S \right) \qquad (2)$$

where g is the acceleration of gravity, C_D is the drag coefficient, ρ is the air density, V is the longitudinal component of air velocity relative to the aircraft, S is wing area, and C_L is the lift coefficient. Eqn (2) is rearranged to separate the unknown coefficients, and the parametric coefficient C_D' is substituted for $C_D - \mu C_L$.

$$\ddot{x} = \frac{g}{W} T - C_D' \frac{g \rho V^2 S}{2W} - \mu g \qquad (3)$$

The unknown coefficients, C_D' and μ , can be determined by linear regression using test data.

The longitudinal component of true air velocity is the sum of the aircraft ground speed, V_G , and headwind component, V_H , of the wind velocity. Using this sum Eqn (3) becomes :

$$\ddot{x} = \frac{g}{W} T - C_D' g \frac{\rho S}{2W} \left(V_G^2 + 2 V_G V_H + V_H^2 \right) - \mu g \qquad (4)$$

yielding a statement of acceleration as a function of ground velocity and headwind for the takeoff roll.

III. Regression Coefficients

The resulting coefficients of the regression process, C_D' and μ , are determined by fitting one or more sets of takeoff data composed of pairs of observed accelerations $\ddot{x}_i$ and ground velocities V_{G_i} . Eqn (4) is rearranged as follows :

$$\frac{T}{W} - \frac{\ddot{x}}{g} = C_D' \frac{\rho S}{2W} \left(V_G^2 + 2 V_G V_H + V_H^2 \right) + \mu \qquad (5)$$

New variables, a_i and b_i , are assigned for simplification.

$$a_i = \frac{T}{W} - \frac{\ddot{x}_i}{g}$$

29

and

$$b_i = \frac{\rho S}{2W} \left(V_{G_i}^2 + 2 V_{G_i} V_H + V_H^2 \right)$$

In terms of a_i and b_i each observation can be expressed accordingly as:

$$a_i = C_D' b_i + \mu \qquad (6)$$

The set of equations, then, for n observations is:

$$a_1 = C_D' b_1 + \mu \qquad (7)$$
$$a_2 = C_D' b_2 + \mu$$
$$\vdots \qquad \vdots \qquad \vdots$$
$$a_n = C_D' b_n + \mu$$

In matrix notation let

$$A = \begin{bmatrix} a_1 \\ a_2 \\ \vdots \\ a_n \end{bmatrix} \quad \text{and} \quad B = \begin{bmatrix} b_1 & 1 \\ b_2 & 1 \\ \vdots & \vdots \\ b_n & 1 \end{bmatrix}$$

and Eqns (7) become

$$A = B \begin{bmatrix} C_D' \\ \mu \end{bmatrix} \qquad (8)$$

The least squares solution of Eqn (8) is (Ref. 2)

$$\begin{bmatrix} C_D' \\ \mu \end{bmatrix} = \begin{bmatrix} B^T B \end{bmatrix}^{-1} B^T A \qquad (9)$$

IV. General Takeoff Performance

Once the unknown coefficients have been determined by linear regression as described in section III, Eqn (4) can be used to make predictions of takeoff performance. A more convenient form of Eqn (4) for prediction purposes is:

$$\ddot{x} = - \frac{C_D' g \rho S}{2W} V_G^2 - \frac{C_D' g \rho S V_H}{W} V_G - \frac{C_D' g \rho S}{2W} V_H^2 - \mu g + \frac{g}{W} T \qquad (10)$$

30

Since the third, fourth, and fifth terms remain constant for a given takeoff prediction Eqn (10) can be written

$$\ddot{x} = aV_G^2 + bV_G + c \tag{11}$$

where a, b, and c represent the appropriate constants.

The takeoff time t is determined by integration of Eqn (11). Since

$$\ddot{x} = \frac{dV_G}{dt}$$

then

$$\int dt = \int \frac{dV_G}{aV_G^2 + bV_G + c}$$

after integration (Ref. 3)

$$t_2 - t_1 = \frac{-2}{\sqrt{b^2 - 4ac}} \tanh^{-1} \left[\frac{2cV_G + b}{\sqrt{b^2 - 4ac}} \right] \Bigg|_{V_{G_1}}^{V_{G_2}} \tag{12}$$

The takeoff distance is determined in a similar manner. Since

$$\frac{dx}{dt} = V_G$$

then

$$\int dx = \int \frac{V_G dV_G}{aV_G^2 + bV_G + c}$$

and the integrated expression is :

$$x_2 - x_1 = \frac{1}{2c} \ln \left[aV_G^2 + bV_G + c \right] \Bigg|_{V_{G_1}}^{V_{G_2}} - \frac{b}{2c} (t_2 - t_1) \tag{13}$$

31

V. Comparison of Model and Data

Velocity and acceleration pairs from four observed takeoffs are shown in Figure 2. These data were recorded during takeoff tests on a Lockheed C-140 Jetstar during a flight evaluation conducted at Edwards AFB in August 1961 (Ref. 4). Different combinations of aircraft gross weight, ambient temperature, ambient pressure, and surface wind occurred for each test, and these data were used to determine the best regression coefficients C_D' and μ. The predictions of the resulting model are also shown in Figure 2. Details of each data set and information on the "goodness of fit" are contained in the Appendix.
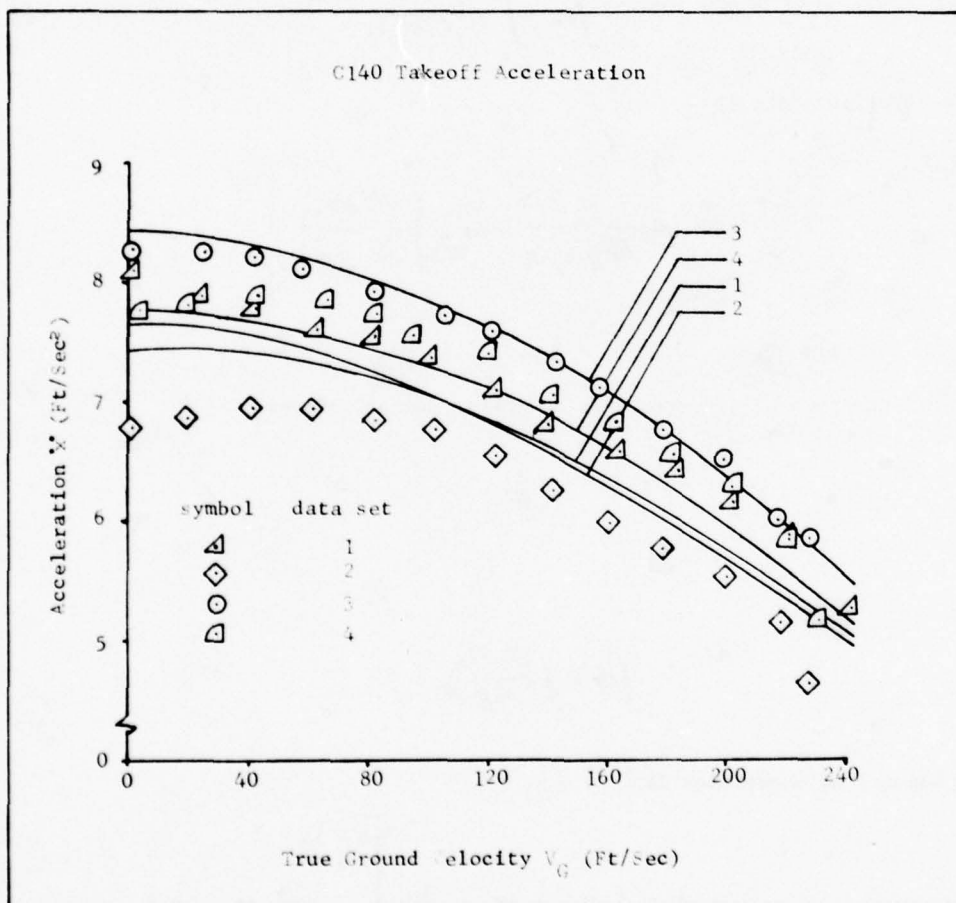

Figure 2. C 140 Takeoff Acceleration

32

The uncertainty of the average takeoff thrust is clearly evident in Figure 2. The thrust-level had not stabilized on data set 2 until nearly lift-off speed. It is quite possible that throttle adjustments were made after break release. In spite of the uncertainties the takeoff roll can be predicted quite accurately. Table 1 compares the takeoff roll predicted by the model to that predicted by the usual data reduction method used at Edwards AFB (Ref. 1).

Table 1

Comparison of C 141 Takeoff Performances

Parameter	Model Prediction	Reference 4 Prediction
takeoff ground roll*	3840 feet	3870 feet
takeoff time*	31 secs	N/A

*Predictions are based on sea level standard day conditions, no wind, no runway slope, an aircraft gross weight of 40,000 lb_f, a net thrust of 2,825 lb_f per engine, and a lift-off true ground speed of 135 knots.

VI. Conclusions and Recommendations

A reasonably accurate model for prediction of takeoff acceleration, time, and distance can be made by estimating drag coefficient and rolling friction coefficient from observed velocity and acceleration data. The model can be used to predict performance under a variety of takeoff conditions with equal ease.

This method of modeling should be evaluated extensively on other data from tests on different aircraft.

The following applications are suggested:

1. This model should be included in flight handbooks in equation form for direct computation of takeoff performance.

2. The model should be programmed into inertial measuring systems on board aircraft. The takeoff predictions could be computed in a "take-off mode" during takeoff roll to provide the pilot continued comparison of actual performance versus estimated. Decisions

33

to abort could be made early significantly reducing the accident rate.

3. The model should be installed as in recommendation 2 to reduce fuel comsumption, thrust used, and engine wear on takeoff. With accurate takeoff predictions displayed to the pilot the throttles could be set to the minimum thrust level required to achieve a safe takeoff. This would increase engine life, save fuel, and reduce the risk of engine failure.

References

1. Lush, Kenneth J.,"Standarization of Take-off Performance Measurements for Airplanes," Technical Note R-12, Air Force Flight Test Center, Edwards, California.

2. Neter, J. and Wasserman, W., Applied Linear Statistical Models, Richard D. Irwin Inc., Homewood Ill, 1974.

3. Selby, Samuel M., CRC Standard Mathmatical Tables, The Chemical Rubber Co., Cleveland, 1967.

4. Myers, R. H. and Cross, C. S., "C-140 Jetstar Flight Evaluation", Report No 62-24, Air Force Flight Test Center, Edwards AFB, California, 1963.

OBSERVED AND COMPUTED TAKEOFF DATA

DATASET 1
AMBIENT TEMPERATURE (DEG C): 19
BAROMETRIC PRESSURE (IN HG): 27.540
WIND VELOCITY (KNOTS): 3.5
WIND DIRECTION (DEG): 240
AIRCRAFT HEADING (DEG): 040
AVG PTS (IN HG): 55.5
SL GROSS THRUST FOR EPR (LBF) 2.015: 2745
ACTUAL TOTAL THRUST: 10106
THRUST PER ENGINE: 2527
TAKE OFF GROSS WEIGHT (LBF): 39972

	------OBSERVED------			----------------COMPUTED-----------------	
VELOCITY	ACCEL	A	B	ACCEL	ERROR
(FT/SEC)	(FT/SEC↑2)	VECTOR	VECTOR	(FT/SEC↑2)	
.6	8.09	.0014	.0004	7.42	-.6698
8.5	8.03	.0033	.0001	7.42	-.6092
16.5	7.96	.0054	.0018	7.42	-.5439
24.4	7.90	.0073	.0052	7.41	-.4939
32.3	7.84	.0092	.0105	7.39	-.4492
40.1	7.77	.0113	.0175	7.37	-.3995
47.9	7.72	.0129	.0263	7.35	-.3749
55.5	7.66	.0148	.0365	7.32	-.3447
63.2	7.62	.0150	.0487	7.28	-.3399
70.8	7.58	.0172	.0623	7.24	-.3395
78.3	7.54	.0185	.0775	7.20	-.3434
85.9	7.49	.0200	.0945	7.15	-.3428
93.3	7.44	.0218	.1128	7.09	-.3456
100.8	7.37	.0238	.1328	7.04	-.3339
108.1	7.29	.0263	.1540	6.97	-.3152
115.4	7.19	.0294	.1767	6.91	-.2910
122.5	7.09	.0325	.2003	6.84	-.2494
129.6	6.99	.0356	.2253	6.77	-.2220
136.5	6.89	.0387	.2511	6.69	-.1967
143.3	6.80	.0415	.2779	6.62	-.1843
150.0	6.73	.0437	.3055	6.54	-.1945
156.7	6.66	.0458	.3345	6.45	-.2086
163.4	6.60	.0477	.3649	6.36	-.2365
169.9	6.54	.0496	.3955	6.27	-.2654
176.5	6.48	.0514	.4279	6.18	-.2993
182.9	6.42	.0533	.4606	6.09	-.3340
189.3	6.35	.0555	.4944	5.99	-.3621
195.6	6.27	.0580	.5289	5.89	-.3820
201.9	6.18	.0608	.5645	5.78	-.3954
208.0	6.07	.0642	.6002	5.68	-.3896
214.1	5.92	.0688	.6369	5.57	-.3451
220.0	5.75	.0741	.6734	5.47	-.2810
225.7	5.57	.0797	.7097	5.36	-.2062
231.0	5.42	.0844	.7443	5.26	-.1564
232.4	5.39	.0853	.7536	5.24	-.1533
236.3	5.31	.0878	.7797	5.16	-.1490
241.7	5.24	.0900	.8166	5.05	-.1861
242.9	5.20	.0912	.8249	5.03	-.1702
246.9	5.07	.0953	.8530	4.95	-.1215
249.5	4.98	.0980	.8714	4.89	-.0850

*DRAG COEFFICIENT .09010, ROLLING FRICTION COEFFICIENT .02217

35

DATASET 2
AMBIENT TEMPERATURE (DEG C): 33
BAROMETRIC PRESSURE (IN HG): 27.540
WIND VELOCITY (KNOTS): 6.9
WIND DIRECTION (DEG): 180
AIRCRAFT HEADING (DEG): 220
AVG PTS (IN HG): 53.5
SL GROSS THRUST FOR EPR (LBF) 1.943: 2581
ACTUAL TOTAL THRUST: 9502
THRUST PER ENGINE: 2376
TAKE OFF GROSS WEIGHT (LBF): 36561

!--------OBSERVED-------!		!---------------COMPUTED--------------!		
VELOCITY	ACCEL	A	B	ACCEL	ERROR
(FT/SEC)	(FT/SEC↑2)	VECTOR	VECTOR	(FT/SEC↑2)	
.6	6.79	.0489	.0014	7.64	.8548
6.2	6.81	.0482	.0035	7.64	.8237
13.1	6.84	.0473	.0074	7.63	.7873
19.9	6.87	.0464	.0127	7.61	.7420
26.8	6.90	.0454	.0195	7.59	.6923
33.7	6.92	.0448	.0278	7.57	.6483
40.6	6.94	.0442	.0375	7.54	.6002
47.6	6.95	.0439	.0488	7.51	.5573
54.6	6.94	.0442	.0616	7.47	.5301
61.5	6.92	.0448	.0758	7.43	.5092
68.5	6.89	.0458	.0916	7.38	.4933
75.3	6.86	.0467	.1084	7.33	.4747
82.1	6.84	.0473	.1266	7.28	.4419
88.9	6.81	.0482	.1462	7.23	.4150
95.8	6.79	.0489	.1675	7.16	.3731
102.6	6.76	.0498	.1980	7.10	.3380
109.3	6.72	.0510	.2135	7.03	.3098
116.1	6.66	.0529	.2388	6.96	.2966
122.7	6.57	.0557	.2647	6.88	.3115
129.2	6.47	.0588	.2915	6.80	.3339
135.7	6.37	.0619	.3195	6.72	.3525
141.9	6.26	.0653	.3475	6.64	.3814
148.2	6.15	.0688	.3772	6.56	.4055
154.2	6.06	.0716	.4065	6.47	.4104
160.3	5.98	.0740	.4375	6.38	.4006
166.2	5.90	.0765	.4685	6.29	.3906
172.0	5.83	.0787	.5001	6.20	.3691
177.8	5.77	.0806	.5326	6.10	.3347
183.6	5.71	.0824	.5662	6.01	.2973
186.3	5.66	.0840	.5822	5.96	.3009
194.9	5.60	.0859	.6347	5.81	.2089
200.5	5.54	.0877	.6700	5.71	.1664
205.9	5.47	.0899	.7050	5.60	.1350
211.4	5.38	.0927	.7416	5.50	.1190
216.8	5.20	.0983	.7734	5.39	.1923
218.1	5.13	.1005	.7874	5.37	.2362
221.9	4.95	.1061	.8140	5.29	.3392
226.9	4.62	.1163	.8496	5.19	.5659

*DRAG COEFFICIENT .09010, ROLLING FRICTION COEFFICIENT .02217

```
DATASET 3
AMBIENT TEMPERATURE (DEG C): 16
BAROMETRIC PRESSURE (IN HG): 27.610
WIND VELOCITY (KNOTS): 5.2
WIND DIRECTION (DEG): 180
AIRCRAFT HEADING (DEG): 220
AVG PT5 (IN HG): 56.1
SL GROSS THRUST FOR EPR (LBF) 2.032: 2789
ACTUAL TOTAL THRUST: 10294
THRUST PER ENGINE: 2574
TAKE OFF GROSS WEIGHT (LBF): 36278
```

	------OBSERVED------			-------------COMPUTED-------------	
VELOCITY	ACCEL	A	B	ACCEL	ERROR
(FT/SEC)	(FT/SEC↑2)	VECTOR	VECTOR	(FT/SEC↑2)	
.7	8.27	.0267	.0009	8.41	.1437
8.9	8.26	.0270	.0040	8.40	.1448
17.2	8.26	.0270	.0094	8.39	.1292
25.5	8.25	.0273	.0170	8.37	.1171
33.7	8.23	.0280	.0267	8.34	.1089
41.9	8.21	.0286	.0386	8.30	.0943
50.2	8.17	.0298	.0538	8.26	.0928
58.4	8.12	.0314	.0693	8.22	.0954
66.5	8.05	.0336	.0876	8.16	.1123
74.5	7.98	.0357	.1078	8.10	.1238
82.4	7.91	.0379	.1298	8.04	.1300
90.3	7.84	.0401	.1538	7.97	.1303
98.1	7.77	.0423	.1796	7.90	.1257
105.8	7.71	.0441	.2069	7.82	.1065
113.5	7.64	.0463	.2362	7.73	.0916
121.1	7.58	.0482	.2670	7.64	.0622
128.6	7.50	.0507	.2993	7.55	.0487
136.1	7.42	.0531	.3334	7.45	.0299
143.5	7.32	.0562	.3688	7.35	.0272
150.8	7.21	.0597	.4055	7.24	.0307
157.9	7.10	.0631	.4429	7.13	.0324
165.0	6.97	.0671	.4819	7.02	.0492
171.9	6.86	.0705	.5215	6.90	.0447
178.7	6.75	.0740	.5619	6.79	.0374
185.4	6.66	.0768	.6033	6.67	.0075
191.9	6.58	.0792	.6448	6.55	⁻.0328
198.5	6.50	.0817	.6883	6.42	⁻.0791
204.9	6.40	.0848	.7319	6.29	⁻.1055
211.4	6.28	.0886	.7776	6.16	⁻.1178
217.7	6.00	.0973	.8231	6.03	.0301
220.8	5.79	.1038	.8460	5.96	.1737
223.6	5.42	.1153	.8670	5.90	.4830
227.6	4.84	.1333	.8974	5.81	.9749

*DRAG COEFFICIENT .09010, ROLLING FRICTION COEFFICIENT .02217

DATASET 4
AMBIENT TEMPERATURE (DEG C): 16.5
BAROMETRIC PRESSURE (IN HG): 27.610
WIND VELOCITY (KNOTS): 1.7
WIND DIRECTION (DEG): 240
AIRCRAFT HEADING (DEG): 040
AVG PTS (IN HG): 55.9
SL GROSS THRUST FOR EPR (LBF) 2.025: 2730
ACTUAL TOTAL THRUST: 10076
THRUST PER ENGINE: 2519
TAKE OFF GROSS WEIGHT (LBF): 38391

	------OBSERVED------		---------------COMPUTED---------------			
VELOCITY	ACCEL	A	B	ACCEL	ERROR
(FT/SEC)	(FT/SEC↑2)	VECTOR	VECTOR	(FT/SEC↑2)	
3.7	7.75	.0216	.0000	7.73	⁻.0187
11.5	7.79	.0203	.0012	7.73	⁻.0621
19.3	7.82	.0194	.0043	7.72	⁻.1010
27.1	7.85	.0185	.0092	7.70	⁻.1453
34.9	.7.88	.0176	.0160	7.68	⁻.1950
42.9	7.90	.0169	.0249	7.66	⁻.2409
50.8	7.90	.0169	.0357	7.63	⁻.2721
58.7	7.88	.0176	.0484	7.59	⁻.2888
66.6	7.85	.0185	.0630	7.55	⁻.3012
74.5	7.79	.0203	.0795	7.50	⁻.2891
82.2	7.73	.0222	.0974	7.45	⁻.2812
89.9	7.67	.0241	.1172	7.39	⁻.2785
97.6	7.60	.0263	.1389	7.33	⁻.2712
105.1	7.52	.0287	.1617	7.26	⁻.2573
112.6	7.44	.0312	.1862	7.19	⁻.2485
120.1	7.35	.0340	.2125	7.12	⁻.2347
127.4	7.26	.0368	.2398	7.04	⁻.2237
134.6	7.16	.0399	.2682	6.95	⁻.2063
141.7	7.06	.0430	.2979	6.87	⁻.1922
148.7	6.97	.0458	.3286	6.78	⁻.1914
155.6	6.89	.0483	.3604	6.69	⁻.2036
162.4	6.81	.0509	.3932	6.59	⁻.2186
169.2	6.74	.0530	.4274	6.49	⁻.2477
175.9	6.65	.0558	.4625	6.39	⁻.2594
182.6	6.56	.0586	.4990	6.28	⁻.2752
189.1	6.47	.0614	.5357	6.18	⁻.2916
195.5	6.38	.0642	.5731	6.07	⁻.3100
201.8	6.29	.0670	.6112	5.96	⁻.3304
208.1	6.19	.0701	.6505	5.85	⁻.3443
214.3	6.07	.0738	.6903	5.73	⁻.3398
220.4	5.84	.0810	.7307	5.61	⁻.2269
223.2	5.68	.0859	.7496	5.56	⁻.1217
226.1	5.54	.0903	.7695	5.50	⁻.0393
231.6	5.17	.1018	.8078	5.39	.2196

*DRAG COEFFICIENT .09010, ROLLING FRICTION COEFFICIENT .02217

38

WIND TUNNEL TESTING OF SCALED HANG GLIDERS
Eric J. Jumper,[*] Mark C. Kargul,[**]
and Glen R. Schlotterbeck[***]

Abstract

This report examines the feasibility of aquiring accurate aerodynamic characteristics for hang gliders using scaled models in a wind tunnel. First, the paper discusses the results of a literature search, next the parameters and equations applicable to collection and interpretation of data collected in the wind tunnel, and finally the results of wind tunnel tests conducted in the USAFA 2' x 3' subsonic wind tunnel.

I. Introduction

A. Background

There is no longer a question about the important role the wind tunnel plays in

aeronautic design; ever since the Wright brothers' first powered flight, aerodynamicists

have appreciated the wind tunnel's contribution to understanding the aerodynamic and

control characteristics of an aircraft design prior to flight testing. It comes as no

surprise, then, that there are those who have wanted to apply wind tunnel techniques to

the design of hang gliders. What does come as a surprise, however, is the presence of

an immense inertia opposing the use of wind tunnels in hang glider design.

At least one manufacturer of hang gliders openly expressed a need for some sort

of unmanned testing of new designs, and the wind tunnel was one of the options explored.

The manufacturer was Sun Sail Corporation of Denver. In an interview with Glider Rider

the co-owners, Brian Jensen and Scott Rojohn, commented on the state of the testing art

and the need for unmanned testing (Ref. 1). Jensen and Rojohn typified commercial hang

glider manufacturers; they were not well versed in aerodynamics. Untypical was the

technical expertise of Rojohn, whose background was in electro-mechanics, structures and

materials. As is true for most manufacturers, both men had years of hang gliding exper-

ience and were well versed in traditional hang glider testing - build them and fly them.

[*]Captain, USAF, Assistant Professor of Aeronautics, DFAN
[**]Cadet, USAFA
[***]Cadet, USAFA

To present, handling characteristics came from so called "public testing" - if the accident record was low that meant the handling characteristics were good. In the words of Jensen this meant the "burden of testing ended up on the unsuspecting public." Jensen went on to say that "old designs are becoming obsolete before they are really understood. And, because of that, the potential problems of the old ones are being transfered to the new ones and added to all the new things that are coming out in the new ones.... We are going to have a lot of bad things happen if we don't start trying to understand what's really happening in the design of these things."

Because of the nonavailability of a wind tunnel for testing their designs, Jensen and Rojohn designed a mount for their pick-up truck. Using a fish scale they obtained information about the forces required to change angle of attack and were able to modify the hang gliders by trial and error to eliminate "bad handling characteristics". This rather crude approach to design was an important first step and Jensen's interest did not stop there.

We first contacted Jensen in January of 1977 while trying to locate a so called "high performance" hang glider design to use as a model for wind tunnel testing. Jensen was extremely cooperative and loaned us one of his designs called the Swift. Jensen has followed our work to see if our results warranted enough confidence to overcome the un-favorable inertia concerning tunnel testing.

B. Scope

The purpose of this project was to demonstrate the feasibility of using the wind tunnel as a tool for designing hang gliders. The approach was to 1) locate full scale hang glider data from any available source, 2) construct and wind tunnel test scale models of full scale hang gliders for which data was available, and 3) draw conclusions based on comparisons between the full scale and model data.

II. Available Data

We found only one good set of data on a full scale hang glider-type wing configura-tion, NASA Technical Note D-1946 (Ref. 2). The wing type was a standard conical Rogallo wing shape. The work reported an entire range of aerodynamic data taken in full scale

wind tunnel tests. The data had been validated through actual flight tests in an associate program, thus could be considered actual full scale flight test data.

Flight test data for the swift was not nearly as complete as for the standard Rogallo wing. We were forced to reduce pertinent data points from rather unsophisticated and uncontrolled observations reported on in advertisements and popularized hang glider articles.

Also refered to in this paper is work reported on by Robert Lee Bass (Ref. 3) who ran wind tunnel tests on small scaled models at the University of Texas at Austin.

III. Theory

The theory used in this project was rather simple basic aerodynamics. In the following we will simply give references to the equations used for reducing the swift flight test data. Additionally reference will be made to part of the data reduction technique for reducing our wind tunnel data simply because it is not readily available elsewhere.

A. Reduction of Swift Flight Test Observations

Reference 4 reported the maximum glide ratio and stall speed of a slightly more advanced swift than we tested. In order to get a ball park estimate of the actual flight characteristics, we backed out the approximate maximum lift to drag ratio, $L_{/D_{max}}$, and the maximum coefficient of lift, $C_{L_{max}}$ using the following equations (Ref. 5),

$$L_{/D_{max}} = \frac{C_L}{C_D}\bigg|_{max} = \text{max glide ratio} \tag{1}$$

and

$$C_{L_{max}} \simeq \frac{W}{\frac{1}{2}\rho V^2_{stall} S} \tag{2}$$

where C_D is the coefficient of drag, W is the weight of the man/hang glider combination, ρ is the air density, V_{stall} the stall speed and S is the planform area of the actual swift.

41

B. Wind Tunnel Test Reduction Parameters

Of concern to the correct reduction of the wind tunnel data and the interpretation of that data, which will follow in another section, are the calculation of the mean aerodynamic chord, the calculation of the correct pitching moment, and the concept of the Oswald Efficiency.

1. Mean Aerodynamic Chord

By definition, the mean aerodynamic chord (MAC) is the length of a line drawn through the centroid of one side of a wing parallel to the airplane longitudinal axis. In the case of a triangular wing (the classic Rogallo shape for example) the centroid of each side of the wing is simply located 1/3 the distance from the root to the wing tip. Irregular shapes, however, must use the following equation for determining MAC

$$MAC = \frac{c^2 \, dy}{c \, dy} \tag{3}$$

where c is the chord at location y and y is the distance from the wing root. For determining the MAC on the swift the wing was divided into difference sections and the integral was approximated by a summation.

$$MAC = \frac{\sum\limits_{i} \bar{c}_i^2 \, \Delta y_i}{\sum\limits_{i} \bar{c}_i \, \Delta y_i} \tag{4}$$

where $\bar{c}_i$ is the average cord for section of width Δy_i .

C. Pitching Moment

Pitching moment information from the wind tunnel tests is given referenced to the electrical center of the force balance in the tunnel. In order to get meaningful information the pitching moment curve must be mathematically shifted to the location on the model corresponding to the center of gravity of the prototype.

Of interest to this project was the slope of the pitching moment coefficient curve when pitching moment coefficient was plotted against the coefficient of lift. The coefficient of moment, C_M , is defined as

42

$$C_M = \frac{M}{\frac{1}{2}\rho V^2 S \bar{c}} \tag{5}$$

where the M was the moment at a given angle of attack. C_M was then plotted against C_L at the same angle of attack. Having C_M vs C_L the slope in the liniear portion of the curve, $C_{M_{C_L}}$ could be found. The negative of $C_{M_{C_L}}$ is known as the static margin, SM, or

$$SM = -C_{M_{C_L}} \tag{6}$$

Generally $C_{M_{C_L}}$ is plotted in relation to the center of gravity of the prototype in these cases stability judgements can be made, and the SM has a physical significance (it is the distance from the center of gravity to the neutral point, the point where the moment is zero, divided by $\bar{c}$). In the case of the wind tunnel data, however, the SM obtained purely from the data is in relation to the electrical center of the force balance, and is, therefore, the distance of the neutral point from the electrical center of the balance divided by $\bar{c}$. In order to find the SM about the CG location for the prototype, the neutral point must be found by

$$X_{NP} = SM_{EC} \, \bar{c} + X_{EC} \tag{7}$$

Then the new SM for the CG is found by

$$SM_{CG} = \frac{X_{NP} - X_{CG}}{\bar{c}} \tag{8}$$

or substituting Eqn (7) into Eqn (8)

$$SM_{CG} = \frac{SM_{EC} \, \bar{c} + X_{EC} - X_{CG}}{\bar{c}} \tag{9}$$

We were then able to use the SM_{CG} found from Eqn (9) to make stability judgements about the model/prototype.

43

D. Oswald Efficiency

If the coefficient of drag for a given wing is plotted against the coefficient of lift squared the linear portion of the curve for an ideally load distributed wing is given by

$$C_D = C_{D_O} + \frac{1}{\pi A\!\!R} \, C_L^2 \tag{10}$$

where $A\!\!R$ is the aspect ratio of the wing. For a non-ideally loaded wing Eqn (10) is modified by the inclusion of the Oswald efficiency factor, e, which is a measure of the efficiency of the wing (i.e., how close it comes to an ideal wing) where e = 1 would correspond to an ideally loaded wing. Thus Eqn (10) is modified as shown in Eqn (11)

$$C_D = C_{D_O} + \frac{1}{e \, \pi A\!\!R} \, C_L^2 \tag{11}$$

For conventional lowspeed aircraft the efficiency factor has a value of about 0.91 to 0.77 (Ref 3).

IV. Experiment

A. Data and Observations

Data was taken on four different flexible wing models in the USAFA 2' x 3' subsonic wind tunnel. The models were sting mounted and strain gauge sensors sensed sting oriented axial, normal and torsional forces. The signals from these sensors together with angle of attack with respect to the tunnel axis and air flow information were reduced to yield C_L, C_D and C_M (about the electrical center) vs angle of attack. The experiments were repeated at various airspeeds ranging from 35 ft/sec to 62 ft/sec. In addition to the force coefficent data, observations were made about the condition of the wing at various airspeeds and angles of attack.

B. Models

Four wind tunnel models were tested. The models were made from two planform areas: Swift (or high performance planform), and Flexi-Flier (standard Rogallo planform). Each of these two planforms were tested in two geometric configurations. In the case of both the Swift and the Flexi-Flier the configuration change was a change in the

44
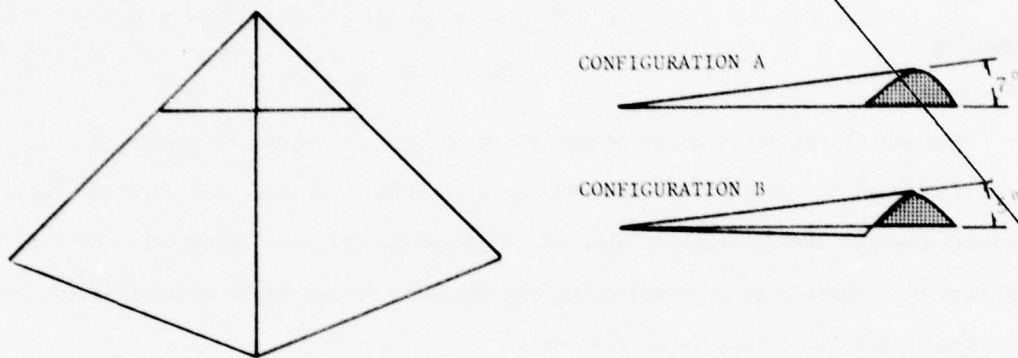
Figure 1. Flexi-Flier Configurations--Standard Rogallo Planform
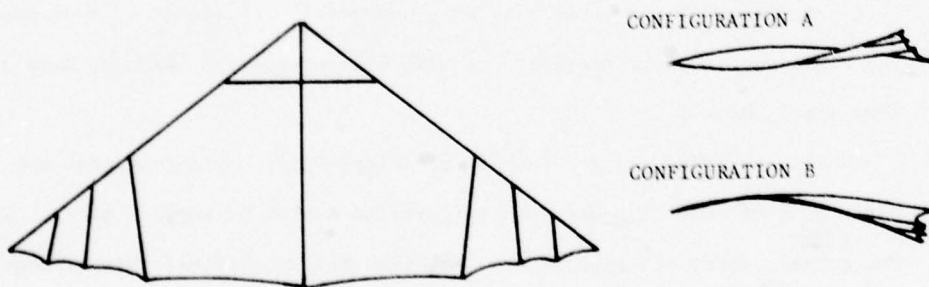

Figure 2. Swift Configurations--High Performance Planform

45

leading edge shapes (see Figures 1 and 2). Acrylic spray was also used to modify the porosity of the wing material (in the figures unsprayed is referred to as "porosity" and sprayed as "no porosity").

V. Results

A. Data

The results of testing are presented in various conventional formats in Figures 3 through 7. In all of these the angle of attack was measured from the keel. The titles explain the contents of each of the figures. Figure 9 presents the Flexi-Flier data in a modified manner adjusting the angle of attack to be measured from the top of the billow, α_B, instead of the keel.

B. Observations

1. Flexi-Flier

a. Flutter

In all configurations the Flexi-Flier fluttered excessively at angles, α_K, from $-10°$ to $+15°$. Flutter was present to a small degree at all angles of attack. Starting from $+15°$ and reducing the angle of attack, the flutter started at the trailing edge of the wing; as the angle of attack was decreased the flutter grew in amplitude and frequency as well as enveloping more of the wing. The wing was totally enveloped by $+4°$ and as the angle continued to decrease the wing billow reversed becoming more or less stable at $-10°$.

While the trend was the same in all Flexi-Flier configurations, the worst flutter condition was in configuration A with no acrylic spray. When the acrylic spray was applied, the material became stiffer; this reduced the severity of the flutter. In configuration B nylon threaded cellophane packing tape was added to the trailing edge, further reducing the severity of the flutter.

b. Airspeed Variations

Airspeed variations did not seem to affect the data. All data taken at different airspeeds on the same configuration overlayed each other exactly. Visual observation of the billow shape and later comparison of photographs
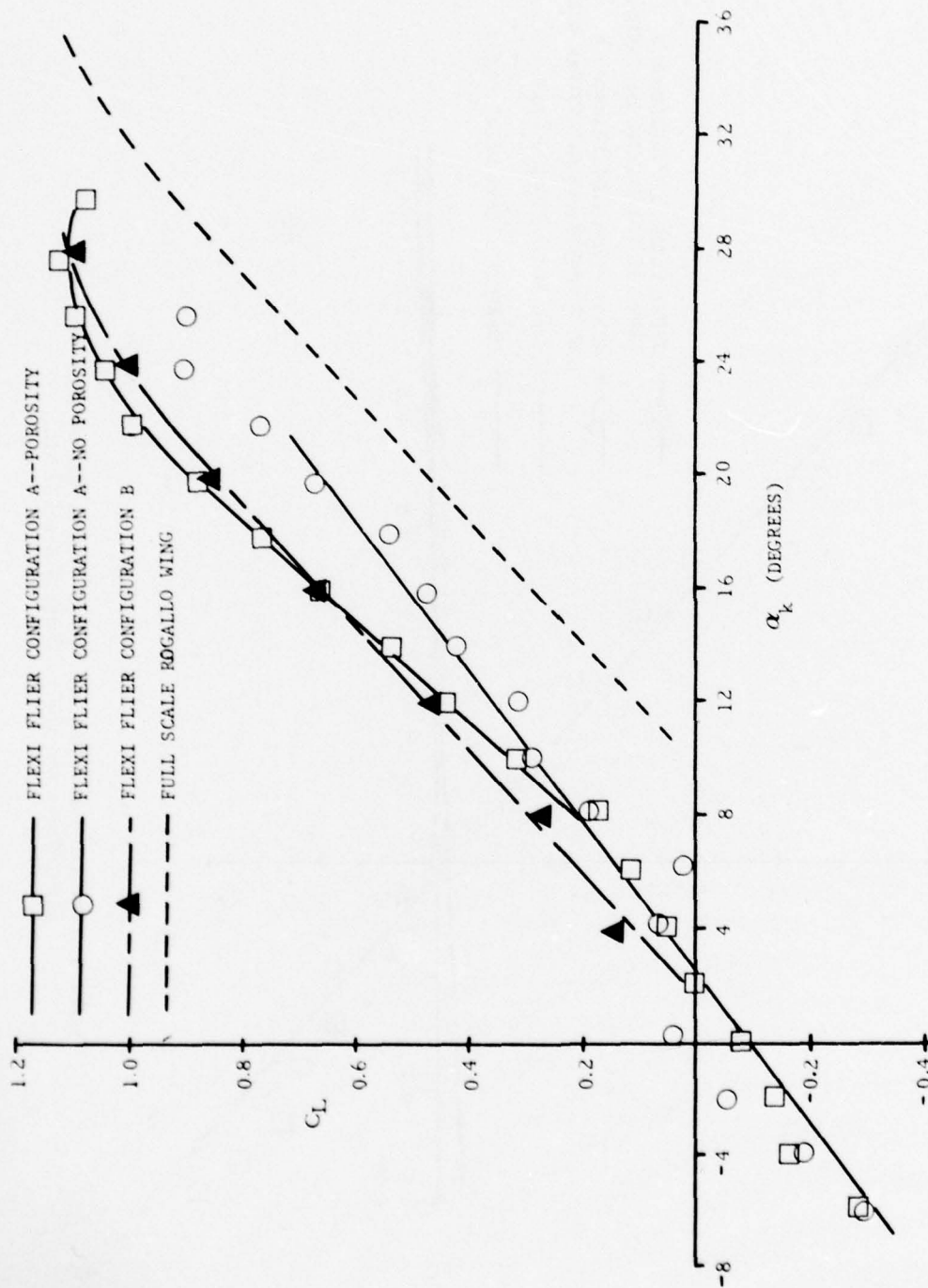
46

Figure 3. Coefficient of Lift versus Angle of Attack Measured from the Keel Line for the Flexi-Flier Configurations and the Full Scale Rogallo Wing
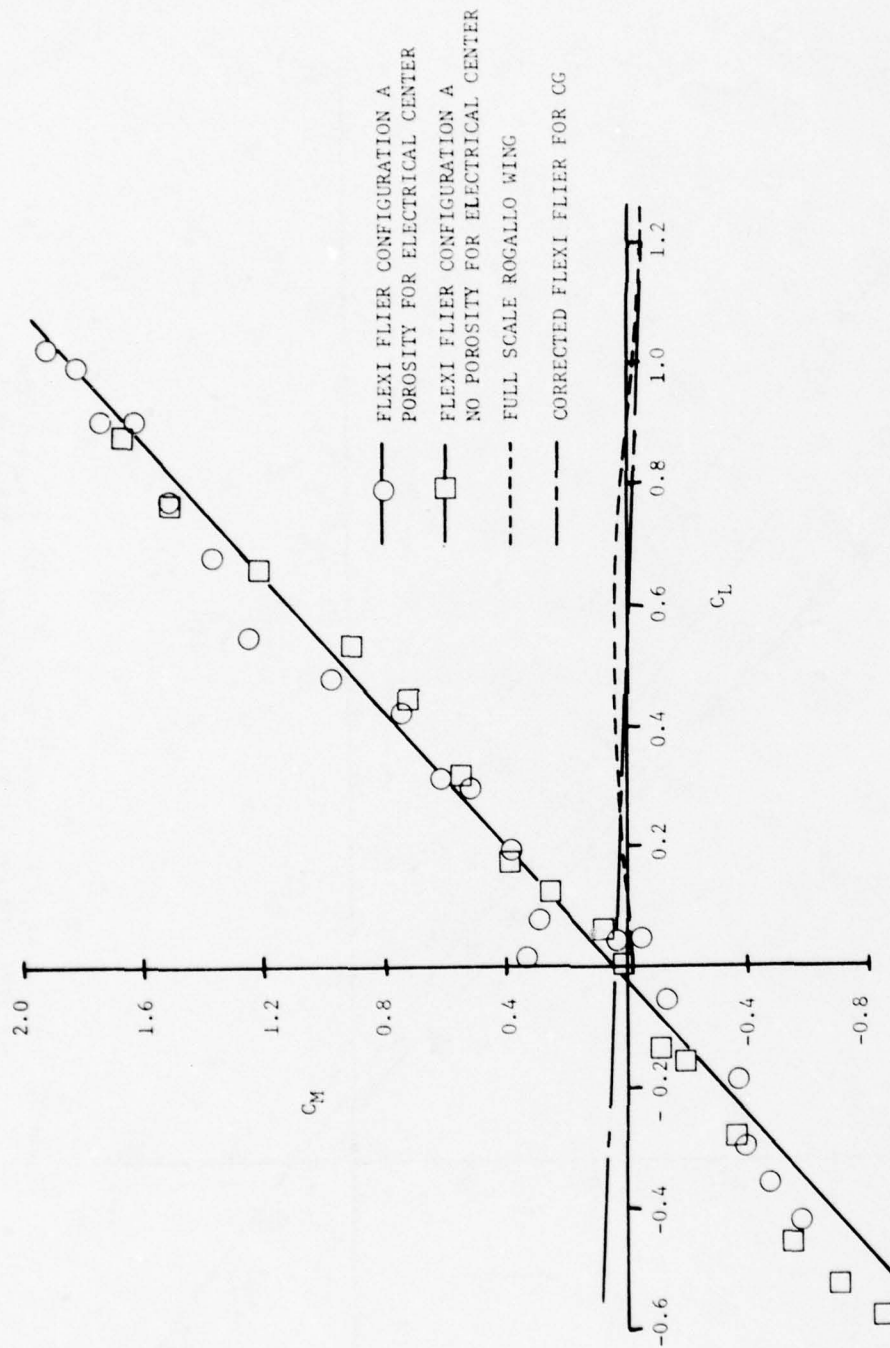
Figure 4. Coefficient of Moment versus Coefficient of Lift for the Flexi-Flier and the Full Scale Rogallo Wing
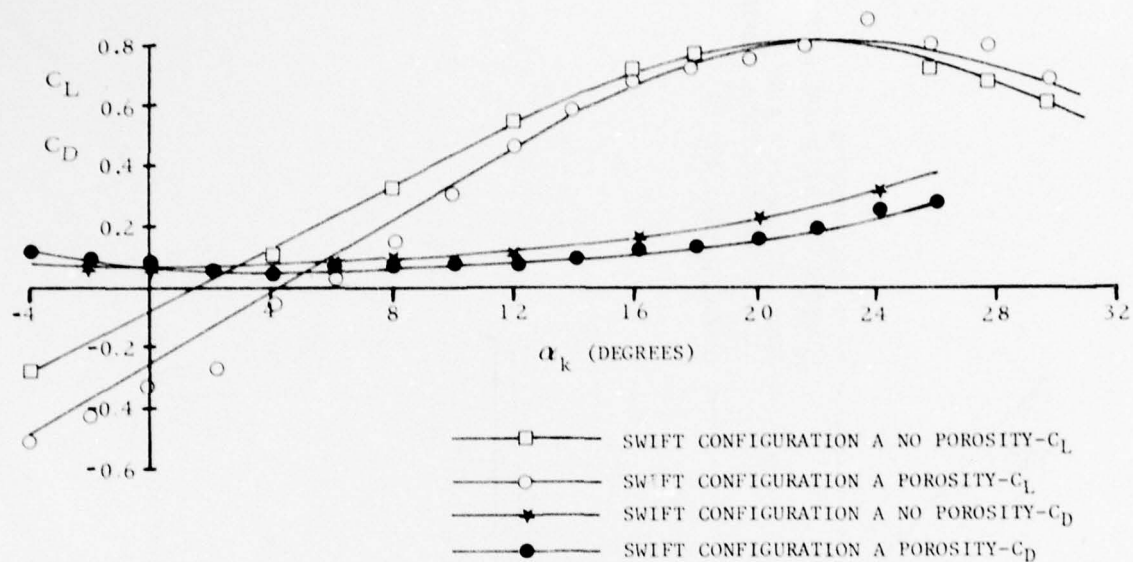
48

Figure 5. Coefficient of Lift and Coefficient of Drag versus Angle of Attack Measured from the Keel for the Swift
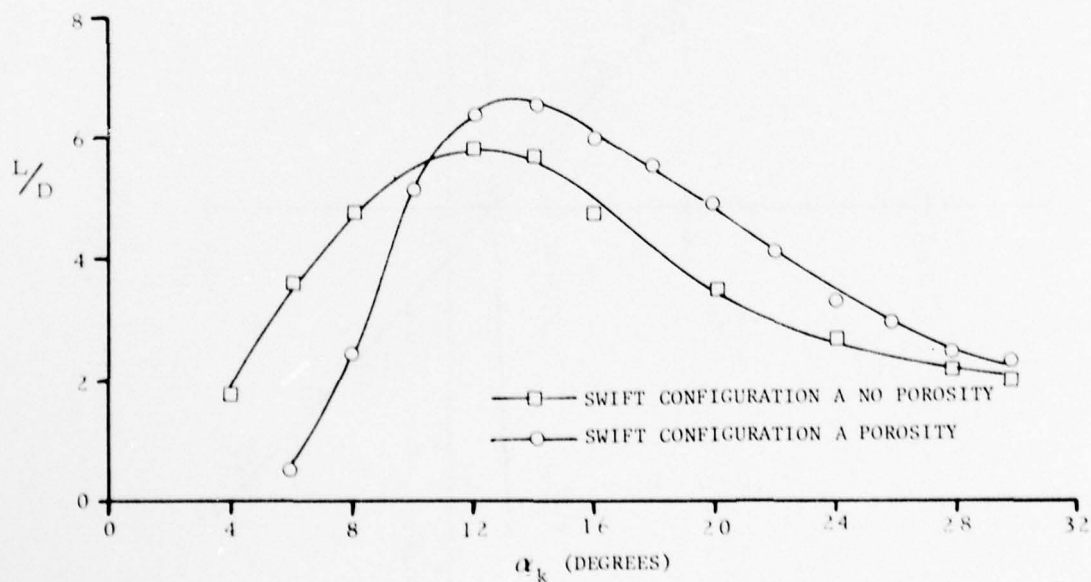

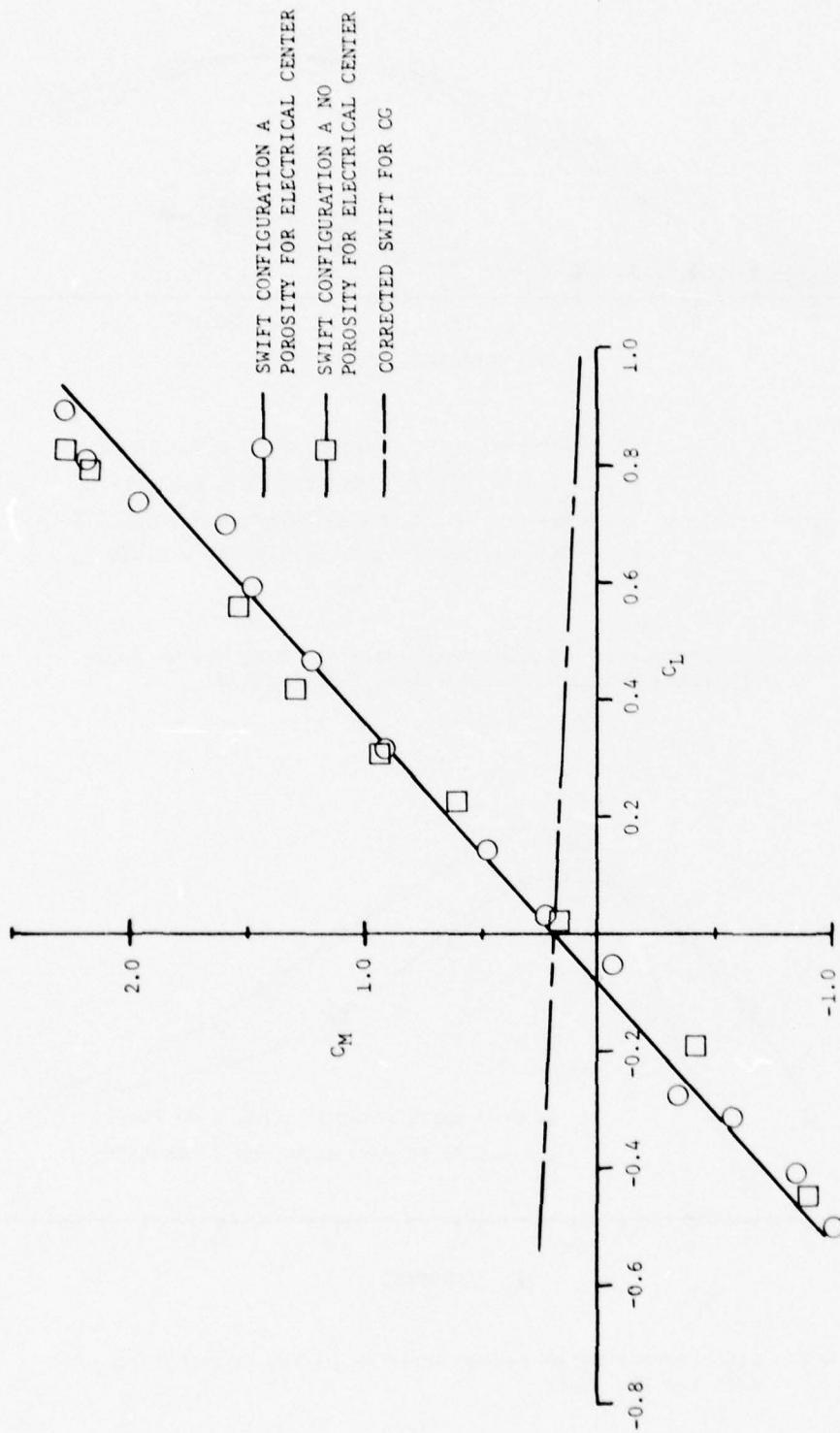Figure 6. Lift-to-Drag Ratio versus Angle of Attack Measured from the Keel for the Swift

Figure 7. Coefficient of Moment versus Coefficient of Lift for the Swift

50

taken during each run showed identical wing shapes at all airspeeds. The flutter had a lower frequency at the slower airspeeds than at the higher airspeeds; the amplitude and severity of the flutter, however, were unchanged.

2. Swift

The Swift configurations included wing battens. These battens held a cambered shape in the wing at all angles of attack including the negative angles. No flutter occurred with the Swift. Data and wing shape remained unchanged with changing airspeed.

VI. Discussion

A. Flexi-Flier

1. Coefficient of Lift

As mentioned in Section II the only available full scale data for comparision was found in Reference 2. Because of the added structure in the NASA test (manned control carriage, etc.) a comparison of the drag data would not be meaningful. Lift data, however, was compared. Figure 3 shows an overlay of the Flexi-Flier configuration data and the NASA data. Some simularities are obvious. The slopes, for example, are nearly identical. There is also an obvious difference; the C_L equals zero intersects differ by up to 8 degrees.

If we examine the configuration differences we notice something quite interesting; the main difference between the configurations is their billow heights. If we further examine the profiles of configuration A, B and the full scale wing we see that the billow angles are 7 degrees, 5 degrees and 13 degrees respectively (See figure 1). As mentioned by Bass (ref. 3) the C_L zero intersect shifts to the right as the sail billow is increased. Because of this statement, we decided to try replotting the data based on the angle between the top of the sail billow and the relative wind, α_B, rather than angle based on the keel line, α_k. The result of this data manipulation is shown on figure 8. Amazingly all sets of data collapse onto the same line.

This result suggests two things. First, it would appear that for the Rogallo type wing the angle-of-attack used for plotting C_L vs α should be measured from the billow line and not the keel line (as has been traditionally
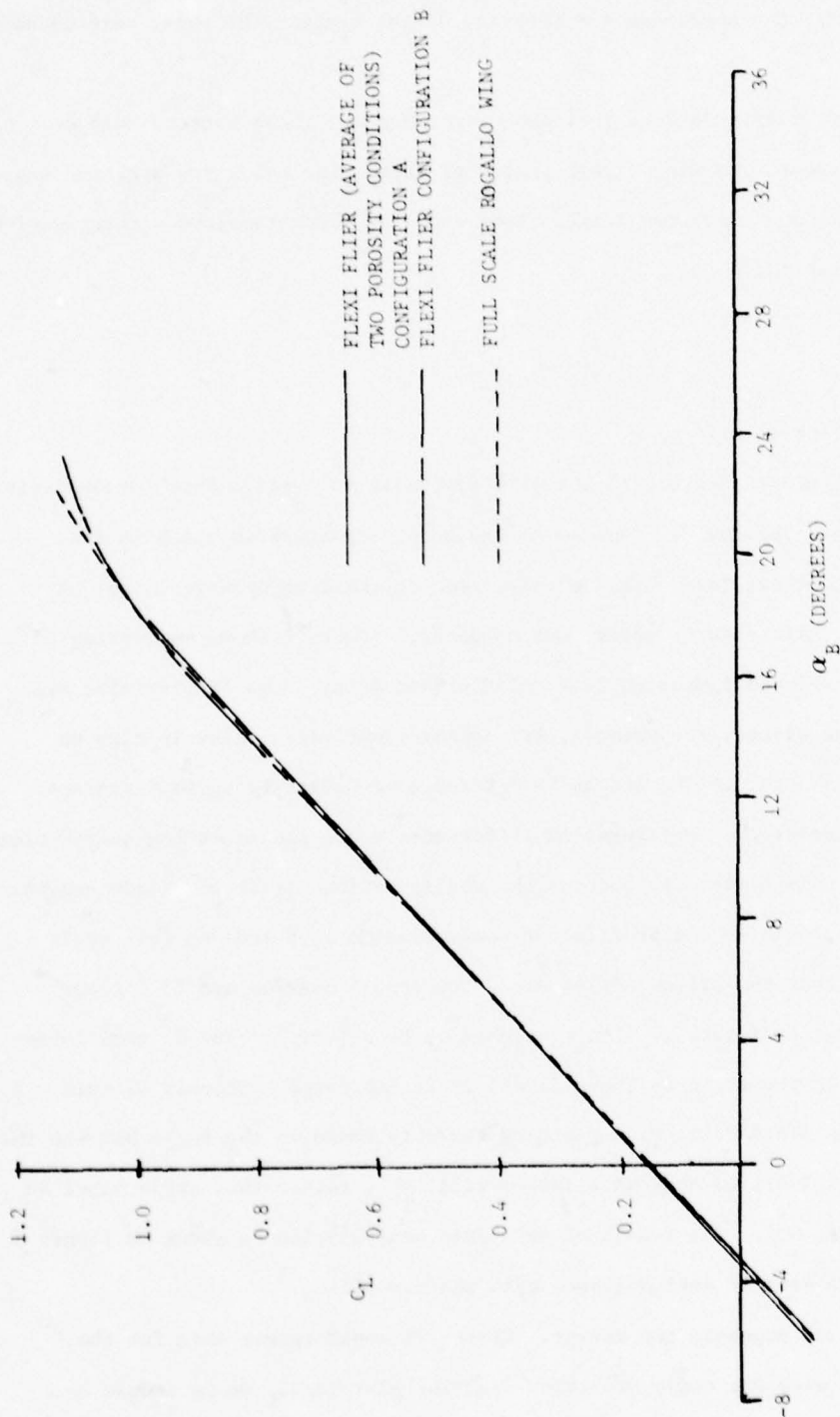
Figure 8. Coefficient of Lift versus Angle of Attack Measured from the Billow Line for Flexi-Flier Configurations and Full Scale Rogallo Wing

the case). Second, when the data is plotted in this manner, it seems apparent

that the scaled wind tunnel data compares very well with full scale data.

2. Coefficient of Moment

An observation can also be made about the scale model $C_{M_{C_L}}$ slope as

compared to the full scale model. Figure 4 shows the original data about the

electrical center and the adjusted slope to the assumed center of gravity

overlayed with the full scale wing. The adjusted curve was made based on

Equation 9 of section III. As shown in Figure 4, both the model and the full

scale wing exhibit near neutral stability and, based on this curve, exhibit

almost identical stability characteristics. It should be noted that the choice

of CG is somewhat arbitrary and was, in fact, chosen to make the curves in

Figure 8 coincide. The CG location needed, however, appeared to be very

reasonable.

B. Swift

1. Comparison with available data

As mentioned in section II very little data is available on the performance

of a full scale Swift. From advertisements of stall speed and glide ratio

(i.e., best forward distance to decent distance) it was possible to back out

an approximate $(L/D)_{max}$ and $C_{L_{max}}$ (Ref. 4). The actual Swift we tested was an

earlier model than that advertised, the Swift A; however, since the newer Swift

advertisements were the only information available, the Swift A information was

used for comparison purposes. The main difference between the model we tested

and the Swift A was a longer wing span reflected in the Swift A aspect ratio of

5.28 compared to our model of aspect ratio 4.76. The performance of the Swift A

was thus expected to be somewhat better than that predicted by our wind tunnel

tests. Also from Reference 4, the stall velocity for the Swift A was stated to be

13 MPH. Assuming a 150 pound man plus the 40 pound weight of the wing, an

area of 170 square ft and sea level conditions Eqn (2) yielded a $C_{L_{max}}$ of 1.28.

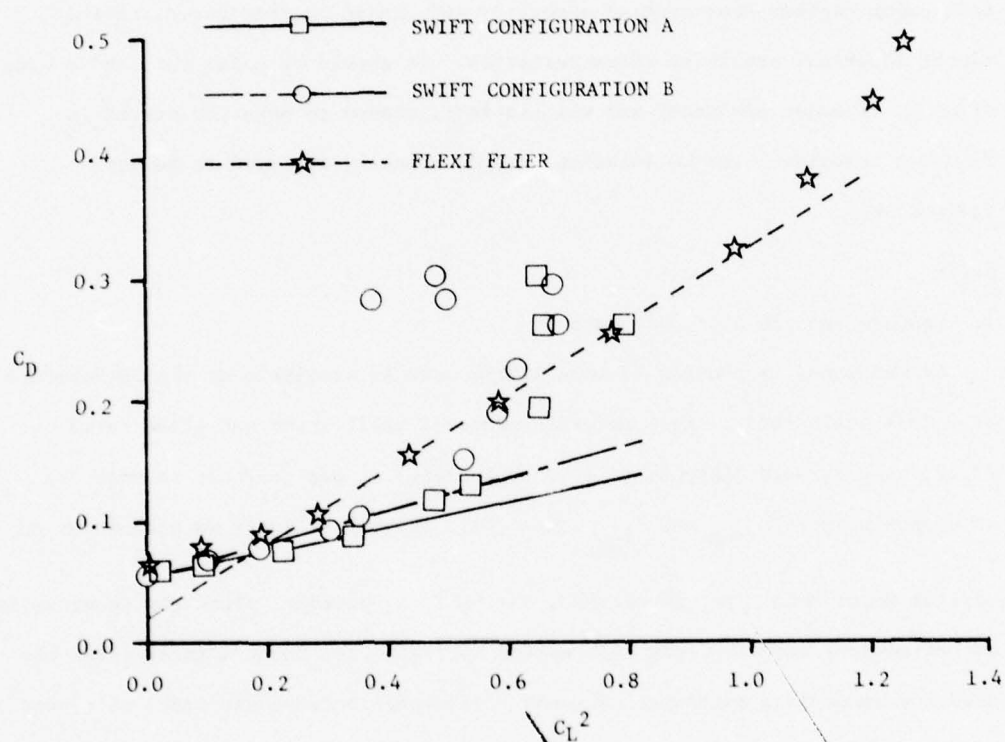According to Reference 4, the max glide ratio was 7 to 1. Using Eqn (1), $(L/D)_{max}$

53

Figure 9. Coefficient of Drag versus Coefficient of Lift Squared for the Swift Configurations and for a Flexi-Flier Configuration

54

is equal to 7. The wind tunnel valves obtained were a $C_{L_{max}}$ of 0.85 and an $(L/D)_{max}$ of 6.8 as shown in figures 5 and 6.

Because of the many approximations required to obtain these numbers the comparison is of little value except to say that they compare reasonably well.

2. Oswald efficiency

One interesting observation, from a design stand point, can be made from Figure 9. Figure 9 shows the result of plotting C_D vs C_L^2 for the configurations A and B of the Swift. According to the theory in section III, Eqn (11) provides a method of calculating the Oswald efficiency. Assuming our interpretation of the data is correct, using the slope of the linear portion of the curves in Figure 9 and an aspect ratio of 4.76 yields efficiency factors of 0.67 and 0.51, for the configurations A and B Swifts respectively. It is interesting that this rather large change in efficiency resulted from only slight changes in geometry (i.e., a slight change in wing tip shape). This emphasizes, we think, the usefulness of using the wind tunnel as a tool for optimizing hang glider designs.

VII. Conclusions and Recommendations

The purpose of this project was to show the feasibility of using the wind tunnel as a design tool. While the results of the project seem to indicate that the wind tunnel data presented here is compatable with the full scale data collected by NASA, it can not, unfortunately, be taken as conclusive. The reason is that the exact configuration of the full scale NASA wind tunnel model was not exactly duplicated. When collapsed onto the billow angle, however, the data certainly suggest that wind tunnel testing is as valid for hang glider analysis as for conventional aircraft designs. Further, from the results of the small shape modification of the leading edge, we think the usefulness of the wind tunnel in hang glider design has been clearly demonstrated.

References

1. Knauss, T., "Jensen & Rojohn Talk about the Swift", Glider Rider, Vol 2, 1, p. 24, Feb 1977.

2. Johnson, J. L., Jr., Full-Scale Wind Tunnel Investigation of a Flexible Wing Manned Test Vehicle, NASA-TN-D-1946, 1963.

3. Bass, R. B., III, An Experimental and Theoretical Investigation of the Lift and Drag Characteristics of Flexible Parawings at Low Subsonic Speeds, University of Texas at Austin Aerospace Engineering Research Report, July 1968.

4. Sun Swift Advertisement, Sun Sail Corporation, 6753 E. 47th Ave Drive, Denver, CO 80216.

5. Clancy, L. J., Aerodynamics, Halsted Press, New York, 1975.

SECTION II

FLUID MECHANICS

A SIMPLE MODEL OF TEMPERATURE GRADIENT METAMORPHISM

James R. Williams[*]

Abstract

Increasing winter mountain travel by skiers, snow mobilers, and climbers means an increasing exposure to avalanches. Slab avalanches, the most important source of winter hazard in the mountains, occur when the stresses in the snowpack exceed the strengths of the anchors holding it in place. The major anchor is the shear strength between the snowpack and the surface beneath it. Any layer with a weak shear strength is a potential sliding surface for a slab avalanche. Temperature gradient metamorphism is one of the primary mechanisms by which weak layers are produced in the snowpack. A simple model is proposed which explains the mechanism of temperature gradient metamorphism and gives qualitative results which agree with observations.

I. Introduction

Avalanches seldom touch man or his works, but when they do, the results can be disastrous. From data reported to the U.S. Forest Service's Rocky Mountain Forest and Range Experiment Station it has been estimated that there are about 10,000 avalanches in the United States each year. Typically, 1 percent of these harm man or his property, accounting for an average of seven lives and $300,000 in property damage each year (Ref. 1). This paper will discuss the two major types of avalanches and present a simple analysis of snow structure metamorphisms, the principle factor in determining the probability of slab avalanches.

II. Types of Avalanches

Two principle types of avalanches are recognized: loose snow avalanches and slab avalanches. The classification is always based on the snow at the point of origin with the distinction being the mechanical character of the snow.

A. Loose Snow Avalanches

Loose snow avalanches start at a point or over a small area. Since they have little internal cohesion, loose snow slides tend to move as a formless mass, growing in size as they descend. A clearly distinguishable sliding layer is not always present and

---

[*]Captain, USAF, Instructor of Aeronautics, DFAN
Asst OIC of Cross Country Skiing,
Cadet Mountaineering Club

the line separating the sliding snow and that which has remained in place is often in-
definite.

Loose snow avalanches occur when snow accumulates on slopes of steeper angle than
its natural angle of repose. This can occur by: (1) deposition of light fluffy snow
under conditions of little wind; (2) reduction of internal cohesion among the snow
crystals by metamorphic changes; or (3) lubrication from percolating melt water. Any
small disturbance is propagated downward from crystal to crystal, causing the snow to
slump downhill towards its natural angle of repose. If sufficient momentum is attained,
the snow may slide onto slopes of lesser angle.

B. Slab Avalanches

The slab avalanche is the major concern because it forms the most important source
of winter hazard in the mountains. Slab avalanches are characterized by the internal co-
hesion of the snow involved. The common characteristic is a large area of snow begins to
slide at once. A well-defined fracture line where the moving snow blanket breaks away
from the stable snow is the positive identifying characteristic. A definite sliding
layer is usually distinguishable.
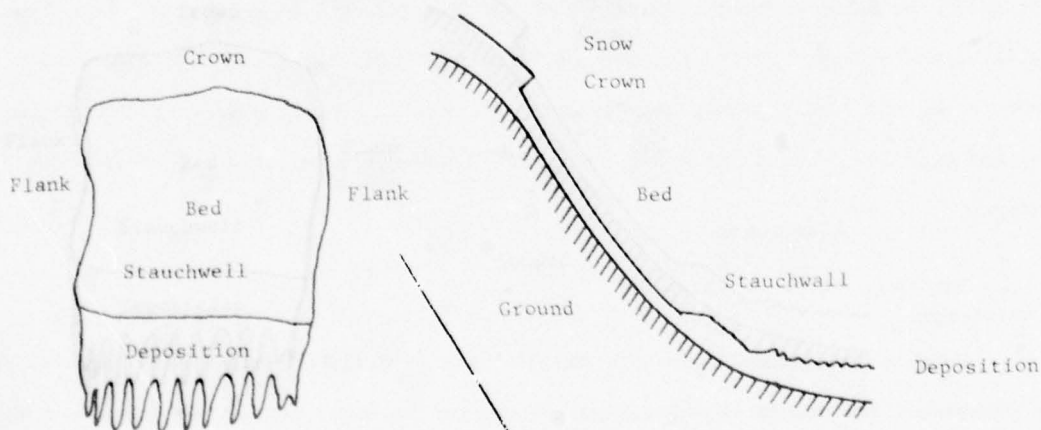
Figure 1 Nomenclature for a Slab Avalanche

The snowpack is held on the mountain by a simple balance of mechanical forces.
Gravity tries to pull the snow down the hill while the internal forces try to resist.
Simply stated, the snowpack will slide when the stresses exceed the strengths of the

59

anchors. At the beginning of a slide, the following failures typically occur (Fig. 1). The crown line fails in tension as the snow is literally pulled apart. The flanks, bed and stauchwall fail in shear. Since the bed is by far the largest area involved, it plays the major role in holding the snowpack on the mountain. Any layer in the snow which has low shear strength must be viewed as a possible bed for a slab avalanche. In some cases, the entire snowpack will slide, using the ground as the bed surface.

Since mechanical forces are involved the structure of the snow is important. The snow structure, however, does not remain constant; but rather, undergoes metamorphisis which greatly effects the probabilities of slab avalanches.

III. Types of Metamorphisis

There are three types of metamorphic changes which alter the structure of the snow crystals after they are in the snow pack: melt-freeze metamorphism, equitemperature metamorphism and temperature gradient metamorphism.

A. Melt-Freeze Metamorphism

Melt-freeze metamorphism occurs where temperature fluctuations cause melting and refreezing, building clusters of large grains. The strength of a layer of melt-freeze grains varies widely. During the melt part of the cycle, the grains are essentially separate and are held together only by surface tension. The structure is then extremely weak and ductile. On the other hand, when the layer refreezes it can have enormous strength.

B. Equitemperature Metamorphism

Between temperatures of -40°C and 0°C, ice crystals and water vapor coexist in the snowpack. The amount of water vapor is called the vapor density and depends not only on the temperature but on the geometry of the snow crystal. Convex regions have a higher vapor density than concave regions (Fig. 2). This results in the water vapor diffusing from the convex areas of the crystal to the concave areas. Additionally, the water vapor is transported to the concave region between crystals which are in contact. Equitemperature metamorphism thus tends to produce rounded grains which are connected to each other.
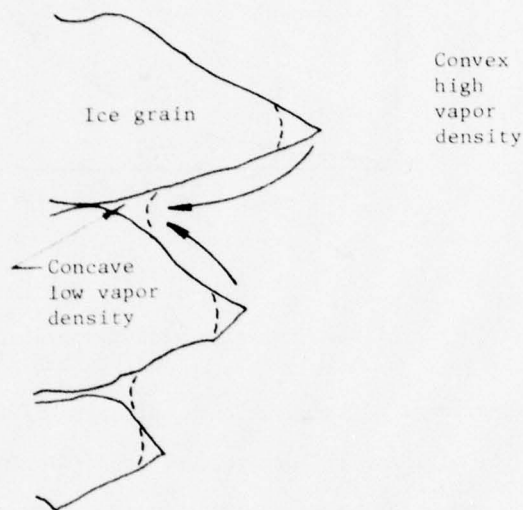
60

This results in a very strong snowpack.

Figure 2. Equitemperature Metamorphism (Ref. 1)

C. Temperature Gradient Matamorphism

The temperature dependence of the vapor density (Fig. 3) implies more vapor is present in a warm snowpack than a cold snowpack. Since vapor tends to diffuse from areas of high concentration to those of low concentration, a net mass transport occurs in the snow pack. This typically results in mass being deposited in the colder layers at the expense of the warm layers. The enlarged grains that result are characterized by flat, sometimes steplike or straited faces which intersect at sharp, angular corners. Since there is little cohesion between the grains the layer is very weak.

IV. Analysis of Temperature Gradient Metamorphism

For simplicity in modeling the temperature gradient metamorphism process we will assume a linear temperature profile with 0°C at the ground and -40°C at the surface. The extension to arbitrary temperature profiles is straight forward and will be explained later.
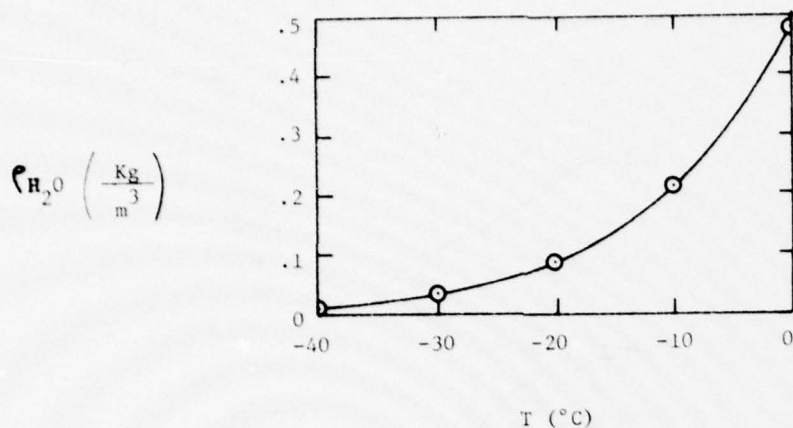
Figure 3. Variation of Vapor Density with Temperature (Ref. 2)

Consider in detail an increment of snowpack with thickness dx (Fig. 4). The element has vapor flowing in from the high temperature region, vapor flowing out into the low temperature region, vapor being produced from the snow crystals and vapor being condensed onto the snow crystals. A mass balance on the vapor gives:

$$\dot{M}(x) + \dot{M}_p = \dot{M}(x+dx) + \dot{M}_c \tag{1}$$

The net rate of crystal growth in the region is:

$$\dot{M}_c - \dot{M}_p = \dot{M}(x) - \dot{M}(x+dx) \tag{2}$$
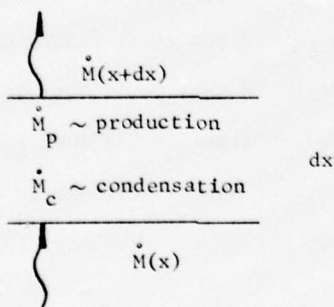
Figure 4. Detail of Snowpack Layer

Since diffusion is the mechanism causing the mass transport, we may write (Ref. 3):

$$\dot{M}(x) = -\rho D \frac{dm}{dx} \tag{3}$$

where:

$$\rho = \text{density of the mixture}$$

$$= \rho_{H_2O} + \rho_{AIR}$$

$$D = \text{diffusion coefficient}$$

$$m = \text{mass of water vapor per mass of mixture}$$

$$= \frac{\rho_{H_2O}}{\rho_{H_2O} + \rho_{AIR}}$$

Thus it follows if $T(x) > T(x+dx)$, then $\dot{M}(x) > \dot{M}(x+dx)$. From eqn (2) we see this implies a net crystal growth in the area. Since crystal growth depends on $\dot{M}(x) - \dot{M}(x+dx)$, the greatest crystal growth will occur in the regions where the vapor density gradient changes most rapidly. For our linear temperature gradient, this will be the region closest to the ground (Fig 5). In the very cold regions of the snowpack, the vapor density gradient approaches zero, so little temperature gradient metamorphism will occur.
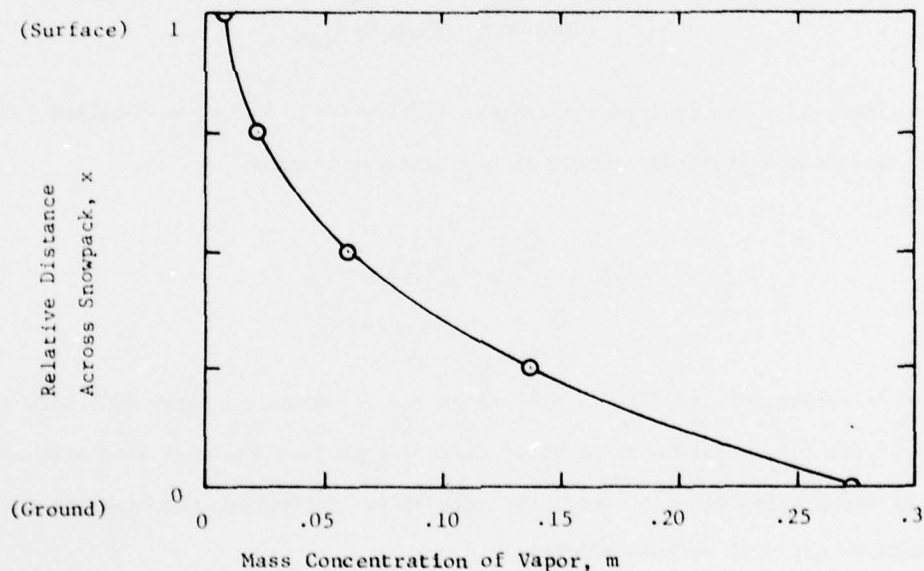
Figure 5. Mass Concentration of Vapor in the Snowpack, Linear Temperature Profile

At the lower boundary of the snowpack (i.e., the ground),

$$\dot{M}(0) = 0 \qquad (4)$$

Thus, the snowpack consumes itself from the ground up, either settling or creating a hollow space. The temperature gradient grain growth is greatest in the region immediately

63

adjacent to the ground and decreases with increasing distance from the ground. In the very cold regions of the snowpack, there is essentially no temperature gradient grain growth at all. This corresponds exactly to observation.

A particularly interesting case arises when

$$\dot{M}(x) = \dot{M}(x+dx) \tag{5}$$

implying no net crystal growth in the region. This is very similar to the case of equi-temperature metamorphism, which has vapor being produced and consumed, but with no net vapor flow. Is it possible then to have a non-uniform temperature distribution and equi-temperature metamorphism?

For no net crystal growth, Eqn (5) requires:

$$\left(\rho_{mix} \frac{dm}{dx}\right)_x = \left(\rho_{mix} \frac{dm}{dx}\right)_{x+dx}$$

An approximation of the desired temperature profile (Fig. 6) can be obtained by neglecting the small temperature dependence of ρ_{mix} and considering

$$\left.\frac{dm}{dx}\right)_x = \left.\frac{dm}{dx}\right)_{x+dx} \tag{6}$$

$$= constant$$

If this temperature profile is present in the snowpack, no layer will show a net crystal growth since the amount of vapor diffusing in from the warm side will match the amount of vapor diffusing out toward the cold side. Of course, the layer near the ground will still be consumed by this process.

It is interesting to speculate on the results of the metamorphic process occuring with this particular temperature profile. The physical situation can be imagined as something of an equitemperature process (since there is no net mass gain in any region) upon which is superimposed a net vapor flux.
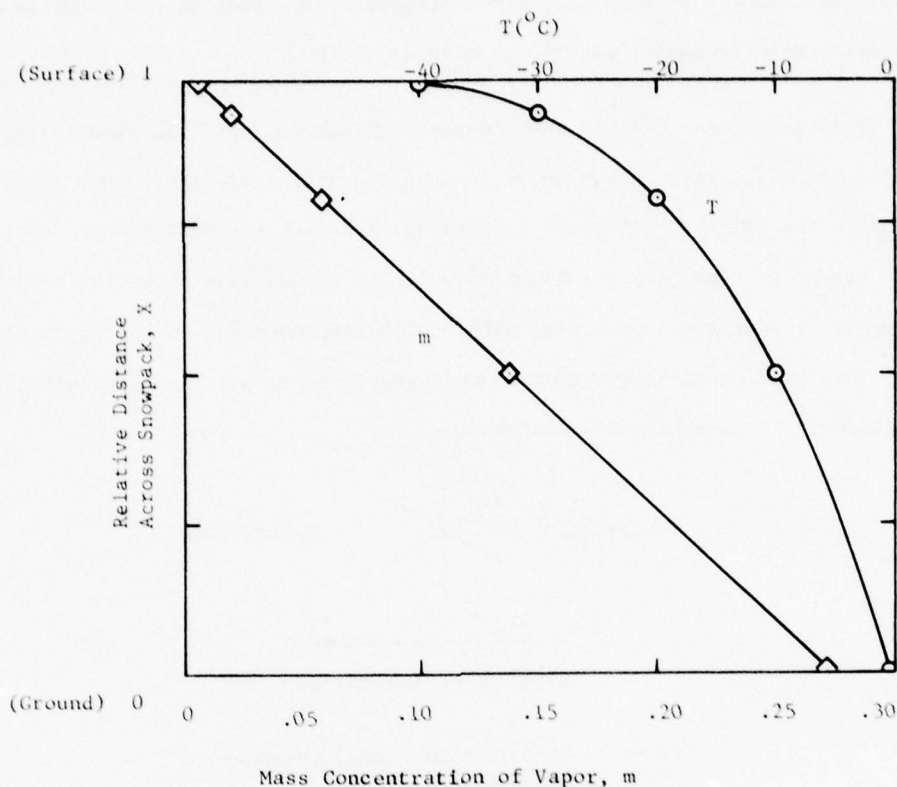
64

Figure 6   Temperature and Mass Concentration
Profiles for Zero Net Crystal Growth

Since there is no net gain of mass in any region, one possible result is equitemperature metamorphism with the vapor flux having little if any, noticable result. This result implies the difference between equitemperature metamorphism and temperature gradient metamorphism is caused by the fact that the cold region gains mass from the warm region during the latter process. With this particular temperature gradient, the vapor mass flow is constant throughout the snowpack. Since mass is not being added to any region, we would not expect temperature gradient metamorphism to occur. Equitemperature metamorphism would then be the dominant mechanism.

Apparently, this has not been observed in nature. However, this is not surprising, nor does it imply this does not occur. When an observer studies the snowpack, he rarely knows the temperature profile that was present during the metamorphic process. Rather, he only sees its end result. If this hypothetical process had actually occurred, it

65

would simply be reported as equitemperature metamorphism. Further, it seems unlikely that this exact profile would exist frequently in nature.

Since there is a vapor flow in the snowpack, the second possible result is temperature gradient metamorphism, even though there is no net addition of mass to any region. This result implies the difference between temperature gradient metamorphism and equitemperature metamorphism is caused by the vapor flow in the former case providing condensation on a preferred side of the snow grain, with sublimation occuring on the opposite side (Fig. 7). This preferential construction would result in temperature gradient grains, even though there is no net mass addition.

Condensation   Sublimation

Vapor Flow (Constant)
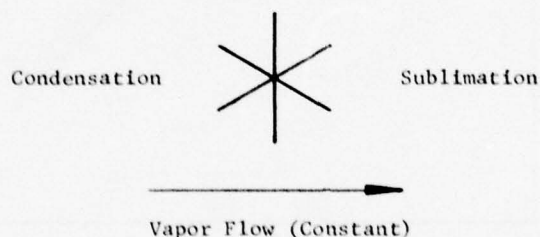
Figure 7   Preferential Grain Construction
Caused by Vapor Flow

It is known that temperature gradient grains grow in a direction opposite to the vapor flow. It is not known how much this growth depends on a net mass addition to the region as compared to how much it depends on the vapor flow. A series of experiments can easily be imagined:

1. Beginning with a uniform snowpack, impose the temperature profile of Figure 6 and observe the resulting process. Varying the snowpack thickness will vary the temperature gradients and the amount of vapor flow, but vapor flow will remain constant, with no net mass deposition in any one region. Thus grain growth could be studied as a function of vapor flow.

2. Beginning with a uniform snowpack, impose a linear temperature profile and observe the resulting process. Varying the snowpack thickness will vary the temperature gradient and the amount of mass deposition in the different regions of the snowpack. Thus grain growth could be studied as a function of mass deposition.

66

These experiments thus would focus on temperature gradient grain growth as a function of vapor flow and mass deposition. Unfortunately, they would be extremely difficult to perform.

V. Extension to Arbitrary Temperature Profiles

For an arbitrary temperature profile, Table 3 allows a plot of m vs location in the snowpack (Fig. 4). From Eqn (3), we see that areas of steepest slope correspond to areas of greatest vapor transfer. Areas of greatest change in slope correspond to areas of greatest crystal growth.

In practice, temperature gradients of 0.2°C/cm to 0.3°C/cm are considered to be strong gradients which will produce significant temperature gradient metamorphism (Ref. 1). Using the model, we may incorporate not only the effect of temperature gradient but also the effect of temperature itself on temperature gradient metamorphism. For example, a gradient of 0.3°C/cm at -40°C will not produce significant temperature gradient metamorphism, but a lesser gradient (say 9.2°C/cm) at -5°C would cause significant crystal growth. Obviously, more work is necessary before it would be possible to do quantitative predictions with this model.

VI. Conclusions

This simple model correctly demonstrates the dependence of temperature gradient metamorphism on both the temperature and temperature gradient. Warm areas in the snow-pack are shown to be consumed with the snow turning to vapor which then diffuses to the colder areas and condenses. This can either cause hollow layers or settlement, both of which are observed in nature. Essentially undisturbed layers remain at very cold temperatures.

The model suggests the possibility of a particular non-uniform temperature profile which might behave in a manner similar to equitemperature metamorphism. Apparently, this has not been observed in nature. However, without specifically looking for this process, it would probably have been reported as an equitemperature process.

Experimentation is needed to determine numerical values to use in the equations so
quantitative predictions could be made and to determine the relative dependence of the
temperature gradient process on vapor flow and mass deposition.

Table 1

VAPOR PRESSURE & VAPOR DENSITY DEPENDENCE ON TEMPERATURE (Ref. 2)

$T(^{o}C)$	$p_{H_2O}(N/m^2)$	$\rho_{H_2O}(Kg/m^3)$
-40	12.9	.011970
-30	38.1	.033979
-20	103.5	.088605
-10	260.2	.214270
0	610.8	.484731

Table 2

PROPERTIES OF AIR

$T(^{o}C)$	$p_{AIR}(N/m^2)^*$	$\rho_{AIR}(Kg/m^3)$
-40	101312	1.5151
-30	101287	1.4524
-20	101315	1.3955
-10	101299	1.3422
0	101264	1.2926

*Calculated from $p_{AIR} + p_{H_2O} = 1$ atm

68

Table 3

PROPERTIES OF THE MIXTURE

$T(^{o}C)$	m	$\rho_{mix}(Kg/m^3)$
-40	.007839	1.5271
-30	.022860	1.4864
-20	.059703	1.4841
-10	.137664	1.5565
0	.272730	1.7773

References

1. Perla, R. I. and Martinelli, M. Jr., Avalanche Handbook. U.S. Department of Agriculture, Forest Service. Agriculture Handbook 489.

2. Handbook of Tables for Applied Engineering Science, 2nd ed., Chemical Rubber Co., Cleveland, 1973.

3. Kays, W. M., Convective Heat and Mass Transfer, McGraw-Hill, New York, 1966.

PRESSURE DATA FROM THE OPEN PORT FLIGHT TEST
WITHOUT APT INPUT WINDOW

S. E. Icardi[*]

Abstract

Ground and flight tests were conducted with the Airborne Laser Laboratory to demon-
strate operation of the Airborne Pointing and Tracking (APT) System in the open port
configuration with the input window removed. Preliminary calculations were performed to
insure that a rapid decompression would not occur when the APT eyelid was opened against
a pressure gradient and that the air flow through the APT would not cause damage to
equipment or harm personnel. The preliminary estimates proved conservative. The meas-
ured dynamic loading inside the APT was low and the cabin pressure transients were
relatively slow and did not degrade flight or test crew performance.

I. Background

Flight testing has been conducted with the Airborne Laser Laboratory (ALL) to confirm
the feasibility of operating the Airborne Pointing and Tracking System (APT) without an
output window (Ref. 1). It was the conclusion of the testing that the open port con-
figuration appears to allow better beam focusing and more beam intensity on target than
the window configuration. These promising results have led to further investigation of
the open port as a candidate configuration for the APT. The open port tests were con-
ducted with a pressure seal between the aircraft and the APT. To be a viable config-
uration, it was clear that the open port had to be tested without an input window. For
follow-on tests the input window was removed from the bottom of the APT and operation of
the modified APT was demonstrated throughout a restricted ALL flight envelope. This
report discusses the very limited aerodynamic data measured during ground and flight
testing of the follow-on configuration.

II. Objective

The objectives of the testing program were to demonstrate operation of the APT in
the open port configuration with the input window removed and to conduct beam quality
experiments. The beam quality experiments were aimed at detecting beam degradation
caused by the increased flow through the beam path in the APT. The particular objectives
of the aerodynamic test program were first to insure, prior to flight, that the air flow
through the APT would not cause damage to equipment or injury to personnel, and second,
to measure the environmental, i.e. pressure, change in the cabin when the APT eyelid
was opened against a pressure gradient.

---

[*] Major, USAF, Instructor, DFAN

III. Method of Test

Testing of the open port APT with the input window removed was conducted in two
phases, ground testing and flight testing. The ground testing phase was included to
insure that the experiments could be performed safely under flight conditions. During
ground testing the aircraft was pressurized, using the aircraft pressurization system,
to sea level standard day pressure, 14.7 psia, approximately 2.5 psi higher than the
local ambient pressure. The APT eyelid was then opened and the APT parameters were
measured and recorded using the existing APT and aircraft instrumentation systems. A
pitot static system was installed at the base of the APT to measure the dynamic pressure
and air velocity in the opening created by removal of the input window, Figure 1. It is
assumed that this opening is the minimum restriction that the air flow will pass as it
leaves the cabin. Therefore, it sees the maximum air velocity and dynamic pressure.
Cabin pressure was recorded using the cabin pressure instrumentation installed in the
aircraft. Time histories of the cabin pressure, air velocity, and dynamic pressure were
made and compared to predicted values to insure the decompression of the cabin would not
harm personnel or the APT System.

Flight tests were conducted to gather data on APT performance and cabin pressure
transients as the azimuth angle of the APT was changed and to evaluate beam quality as
effected by the increased flow through the beam path. The only pressure data recorded
in the air were the cabin pressure transients as the APT eyelid was opened and the APT
was scanned in azimuth. The flight testing was conducted as described in Ref. 2. The
inflight measurements of cabin pressure versus time and APT azimuth are presented in the
results section of this report.

IV. Theory

Initial theoretical calculations were made to confirm the feasibility of such test-
ing. Preliminary analysis was run to calculate the cabin pressure transient as the eye-
lid was opened on the ground at Kirtland AFB with the cabin pressurized to sea level
standard day pressure. Additional calculations were then run under what were considered
to be the worst case flight conditions. Plots of cabin pressure versus time were
generated using the theory of conservation of mass as outlined below.

| Time rate of decrease
of mass in volume (V) | = | Net rate of outflow of mass
across the boundary |

$$- \frac{\delta}{\delta t} \int_V \rho \, dV = \int_A \rho \, (\bar{v} \cdot \tilde{N}) dA \qquad (1)$$

71
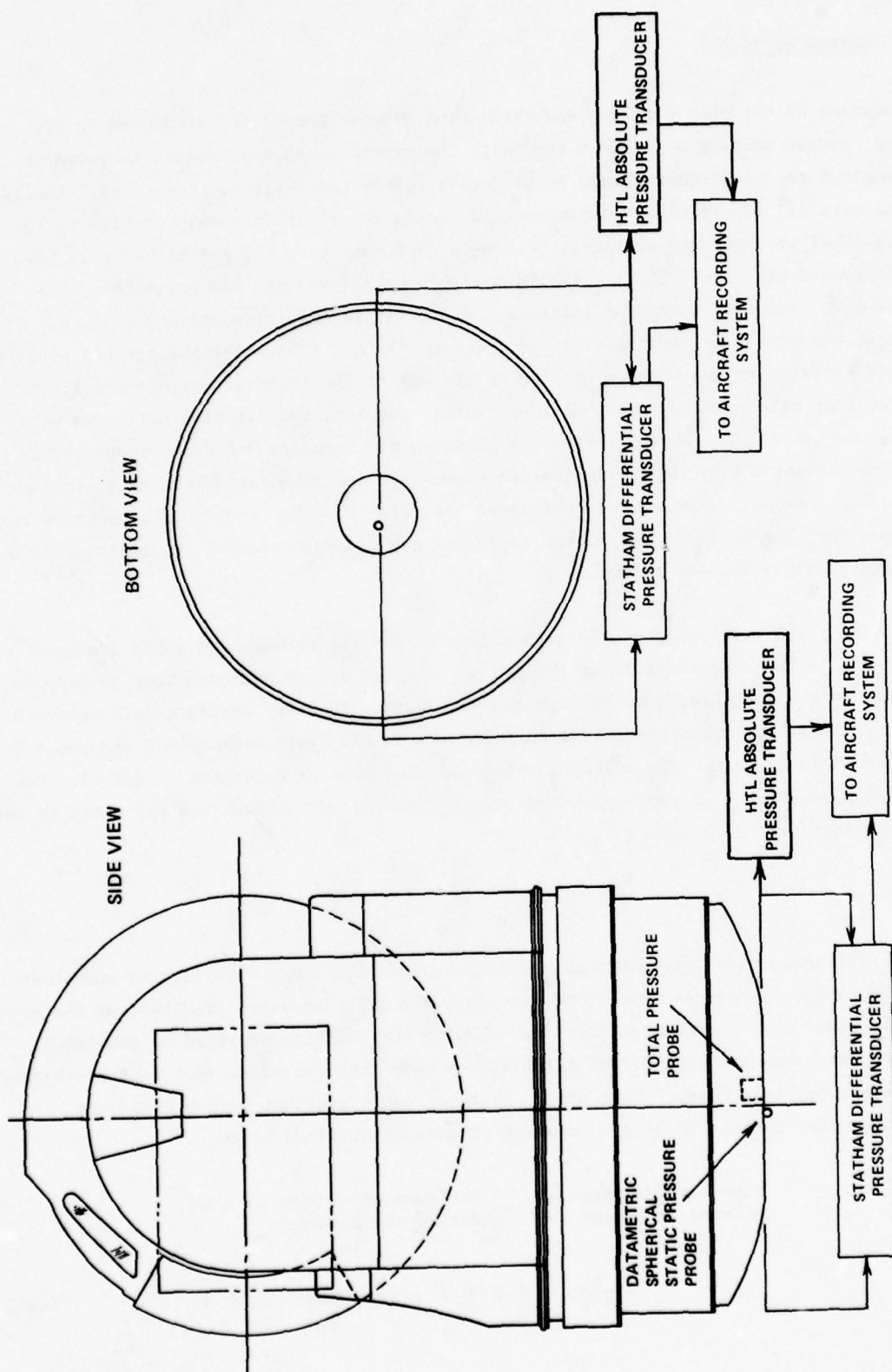
Figure 1. Installation of Pressure Instrumentation for Ground Test

where   t = time (s) $\vec{N}$ = surface normal vector

ρ = density of air $\left(\text{lbm}/\text{ft}^3\right)$ A = surface area (ft^2)

V = volume (ft^3)

$\vec{v}$ = velocity vector (ft/s)

for steady flow

$$\int \rho \, (\vec{v} \cdot \vec{N}) dA = 0$$

or one dimensionally

$$\dot{m} = \rho A v = \text{constant}$$

where

$$\dot{m} = \text{mass flow rate} \ (\text{lbm}/\text{s})$$

$$v = \text{velocity magnitude} \ (\text{ft}/\text{s})$$

Applying the perfect gas relation ($p = \rho RT$) and the Mach relation $\left(M = \dfrac{v}{\sqrt{\gamma RT}}\right)$, for air, $\dot{m}$ then becomes :

$$\dot{m} = \frac{p}{RT} \ A \ M \ (49.05) \ \sqrt{T} \tag{2}$$

For adiabatic perfect gas, $\gamma = 1.4$

$$\frac{T}{T_o} = \left(1 + \frac{\gamma - 1}{2} M^2\right)^{-1} = \left(1 + \frac{M^2}{5}\right)^{-1}$$

Substituting for T

$$\dot{m} = \frac{pA}{\sqrt{R \, T_o}} \ \sqrt{M^2 + \frac{M^4}{5}} \qquad \left(\gamma = 1.4\right) \tag{3}$$

Now $\dot{m}$ may be calculated by knowing the static pressure (p), Mach number (M), area of interest (A), and total temperature (T_o).

As a conservative estimate we can assume no pressure losses through the APT. The static pressure at the outlet then corresponds to the static pressure outside the opening in the APT. By the isentropic relationship, the Mach number is related to the outside pressure (p) and the cabin pressure (p_o) by:

$$M^2 = \left[\left(\frac{p}{p_o}\right)^{-2/7} - 1\right] 5 \tag{4}$$

73

We now have estimates for M and p and only need to estimate the cabin air temperature (T_o) and the surface area of the outlet (A) to solve for $\dot{m}$. This is an instantaneous value of $\dot{m}$ and must be adjusted as the cabin pressure is reduced. If we assume that $\dot{m}$ is constant over some small unit of time (Δt), we can estimate the change in pressure in the cabin by again applying conservation of mass.

$$\begin{array}{ll} \text{Mass flowing out of} & = \text{ Net decrease in mass} \\ \text{cabin in time } \Delta t & \text{ in cabin} \end{array}$$

$$\dot{m} \, \Delta t = \Delta \text{Mass} = \Delta \rho_o \, (\text{Vol})$$

From perfect gas $(\rho = \dfrac{p}{RT})$

$$\Delta \rho_o = \frac{\Delta P_o}{RT_o} \quad \text{if } T_o \text{ is constant}$$

By substitution then

$$\dot{m} \, \Delta t = \frac{\Delta P_o}{RT_o} \, (\text{Vol})$$

or the change in cabin pressure

$$\Delta P_o = \frac{\dot{m} \, \Delta t \, RT_o}{\text{Vol}} \tag{5}$$

where $\dot{m}$ = instantaneous mass flow rate $(\text{lbm}/_s)$

R = gas constant for air $\left(\dfrac{\text{ft} - \text{lbf}}{\text{lbm} \, ^\circ R} \right)$

T_o = cabin air temp $(^\circ R)$

Δt = time interval (s)

Vol = cabin volume (ft^3)

Since

$$P_{o_{new}} = P_o - \Delta P_o$$

then

$$M^2_{new} = \left[\left(\frac{p}{P_{o_{new}}} \right)^{-2/7} - 1 \right] 5$$

with M^2_{new}, we solve for a new $\dot{m}$, using Equation 3. We can set up an iterative process to solve for P_o at each Δt which results in a plot of cabin pressure (P_o) versus
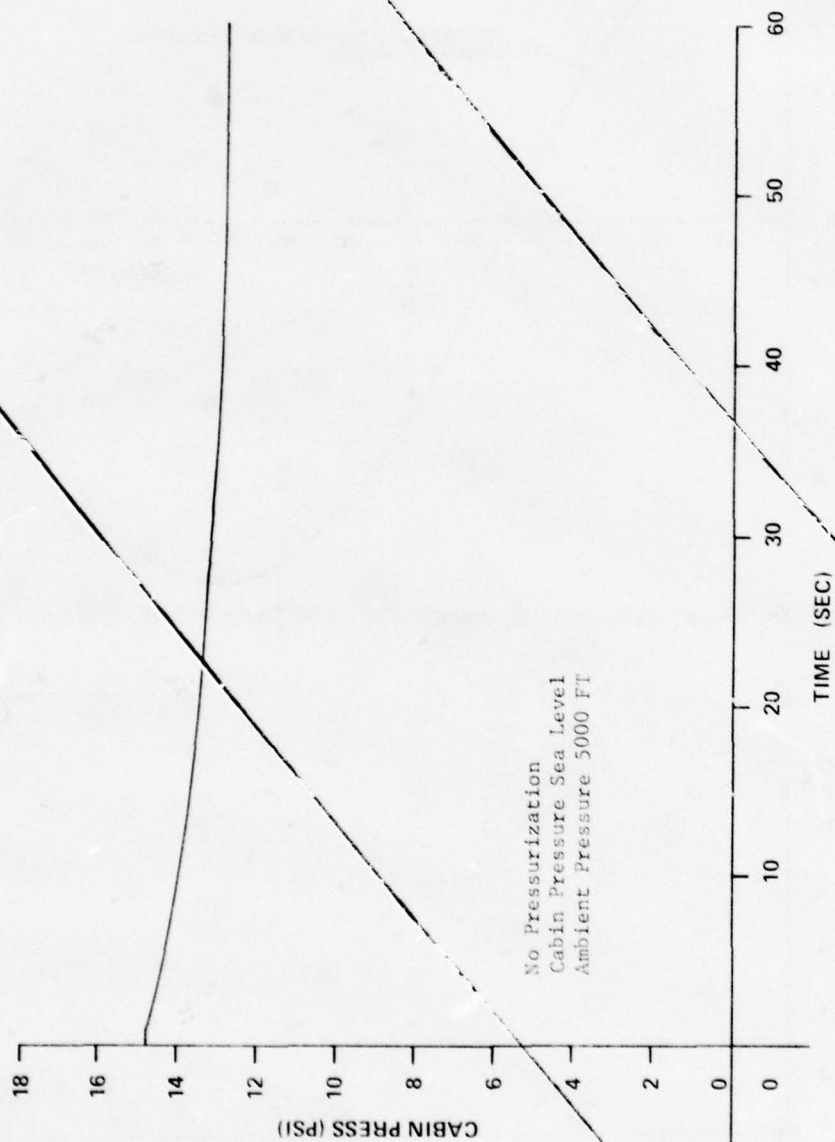
74

No Pressurization
Cabin Pressure Sea Level
Ambient Pressure 5000 FT

Figure 2. Theoretical Time to Equalize Cabin Pressure to Ambient Pressure for Ground Test Conditions

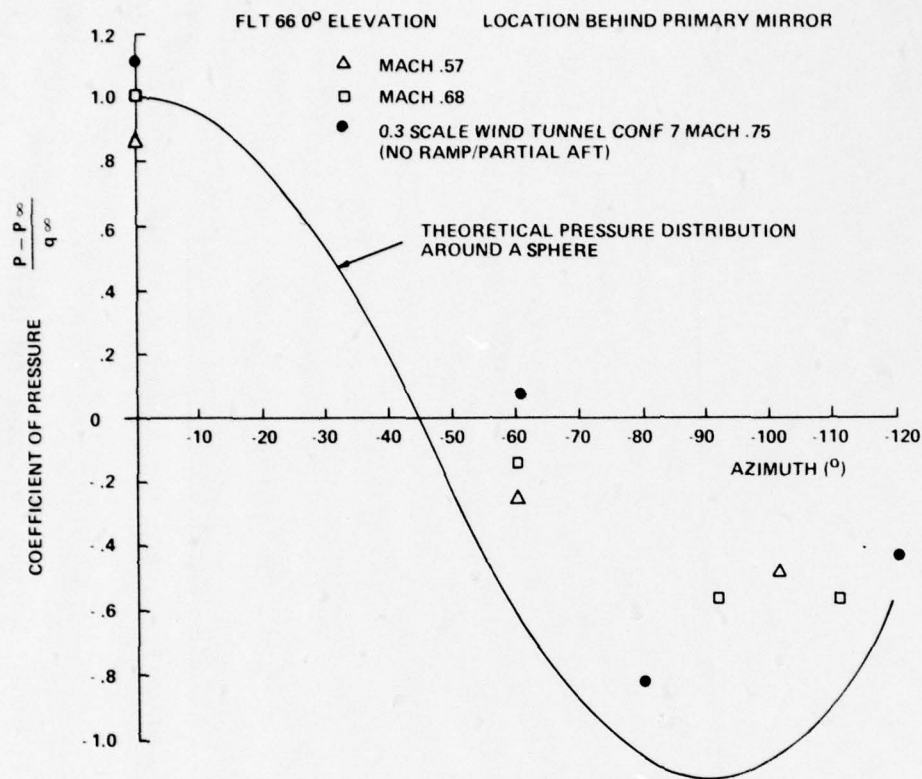FLT 66 0° ELEVATION   LOCATION BEHIND PRIMARY MIRROR

△   MACH .57

□   MACH .68

●   0.3 SCALE WIND TUNNEL CONF 7 MACH .75
    (NO RAMP/PARTIAL AFT)

THEORETICAL PRESSURE DISTRIBUTION
AROUND A SPHERE

$\frac{P - P_\infty}{q_\infty}$

COEFFICIENT OF PRESSURE

AZIMUTH (°)

Figure 3.   Variation of Cavity Interior Steady Pressure with Turret Azimuth Angle (ref. 2)

CABIN PRESSURE (PSI)

TIME (SEC)
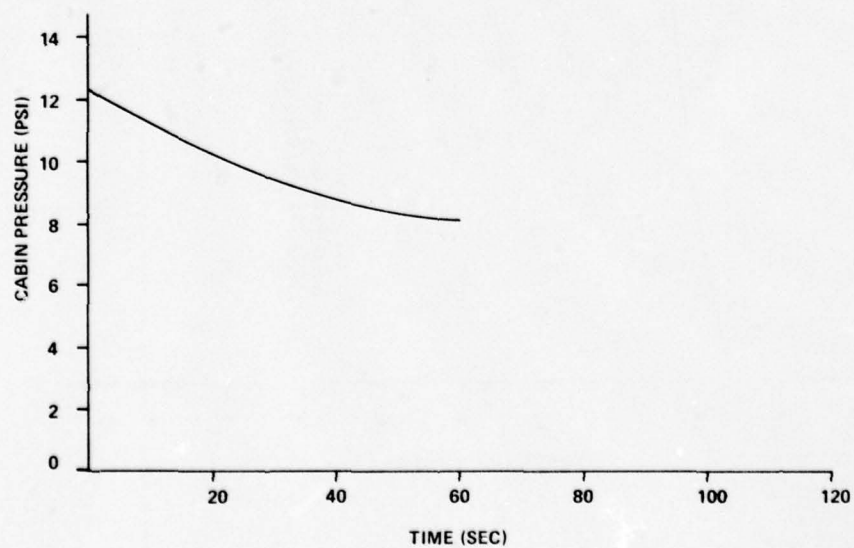
Figure 4.   Theoretical Time to Equalize Cabin to Ambient Pressure,
No Pressurization. Worst Case: 12,000 ft Mach 0.66
Azimuth Angle 110°

76

time. Figure 2 is a plot of the initial theoretical analysis of cabin pressure versus time. Initial conditions are similar to those that were set in the ground test. In this calculation cabin pressure (P_o) was assumed to be initially at sea level pressure (14.7 psi), outlet static pressure (P) at 5000 ft pressure altitude (12.2 psi), cabin temperature (T_o) constant at $70°F$ and outlet area (A) 11.45 in^2. Test point 1C from Ref. 2 at turret azimuth angle $110°$ was selected as the flight worst case since it presented the largest pressure differential between cabin pressure and outlet static pressure. The cabin pressure (P_o) was assumed to be 5000 ft pressure altitude (12.2 psi), the outlet static pressure (P) was estimated at 8.0 psi using pressure coefficients obtained during flight certification of the open port configuration, see Figure 3, cabin temperature (T_o) constant at $70°$ and the outlet area (A) 11.45 in^2. Figure 4 show the results of these calculations. The primary purpose of the calculations was to show that even with instantaneous opening of the APT eyelid under worst possible flight conditions there was no chance of an "explosive" rapid decompression.

An additional concern of safety personnel was the flow velocity around the opening in the bottom of the APT. The velocity field around the opening was calculated using conservation of mass and assuming perfect gas, steady and isentropic flow.

Let us assume that

$$\dot{m} = \rho \, Av = constant$$

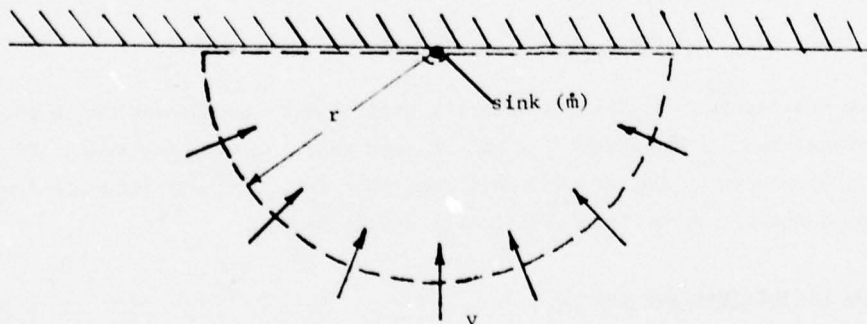and that we have a sink located next to a solid wall.

Figure 5. Control Volume for Mass Flow Calculations

Now assume a half spherical control volume as shown in Figure 5 above. The mass that flows into the sink is denoted by $\dot{m}$. This mass must from conservation of mass be equal to the mass flux through the half spherical surface area around the sink ($\rho \, v \cdot r^2$).

Then $\dot{m} = \rho v 2 \pi r^2$

where ρ = density of air (lbm/ft^3)

r = radius from sink to spherical surface area (ft)

v = velocity normal to surface (ft/s)

It is possible to neglect compressibility, since the velocity at a very short radius from the sink is well below Mach 0.5.

The density then becomes constant and equal to the density of the air in the cabin. The initial velocity profile can now be calculated as a function of the radius of the spherical area,

$$v = \frac{\dot{m}}{\rho \, 2 \, \pi \, r^2} \qquad (6)$$

if the initial mass flow $\dot{m}$ and the cabin air density ρ are known.

Assuming perfect gas relation

$$\rho = \frac{P}{RT}$$

$$v = \frac{RT_o}{2 \pi P_o} \frac{\dot{m}}{r^2} \qquad (7)$$

where T_o = cabin temperature ($^\circ R$)

P_o = cabin pressure (lbf/ft^2)

Figure 6 shows the theoretical initial velocity distribution as the radius of the spherical surface area is increased. It can be seen that the velocity drops off very quickly and is less than 10 fps at 10 inches from the sink. The velocity field around the opening does not appear to be a significant safety hazard.

V. Ground and Flight Test Results

The ground tests were conducted by pressurizing the aircraft to sea level standard day pressure (14.7 psia) and then opening the APT eyelid. The cabin pressure was recorded using the aircraft system. Static and total pressures were recorded at the opening in the base of the APT. Figure 7 is a plot of the change in cabin pressure with time. It is interesting to compare this measurement with the theoretical estimate (Figure 2) for the ground test. The theoretical estimate, though based on several rather critical assumptions, proved to be a conservative calculation.
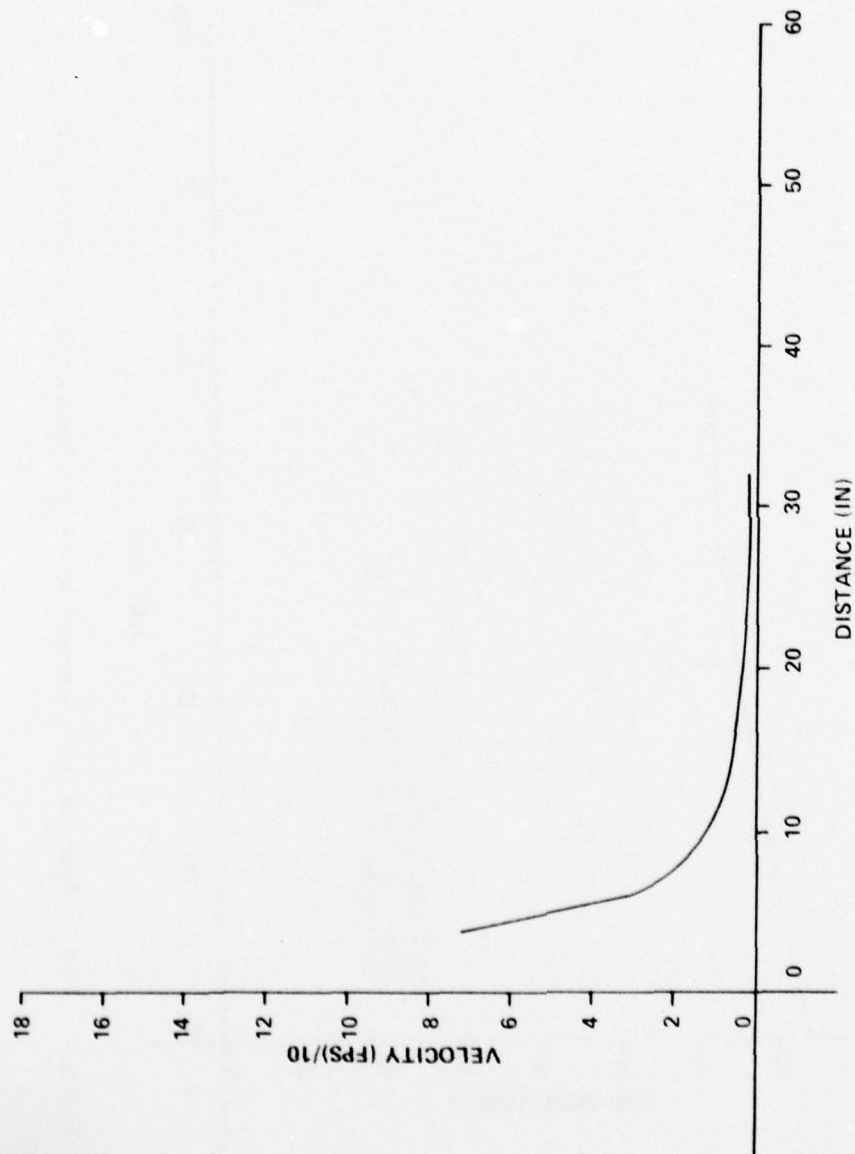
Figure 6. Theoretical Estimate of Flow Velocity Below the APT, Worst Case: 12,000 Ft,
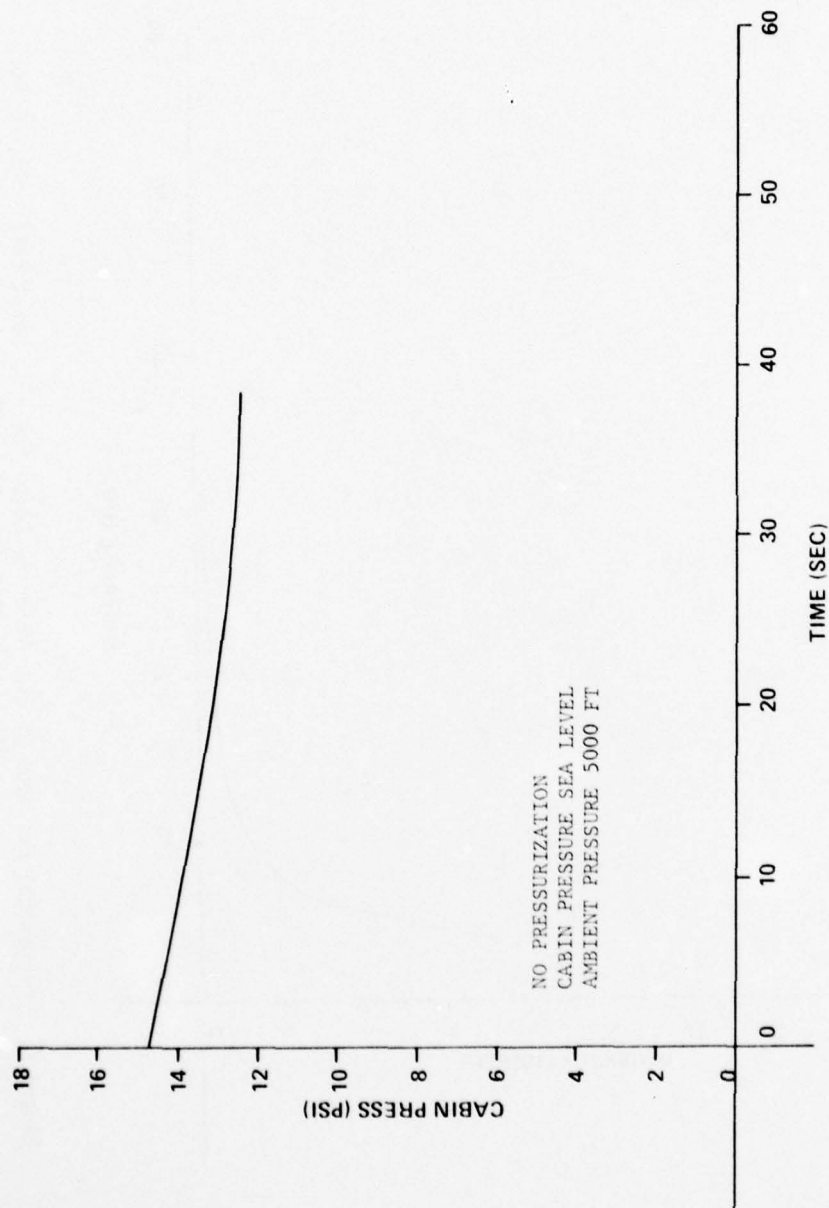Mach 0.66, Azimuth Angle 110°

79

Figure 7. Time to Equalize Cabin Pressure to Ambient Pressure During Ground Test

NO PRESSURIZATION
CABIN PRESSURE SEA LEVEL
AMBIENT PRESSURE 5000 FT

The velocity and dynamic pressure calculations were made from the pitot-static data. Figure 8 is a plot of the change in velocity with time. It can be seen that the velocity never exceeds 200 fps which at a cabin altitude of 5000 ft corresponds to Mach 0.18. In the theory section we showed that the velocity dissipates very quickly as the distance is increased away from the opening. Figure 9 shows the change in dynamic pressure with time. The maximum dynamic pressure was measured to be 0.27 psi, the dynamic pressure was well below any structural limit on the APT.

The pitot static system was removed from the base of the APT for the flight test, since propagation data was required on this flight. The cabin pressure was recorded during opening of the APT eyelid and also through an azimuth scan of the turret. Figure 10 shows the cabin pressure response versus time for a typical opening of the APT eyelid. A comparison of the theoretical results (Figure 4) shows a favorable agreement in the data. This pressure response is similar to what might be seen if the turret was rotated at max speed from an azimuth angle of zero degrees to 90 degrees. Figure 11 is a plot of the change in cabin pressure as azimuth angle is varied. For this data, azimuth angle was rotated slowly so that cabin pressure was essentially stabilized at each point. The largest pressure changes occur between 30° and 80°, which corresponds to the changes in external pressures on the APT as recorded during earlier flight tests and noted in Figure 3.

VI. Conclusions and Recommendations

The primary objective of these tests was to show that the aerodynamic environment due to changing cabin pressure would not cause damage to equipment or injury to personnel. Tests show that aerodynamically there is no reason to prevent operation of the APT without output and input windows. Dynamic loading inside the APT is low, and cabin pressure transients are relatively slow and will not degrade flight or test crew performance.

References

1. Icardi, S. E., "Pressure Measurements from Airborne Laser Laboratory Open Port Flight Test", AFWL TR-76-170, Air Force Weapons Laboratory, Kirtland AFB, NM, 1977.

2. "Test Plan: Advanced Radiation Technology Program, Airborne Laser Laboratory Project, Cycle II, APT Open Port with No Input Window Test", 4900th Test Group; Air Force Special Weapons Center; Kirtland AFB, NM; 19 December 1975.
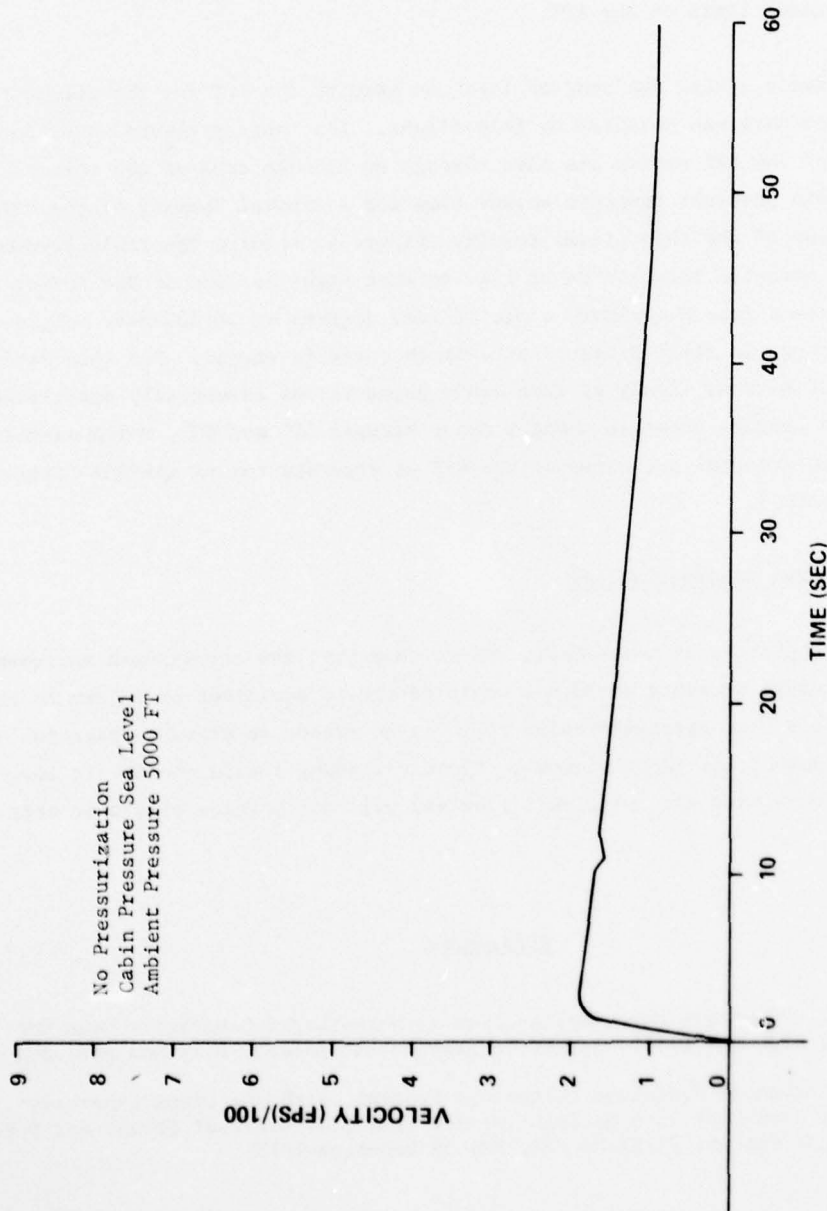
No Pressurization
Cabin Pressure Sea Level
Ambient Pressure 5000 FT

VELOCITY (FPS)/100

9
8
7
6
5
4
3
2
1
0

5   10   20   30   40   50   60

TIME (SEC)

Figure 8. Air Velocity at Base of APT During Ground Test

No Pressurization
Cabin Pressure Sea Level
Ambient Pressure 5000 FT

DYN PRESS (PSI)

TIME (SEC)
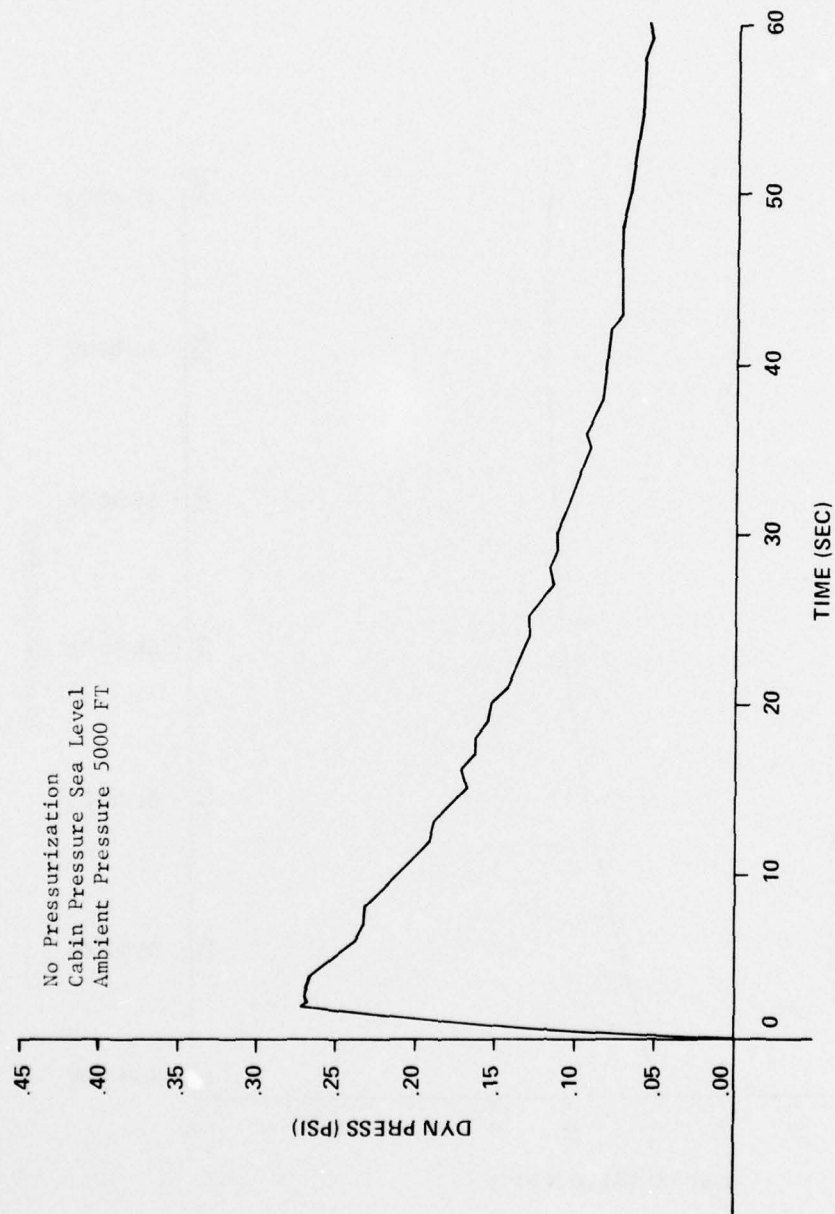
Figure 9. Dynamic Pressure at Base of APT During Ground Test

FLIGHT 88
MACH .55
ALTITUDE 11,000 FT
EYELID OPENING AZ 90°

CABIN PRESSURE (PSI)

TIME (HR:MIN:SEC)
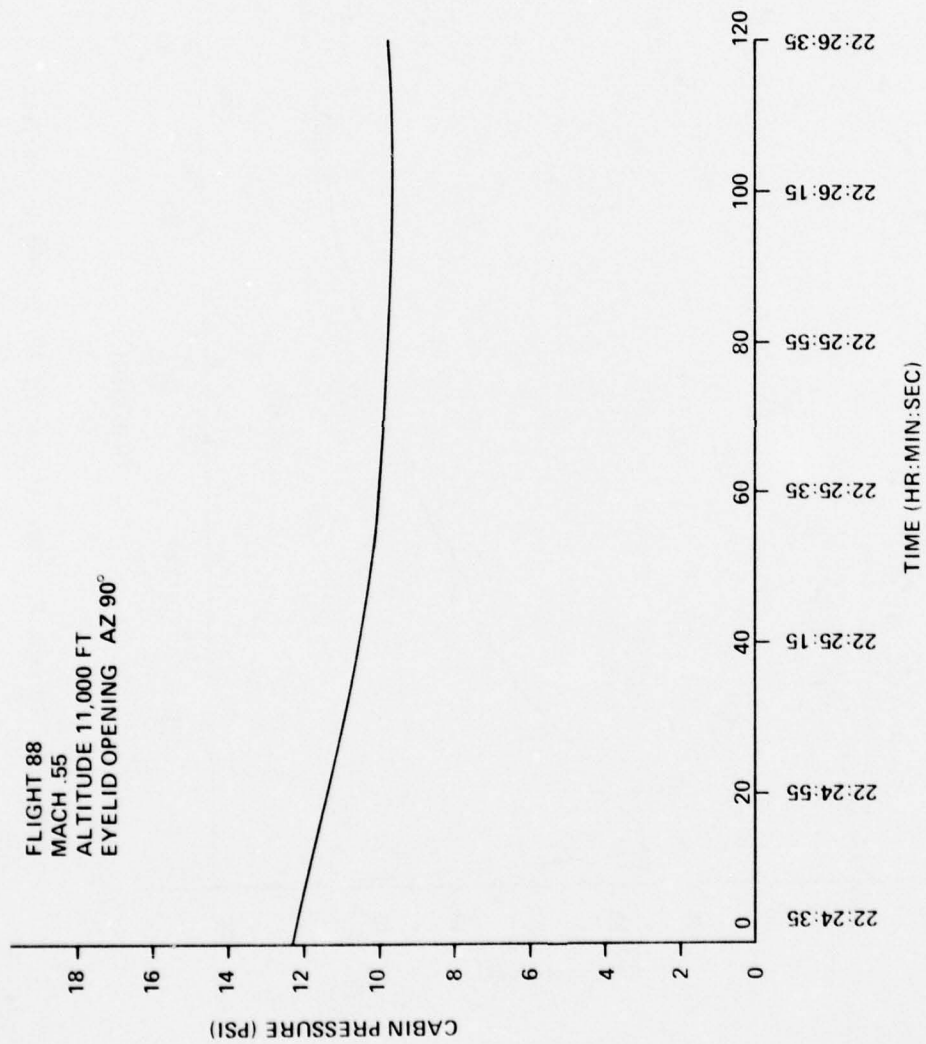
Figure 10. Time to Equalize Cabin Pressure to Ambient Pressure During Eyelid Opening, Flight Test, Pressurization On

84

FLIGHT 88
MACH .63
ALTITUDE 11,000 FT
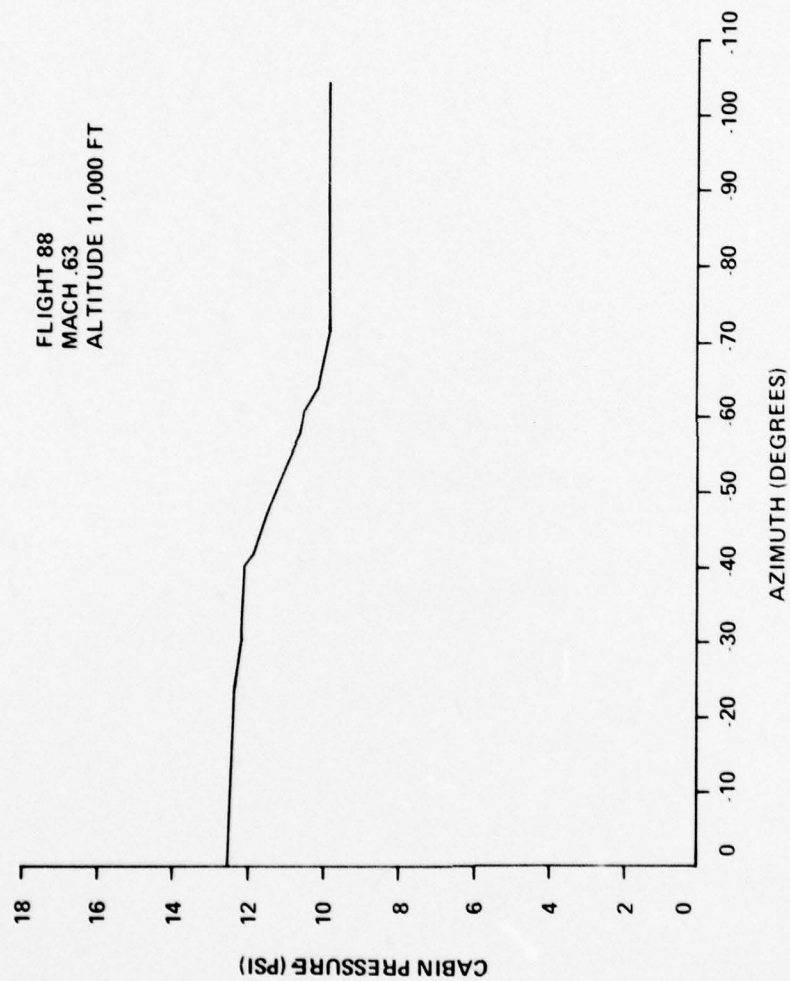
Figure 11. Variation of Cabin Pressure with Azimuth Angle During Flight Test, Pressurization

SECTION III

THERMODYNAMICS

AND

HEAT TRANSFER

CONVECTIVE HEAT TRANSFER AUGMENTATION BY
COMBINED TECHNIQUES

R. C. Oliver[*] and D. N. Black[**]

Abstract

Current Air Force developments in lasers and advanced propulsive systems have demon-
strated the requirements for high rates of heat transfer. Many augmentative techniques
exist and this paper reports on the experimental evaluation of a combination of two of
the most promising convective techniques, nucleate boiling and surface promoters.
Results indicate that these techniques can be used in concert, with additive effects; no
detrimental effects were noted in the range investigated.

I. Introduction

Current Air Force and industry research and development efforts have illuminated a
requirement for enhanced heat transfer rates. Several specific areas of application are
laser mirrors and turbine blade cooling. Increased heat transfer techniques could also
be employed in many standard cases resulting in decreased heat exchanger size or increased
performance or efficiency. Successful developments of some advanced systems may require
the use of augmentative heat transfer devices.

The baseline case for convective heat transfer is a constant area, smooth, straight
channel with only gravitational forces present. The multitude of available techniques
are found in several publications, those by Bergles (Ref. 1 and 2) being perhaps the
most complete. Very briefly the techniques range from passive, where some surface treat-
ment is considered, to active, where mechanical devices, vibration, injection or suct-
ion and electro-magnetic fields are employed. Additionally, devices such as swirl flow,
surface tension or additives comprise another distinct class (displaced promoters).
Add to this the application of these techniques to either boiling or non-boiling proc-
esses and you began to see the magnitude of the possible combinations. Of course,
combined techniques of any two or more of the basic techniques employed simultaneously
should also be considered while seeking the "optimum" augmentative device.

Bergles summarizes the research to 1973 by noting that passive techniques appear
most practical in the near term and that the only active techniques having present
practical utility are mechanical aids. He also noted that work on compound techniques
should be extended, as the few available studies indicate an increased effectiveness
(Ref. 2).

[*]Major, USAF, Instructor of Aeronautics, DFAN

[**]C1C, USAF Academy

II. Theory

The system selected for study was a displaced promoter with nucleate boiling. Types of displaced promoters include disks, inserts, ring inserts, etc. with the purpose of tripping the boundary layer. The repeated disruption of the boundary layer reduces the boundary layer thickness and enhances the heat transfer.

Theoretically this effect is shown by considering the local Nusselt number developed for laminar flow but also applicable to turbulent flow (Ref. 3):

$$N_{u_x} = .332 \, Pr^{\frac{1}{3}} \, Re_x^{\frac{1}{2}} \tag{1}$$

or

$$h_x = k \, \frac{.332 \, Pr^{\frac{1}{3}}}{\sqrt{\nu x / U_\infty}} \tag{2}$$

Where N_{u_x} is the local Nusselt number, Pr the Prandtl number and Re_x the local Reynolds number. Further, h, k, ν, x, and U_∞ are the convective heat transfer coefficient, thermal conductivity, viscosity, distance, and the velocity, respectively. From this we note that as the boundary layer distance, x, is decreased toward zero, h tends towards infinity, which is certainly in the right direction.

The validity of this trend has been verified by a number of researchers listed by Bergles (Ref. 4), while Webb and others have developed predictive techniques for repeated rib or ring geometry using non-boiling flows (Ref. 5 and 6).

It was our goal to demonstrate that this augmentation could be maintained in conjunction with nucleate boiling enhancement, to verify that the effects are additive. Additionally, consideration of the effect of the promoters must also include changes in the critical heat rate. Yang reported a 15-30% reduction of sub-cooled burnout heat fluxes due to large scale roughness (Ref. 7). Bergles noted that surface conditions do not appear to significantly alter the boiling curve for reasonably high flow velocities (Ref. 8), while Durant noted an increase in sub-cooled critical heat flux with relatively course mechanical roughness (Ref. 9). Gambill, using swirl flows, reported on increase of 200% in the critical heat flux (Ref. 10). In summary, we must eventually consider the effect of such augmenters on the critical heat rate; this effect appears to be presently undetermined. The experimental plan reported here includes investigations of convective flow with nucleate boiling with and without the use of a displaced promoter. The critical heat flux was investigated but not quantified. Primary emphasis was in the boiling phase prior to the critical heat rate.

III. Experimental Design and Data Collection

The experiment was conducted in the Physical Chemistry Laboratory at the U.S. Air Force Academy from October through December 1977. The test apparatus consisted of an aluminum finned surface, 11.43 by 11.43 cm by 1.9 cm thick. Uniform two dimensional fins 1.27 cm thick were used on the fluid side in the direction of flow. The fins maintained flow direction and increased the heat transfer from a TEMCO Hot Plate Model HP-1915B mounted under the non-finned side of the device. Plexiglass mounted across the device (on the fins) formed a water tight apparatus. A manifold at each end introduced and removed water. Iron-constantan thermocouples were used to measure the incoming and exit fluid bulk temperatures as well as the device surface temperature. Mass flow rates were measured with a graduated cylinder.

A typical run would commence at an established mass flow and heat rate below the onset of nucleate boiling. Heat transfer parameters were noted in the steady state and then the heat rate was increased. A number of points were sampled 10 to 15°F apart until the critical heat rate was approached.

Several configurations were tested. The baseline condition was the clean configuration, as previously described. Modifications using wires forming rectangular ring inserts were installed and tested. Densities of 0.3937 and 0.8 inserts per centimeter (spacing of 2.54 and 1.27 cm) were examined. Data collection for these cases was as described for the baseline case.

IV. Discussion

The experimental data were reduced and plotted as the rate of heat transfer versus the surface-fluid bulk temperature difference. Figure 1 presents the results of all three cases, forced convection with nucleate boiling, clean and with both insert configurations.

As the figure illustrates, the critical heat rate was reached at a smaller temperature difference for the two cases using wire inserts for boundary layer disruption. The critical heat rate for the baseline case occurred at a temperature difference (surface - fluid bulk) of 175°F. For the lower insert density treatment the temperature difference was 125°F. The higher density treatment resulted in temperature difference of 100°F. From the data analyzed, no significant difference in the critical heat flux was observed for these treatments. If higher fluxes were used perhaps some differences would be noted. However, the object of this study was heat transfer below the critical flux. The increase in insert density, then results in enhanced convection. For a given flux the decrease in the temperature difference is indicative of an increased convective heat transfer coefficient.
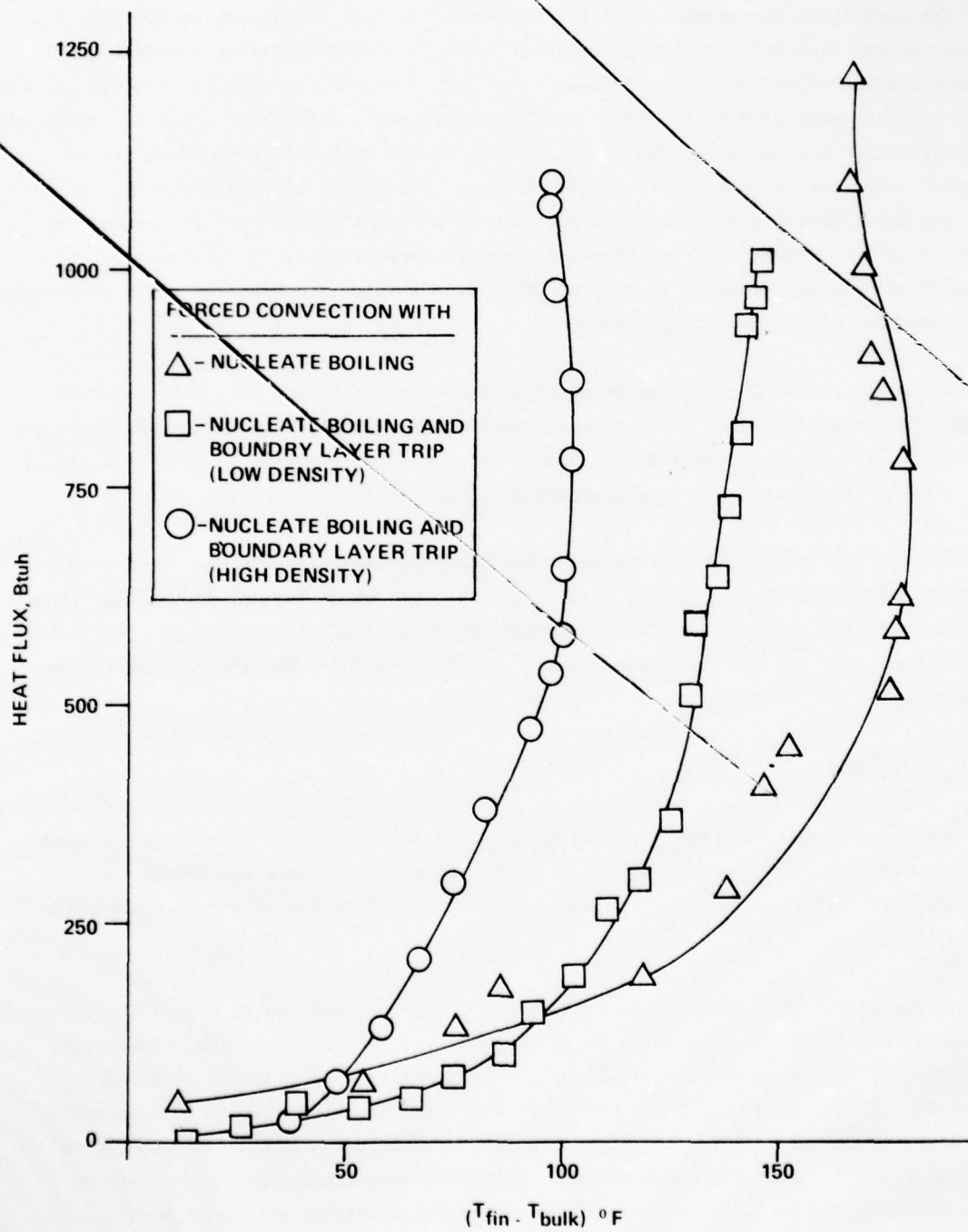
Figure 1. Heat Flux as a Function of Temperature Difference
For Nucleate Boiling with Various Geometries

90

Heat transfer coefficient to the maximum temperature difference in each case resulted in values of 23.71, 41.03, and 71.20 BTUH per Sq Ft-$^\circ$ F. The absolute values of these coefficients is low because of the limited mass flow rate. The flow had to be maintained at low rates to insure reaching the critical flux with the fixed power heater. The possibility of different results at higher flow rates must be considered and experiments should be performed to confirm this result. Such determination was beyond the scope of this effort.

V. Conclusion

The data collected indicated that the use of displaced promoters, namely rectangular inserts, increases heat transfer rates for flows where nucleate boiling is present. For systems using nucleate boiling, then, the additional use of inserts will increase the heat transfer rates. No mention of the increased pressure loss is made, but its effect must also be considered. It is also highly likely that even a third or fourth technique could be coupled with these to further increase the heat transfer rate. Specifically, fluid additives and surface treatments which increases the nucleation sites should be considered.

The data collected and presented here imply that further increases in the insert density will further increase the heat transfer rate. While this is true, based on both theory and the reported results, the rate of increase decreases with increasing insert density (diminishing returns). The optimum design would have to consider the increased pressure losses, initial cost and operating expenses, perhaps more frequent defouling. The combined techniques do, however, have additive effects and can be used in concert to further increase heat transfer rates.

The data collected are not deemed sufficiently general in flow and heat transfer rates to justify empirical predictive equations. The data do, however, indicate the possibility of using these two techniques in concert and encourages the research into the use of additional techniques with these or other combined techniques.

References

1. A. E. Bergles, "Survey and Evaluation of Techniques to Augment Convective Heat and Mass Transfer,"Progress in Heat and Mass Transfer, Vol. 1, Pergamon Press, pp 331-424, 1969.

2. A. E. Bergles, "Recent Developments in Convective Heat-Transfer Augmentation," Applied Mechanics Review, Vol. 26, No. 6, pp 675-682, 1973.

3. W. M. Kays, Convective Heat and Mass Transfer, McGraw-Hill, pp 280, 1976.

4. A. E. Bergles, "Techniques to Augment Heat Transfer", Handbook of Heat Transfer, edited by W. M. Rohsenow and J. P. Hartnett, McGraw-Hill, pp 10-1 - 10-32, 1973.

5. R. L. Webb, E. R. G. Eckert, and R. J. Goldstein, "Heat Transfer and Friction in tubes with Repeated - Rib Roughness", Int. J. Heat Mass Transfer, Vol. 14, Pergamon Press, pp. 601-617, 1971.

6. R. L. Webb and E. R. G. Eckert, "Application of Rough Surfaces to Heat Exchanger Design", Int. J. Heat Mass Transfer, Pergamon Press, pp 1647-1658, 1972.

7. W. J. Yang, "Enhancement of Convective Heat and Mass Transfer", Improving Heat Exchanger Design, a collection of information for a Short Course, 1975.

8. Ibid, Bergles, p. 10-7, 1973.

9. W. S. Durant, R. H. Towell, and S. Mirshak, "Improvement of Heat Transfer to Water Flowing in an Annulus by Roughening the Heated Wall", Chem. Eng. Symp., Ser. 61, Vol. 60, p. 106, 1965.

10. W. R. Gambull, R. D. Bundy, and R. W. Wansbrough, "Heat Transfer, Burnout, and Pressure Drop for Water in Swirl Flow through Tubes with Internal Twisted Tapes", ORNL 2911, 1960.

LASER INDUCED HEATING: PREDICTION OF FRONT SURFACE MELTING TIMES[*]

Raymond A. Shulstad[**]

Abstract

A critical thickness for a slab subjected to laser radiation is defined. It is then shown that for slabs of thickness greater than this critical thickness a simple equation, derived from a half-space solution to the heat equation, may be used to predict front surface melting times. In addition it is shown that for thin slabs, of thickness less than three-fifths of the critical thickness, another simple equation may be used to compute melting times. Further, front surface melting times for slabs of intermediate thickness are shown to be bounded by the times computed from the two equations cited above.

I. Introduction

An important parameter in any investigation of the effects of high-power laser radiation on solids is the time required to melt the front surface. Two elementary solutions of the heat conduction equation as given by Carslaw and Jaeger (Ref. 1) are particularly useful for predicting surface thermal response up to the time when the front surface begins to melt. These solutions assume one dimensional heat flow and neglect radiative and convective losses.

The front surface temperature of a half-space of thermal conductivity k and diffusivity κ initially at temperature T_o and subjected to a flux of uniform intensity I with a fraction α absorbed at the surface is:

$$T_{surf} = T_o + \frac{2\alpha I}{k} \left(\frac{\kappa t}{\pi} \right)^{\frac{1}{2}} \tag{1}$$

The time to initiate front surface melting, τ_∞, is calculated in equation 2:

$$\tau_\infty = \frac{\pi}{\kappa} \left(\frac{k\Delta T_m}{\alpha I} \right)^2 \tag{2}$$

where $\Delta T_m = T_{melt} - T_o$.

If a critical thickness, ℓ_{crit}, is defined as:

$$\ell_{crit} = \frac{2.2 \, k \, \Delta T_m}{\alpha I} \tag{3}$$

then equation 2 may be rewritten as:

$$T_\infty = \frac{\pi}{4\kappa \ (2.2)^2} \ \ell^2_{crit} \tag{4}$$

It will be shown in this paper that if a <u>slab</u> is of thickness greater than ℓ_{crit}, then the time required to melt its front surface is also given by equation 4 (i.e., the same as predicted by the half-space equation).

For uniform absorbed flux, αI, on the surface of a homogeneous slab of thickness ℓ, the front surface temperature is given by:

$$T_{surf} = T_o + \frac{\alpha I \kappa t}{k\ell} + \frac{\alpha I \ell}{3k} - \frac{2\alpha I \ell}{\kappa \pi^2} \sum_{m=1}^{\infty} \frac{e^{\frac{-m^2 \kappa \pi^2 t}{\ell^2}}}{m^2} \tag{5}$$

Equation 5 is transcendental, and an iterative procedure must be used if melt times are desired. For thin slabs ($\kappa \pi^2 \ t/\ell^2 >> 1$) equation 5 can be reduced to

$$T_{surf} = T_o + \frac{\alpha I \kappa t}{k\ell} + \frac{\alpha I \ell}{3k} \tag{6}$$

from which the time required to initiate front surface melting, τ_{s1}, is given by

$$\tau_{s1} = \frac{\ell k \ \Delta T_m}{\alpha I} - \frac{\ell^2}{3\kappa} \tag{7}$$

Using equation 3, τ_{s1} is also found to be

$$\tau_{s1} = \frac{\ell}{2.2\kappa} \ \ell_{crit} - \frac{\ell^2}{3\kappa} \tag{8}$$

It is interesting to note that the first term in equation 7 is the melting time for a very thin slab under uniform heating conditions (i.e., $dT/dx = 0$).

Thus, it is seen that front surface melting times are easily calculated for "thick" slabs via equation 4 and for "thin" slabs via equation 8, but one must work considerably harder to determine melting times for slabs of intermediate thicknesses. This investigation establishes the range of applicability of equation 4 and 8 in terms of the critical thickness, ℓ_{crit}, defined in equation 3 and derived in the next section of this paper. It will also be shown that melting times as predicted by equations 4 and 8 may be used to bound the actual melting time of slabs of intermediate thicknesses.

II. Definition of Critical Thickness

An iterative procedure was developed to compute front surface melting times for slabs

94

of various materials and thicknesses (Eq 5) and intensities. These times were compared to τ_∞, the time required to melt the front surface of a half-space subjected to the same flux (Eq 2). Figure 1 depicts typical results obtained in these studies. The results of these comparisons suggested the existence of a "critical thickness" which is defined to be the minimum thickness where the time required to melt the front surface of the slab is equal to the time predicted by the half-space solution (τ_∞).

With this definition in hand, information as to what factors determine critical thickness was sought. By requiring the front surface of the slab to melt at time equal τ_∞, it was found that

$$z = \frac{\ell \alpha I}{k \, \Delta T_m} \tag{9}$$

seemed to be a fundamental dimensionless parameter. Utilization of critical thickness data acquired in the comparison study described above showed that

$$\ell_{crit} = \frac{z \, k \, \Delta T_m}{\alpha I} \tag{10}$$

where $z \approx 2.2$.

Critical thicknesses and corresponding "z values" for a varity of metals are presented in Table 1. These data show that z is independent of material properties. Further studies verified that this parameter is also independent of absorbed intensity.

Thus, it is proposed that, for slabs of thickness greater than the critical thickness (Eq 3), one may with confidence predict front surface melting times via equations 2 or 4. Further, it is suggested that τ_∞ may be used as an upper bound on front surface melting times for slabs which do not meet this criterion.

It was pointed out above that, for "thin" slabs, equation 7 or 8 can be used to predict front surface melting times. In the course of this study, it was found that "thin slab" could also be defined in terms of the critical thickness. With this definition, it will be shown that the range of applicability of equation 7 or 8 can be established.

III. Definition of Thin Slabs

Using equations 5 and 7, it is easy to show that the front surface melting time for a slab is given by

$$\tau = \tau_{s1} + t' \tag{11}$$

where $t' = \frac{2 \ell^2}{\kappa \pi^2} \sum_{m=1}^{\infty} \frac{e^{\left(\frac{-m^2 \kappa \pi^2 \tau}{\ell^2} \right)}}{m^2}$ \hfill (12)

For thin slabs the series converges extremely rapidly, and t' may be adequately approximated by the first term. Thus,

$$t' \approx \frac{2\ell^2}{\kappa \pi^2} \; e^{\frac{-\kappa \pi^2 \tau}{\ell^2}} \tag{13}$$

A thin slab, for our purpose, amy be defined as one thin enough such that the series contribution to the surface thermal response at melting is negligible. This enables one to use the very simple equation 7 to predict front surface melting times and requires

$$t' \leq f \tau_{s1} \tag{14}$$

where f is some small fraction which we arbitrarily choose to be 0.01. Since τ_{s1} is a lower bound for τ, equation 13 is satisfied if

$$\frac{2\ell^2}{\kappa \pi^2} \; e^{\frac{-\kappa \pi^2 \tau_{s1}}{\ell^2}} \leq .01 \; \tau_{s1} \tag{15}$$

Using the expression for τ_{s1} given previously (Eq 8), equation 15 may be rewritten as :

$$\frac{2}{\pi^2} \left(\frac{1}{2.2} \frac{\ell_{crit}}{\ell} - \frac{1}{3} \right) e^{-\pi^2 \left(\frac{1}{2.2} \frac{\ell_{crit}}{\ell} - \frac{1}{3} \right)} \leq .01 \tag{16}$$

It is easily shown that equation 16 is satisfied when

$$\ell \leq .62 \; \ell_{crit} \tag{17}$$

Thus, it is proposed that, for slabs of thickness less than about three-fifths of a critical thickness, equation 7 or 8 may be used to predict front surface melting times (i.e., $\tau \approx \tau_{s1}$). Further, since the series contribution is neglected in equation 7, τ_{s1} may be used as a lower bound on front surface melting times for slabs of intermediate thicknesses ($.62 \; \ell_{crit} < \ell < \ell_{crit}$).

IV. Conclusion

This paper defines a critical thickness for a slab subjected to a constant flux of laser radiation. This critical thickness can be used in predicting front surface

melting time bounds for slabs of intermediate thicknesses. Table 2 summarizes the results of this study in terms of the critical thickness defined by equation 3.

Acknowledgements

The author gratefully acknowledges the many valuable discussions he had with Professor Peter J. Torvik of the Mechanics Department at the Air Force Institute of Technology. It was he who first suggested that the type of analysis presented in this paper could and should be done. Further, it was his inspiring and interesting lectures which first kindled the author's interest in laser induced melting.

Symbols

k	-	thermal conductivity
κ	-	thermal diffusivity
T_o	-	initial temperature
T_{surf}	-	front surface temperature
ΔT_m	-	melting temperature - initial temperature
I	-	incident intensity
α	-	absorptivity
t	-	time
τ	-	melting time
τ_∞	-	time required to melt front surface of a half-space
τ_{sl}	-	time required to melt front surface of thin slab
ℓ_{crit}	-	slab critical thickness
ℓ	-	slab thickness

References

1. Carslaw, H. S. and Jaeger, J. C. Conduction of Heat In Solids, Oxford University Press, 1959.

Table 1

CRITICAL THICKNESS VS Z FOR VARIOUS METALS

Metal	k J/cm-sec-k	ΔT_m^* k	ℓ_{crit}^{**}	z
Aluminum	1.84	611.	0.51	2.27
Magnesium	0.96	605.	0.26	2.22
Titanium	0.145	1600.	0.11	2.38
Stainless-Steel	0.240	1400.	0.16	2.38
Lead	0.320	300.	0.04	2.08
Copper	3.91	1050.	1.50	1.82
Nickel	0.67	1428.	0.46	2.38
Cadmium	0.944	294.	0.12	2.17
Silver	4.18	935.	1.50	1.92
				$\bar{z} = 2.18 \pm .06$

$^*T_o = 300^\circ$ k

$^{**}\alpha I = 5 \times 10^3$ w/cm^2

Table 2

PREDICTION OF FRONT SURFACE MELTING TIMES

IF	THEN	REF
$\ell > \ell_{crit}$	$\tau = \tau_\infty = \frac{\pi}{4\kappa(2.2)^2}\ell^2_{crit}$	EQ 4
$\ell < .62\,\ell_{crit}$	$\tau = \tau_{sl} = \frac{\ell\,\ell_{crit}}{2.2\kappa} - \frac{\ell^2}{3\kappa}$	EQ 8
$.62\,\ell_{crit} < \ell < \ell_{crit}$	$\tau_{sl} < \tau < \tau_\infty$	
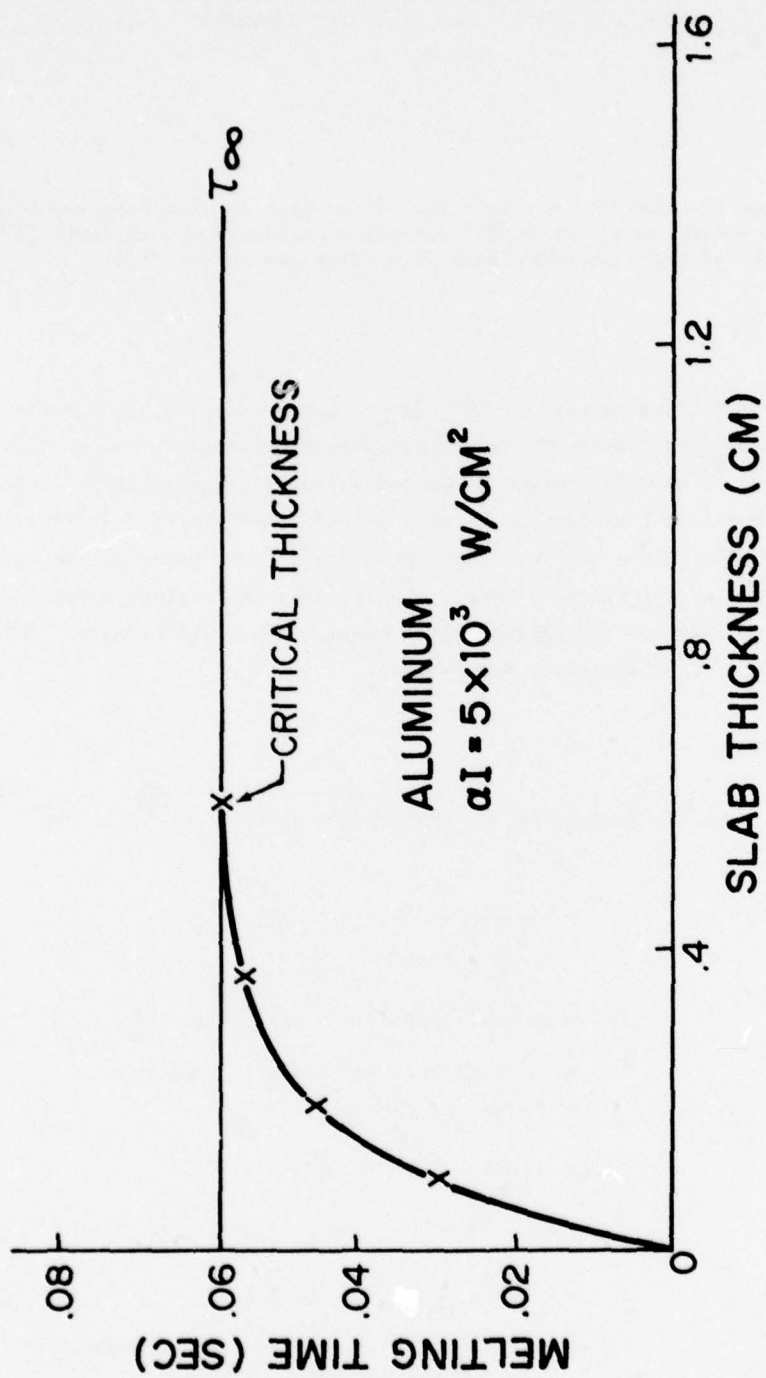
Figure 1. τ_∞ vs Time Required to Melt Front Surface of Slab

99

THE THEORETICAL BASIS AND EXPERIMENTAL APPLICATION
OF THE ANALOGY BETWEEN MASS AND HEAT TRANSFER

S. E. Icardi[*]

Abstract

This paper outlines the theoretical basis for the analogy between mass and heat transfer. It discusses an experimental method for estimating temperatures in flows by relating them to the measurement of mass concentrations of a trace gas in the flow.

I. Introduction

Due to concern over the impingement of hot exhaust gases from the gas dynamic laser on the fuselage and control surfaces of the Airborne Laser Laboratory, an experimental technique was developed to map the exhaust plume and estimate its temperature. The experiments involved modeling the flow in the wind tunnel, introducing a trace gas into a cold jet, and then, measuring the mass concentrations of this trace gas at various locations on the surface of the aircraft model. By applying the analogy between mass and heat transfer an estimate of the exhaust plume temperature could be made. This paper outlines the theoretical basis for these experiments.

II. Definition of Terms

$$\text{Lewis Number} = Le_j = \frac{Pr}{Sc_j} = \frac{\gamma_j}{\Gamma} = \frac{D_j}{\alpha} \tag{1}$$

where

μ = dynamic viscosity coefficient

Pr = Prandtl Number = $\frac{\mu}{\Gamma}$

Γ = thermal diffusion coefficient = $\frac{c}{k}$

c = specific heat at constant pressure

k = thermal conductivity

Sc_j = Schmidt Number = $\frac{\mu}{\gamma_j}$

γ_j = mass diffusion coefficient = ρD_j

ρ = density, mass unit volume

D_j = mass diffusion coefficient for component j in a multi-component mixture

α = molecular thermal diffusivity = $k/\rho c$

---

[*]Major, USAF, Instructor of Aeronautics, DFAN

III. Development of the Analogy

We will develop an analogy between heat and mass transfer using a technique similar to Reynold's analogy for heat and momentum transfer.

First, it is well known that for an arbitrary surface in laminar flow, the heat flux per unit area through the surface is:

$$q = -k \frac{dT}{dy} \quad \text{(ref. 1, pg 18)} \tag{2}$$

k = thermal conductivity

T = temperature

y = distance perpendicular to surface

and the mass "flow" rate per unit area through the surface is,

$$\dot{m}_j = -\rho D_u \frac{dw_j}{dy} \quad \text{(Ref. 1, pg 290)} \tag{3}$$

where ρD_j and y have been previously defined and $w_j = \frac{n_j M_j}{nM}$ = mass fraction

n = number of moles

M = molecular weight

Dividing heat flux by mass "flow", we have the following ratio for laminar flow:

$$\frac{q}{\dot{m}j} = \frac{k}{\rho D j} \frac{dT}{dwj} \tag{4}$$

Following the Reynold's analogy, the same type of relations should exist for turbulent flow.
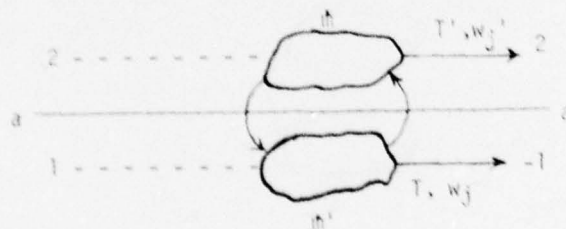
Consider the simple model in the figure above. A fluid mass m moves from plane 1-1 to 2-2 where its mass fraction and temperature become w_j' and T'. Continuity requires an equal mass m' to move from 2-2 to 1-1. The fluid that flows upward carries an amount

101

of heat equal to mcT and fluid flowing downward carries an amount m' cT' if $> T'$ since m = m' the heat flux per unit area through aa is:

$$q = \frac{mc}{A} \frac{(T-T')}{\Delta t} \tag{5}$$

The turbulent exchange causes a mass flow rate per unit area of one component of the mixture

$$\dot{m}_j = \frac{m}{A} \frac{(w_j - w_j')}{\Delta t} \tag{6}$$

Dividing heat flux by mass flow rate we have the following for turbulent flow

$$\frac{q}{\dot{m}_j} = c \frac{dT}{dw_j} \tag{7}$$

For the analogy to hold between laminar and turbulent flows then

$$c \cong \frac{k}{\rho D_j} \tag{8}$$

or,

$$\frac{c \rho D_j}{k} = \frac{D_j}{\alpha} \quad Le_j \equiv 1 \tag{9}$$

We are now able to relate the mass fraction difference to the temperature difference in a flow. If the Lewis number is one, we have seen above that the ratio of heat flux to mass flux at any particular point in the flow is the same regardless of the type of flow (laminar or turbulent). It follows that the relationship between temperature and mass concentrations at any particular point in the free stream and any two other locations in the flow are also the same.

$$\frac{q}{\dot{m}_j} = c \frac{T_1 - T_\infty}{w_1 - w_\infty} = c \frac{T_2 - T_\infty}{w_2 - w_\infty} \tag{10}$$

or,

$$\frac{T_1 - T_\infty}{w_1 - w_\infty} = \frac{T_2 - T_\infty}{w_2 - w_\infty} \tag{11}$$

adjusting this equation,

$$\frac{T_1 - T_\infty}{T_2 - T_\infty} = \frac{w_1 - w_\infty}{w_2 - w_\infty} \tag{12}$$

102

Experimentally, if we desire to estimate the temperature in a flow (knowing the temperature in the free stream and at one other location in the flow), we can do so by modeling the flow and introducing a trace gas into the flow. Measuring the mass fraction of the trace gas at these locations and using the following equation, we can estimate the temperature :

$$T_1 = \frac{w_1}{w_2} (T_2 - T_\infty) + T_\infty \tag{13}$$

This equation of course assumes that the mass fraction of the trace gas in the free stream is zero ($\omega_\infty = 0$)

IV. Conclusion

Experiments verifying this technique have been performed by a number of researchers and are sighted in Reference 2 pg. 472. This technique was used to estimate temperatures in hot exhaust gases of the Airborne Laser Laboratory Laser Exhaust Plume. The experiments were run in the subsonic wind tunnel at the U.S. Air Force Academy. The results of these experiments are reported in Reference 3.

References

1. Eckert, E.R.G.; Introduction to Heat and Mass Transfer; translated by Joseph F. Gross, McGraw Hill, New York, 1963.

2. Eckert, E.R.G. and R. M. Drake; Heat and Mass Transfer; McGraw Hill, New York, 1959.

3. Icardi, S. E.; "All Exhaust Flow Experiments (Duct Backpressure and Plume Impingement)" Laser Digest, Fall 1974, Air Force Weapons Laboratory, Kirtland AFB, NM, 1974.

SECTION IV

INSTRUMENTATION

AND

HARDWARE

IMPROVED INSTRUMENTATION OF A

CLASSROOM WIND TUNNEL

G. Douglas Evans[*]

Abstract

This paper describes an alternative electronic lift and drag measuring system for the Department of Aeronautics 12" wind tunnels. An analysis of the problem areas of the present mechanical measuring system is given. An alternate digital electronic system is described along with the test results obtained in testing this alternative. Recommendations of future changes and implementation of this new system are made.

I. Introduction

Commercially available wind tunnels, with a 12" diameter circular test section, are used by the Department of Aeronautics at the United States Air Force Academy for demonstrations and experiments in introductory Aeronautical Engineering courses. They are mechanically simple, and fairly inexpensive, but are capable of producing data for quantitative analyses.

The wind tunnels are constructed with a mechanical pointer and scale system to display lift and drag forces acting on the test model. Usually, however, the pointers fluctuate excessively, which makes data collection difficult and uncertain. This paper reports on the feasibility of improving the present mechanical measurement system used in classroom wind tunnels by installation of a new electronic digital measurement system.

The design of the improved alternative presented here was greatly influenced by the criteria that the system be inexpensive and easily installed. Additionally all electronic circuitry required had to be constructed by an undergraduate student using readily available parts.

II. Wind Tunnel Construction

Figure 1 shows the construction of the classroom wind tunnels used at the USAF Academy. The wind tunnels have a 12 inch diameter test section. A model is placed on a test stand which is connected to mechanical pointers that indicate the amounts of lift and drag. Air enters the tunnel through the honeycomb inlet. The honeycomb forms a series of small tubes through which the air is drawn, straightening and smoothing the airflow. The wall of the test section is made of clear Plexiglass, enabling the model to be viewed during testing. Angle of attack (α) can be adjusted by a thumb-screw on

---

[*] C1C, USAFA, Cadet United States Air Force Academy, Graduated Jun 77
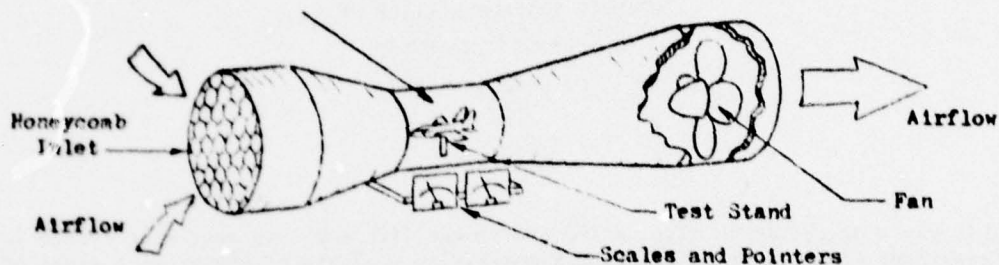
the test stand through the range $-20°$ to $+20°$.

Figure 1. Wind Tunnel Construction

Zeroing thumb-screws are provided to set the pointers to zero under no-wind conditions. Air is drawn through the tunnel by a four-bladed electric fan mounted at the wind tunnel exit.

III. Mechanical Force-Measuring System

A. Lift and Drag vs Angle of Attack

For low angles-of-attack, C_L changes nearly linearly with angle of attack, while the C_D curve is parabolic. Drag is always positive, whether α is positive or negative, while lift can take on positive or negative values. Figure 2 shows an ideal plot of lift and drag coefficients vs α.
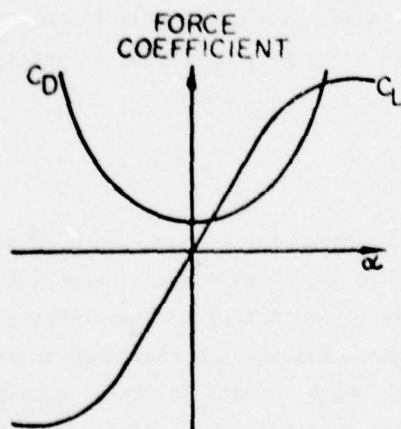
Figure 2. Typical Lift and Drag Coefficients vs α

106

B. Pointer Construction

Figure 3 shows the present method of measuring and indicating lift and drag forces with the classroom wind tunnels. Lift and drag are measured using the same method (only the lift-measuring system is shown). Lift forces the model, test stand, and steel spring upward, pulling a string in the direction indicated. The string pulls on the pointer, which is balanced by a counterweight and a small spring. The small spring is omitted from Figure 3 for simplicity. As lift increases, the string is pulled and the pointer moves toward the right, indicating an increase in force.
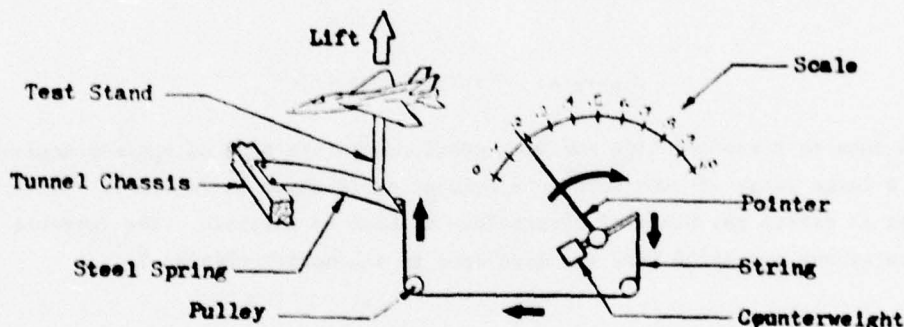
Figure 3. Mechanical Force Measuring System

As lift decreases, tension in the string is relaxed, and the counterweight and steel spring force the pointer back to the left, indicating a decrease in force. The mechanical system is not capable of indicating downward-acting lift.

C. Cause of Pointer Fluctuation

The steel spring is not very stiff, and the pointer assembly is of low-mass construction. Turbulent flow inside the wind tunnel causes the model to vibrate considerably. The fan causes the entire wind tunnel to vibrate. Together, these two effects cause the pointer to fluctuate erratically, making accurate readings very difficult.

D. Resultant Data and Uncertainty

Most of the test models used in this particular wind tunnel (1/72 scale models) produce a maximum lifting force of 0.70 pound. Some larger models (1/48 scale) produce up to one pound of lift. Typical values of lift change by only 0.02 pound when α is changed by two degrees. Corresponding changes in values of drag are only about 0.01 pound. However, the pointers fluctuate up to 0.06 pound for both lift and drag. This fluctuation covers a greater range than the distance between two data points. A 0.06

107

pound fluctuation for a model producing 0.70 pound of lift equates to an uncertainty of up to 9%. This same fluctuation for a maximum drag of 0.22 pound (typical for a 1/72 scale model) equates to an uncertainty of up to 37%. Figure 4 shows a typical range of pointer fluctuation against a calibrated scale.
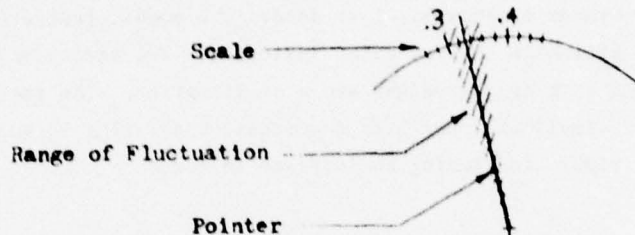

Figure 4. Pointer Fluctuation

When data is taken and lift and drag coefficients are plotted against angle-of-attack, a large range of uncertainty is evident as is shown in Figure 5. It is desirable then to reduce the range of uncertainty as much as possible. The improved instrumentation system presented here was developed to accomplish this goal.
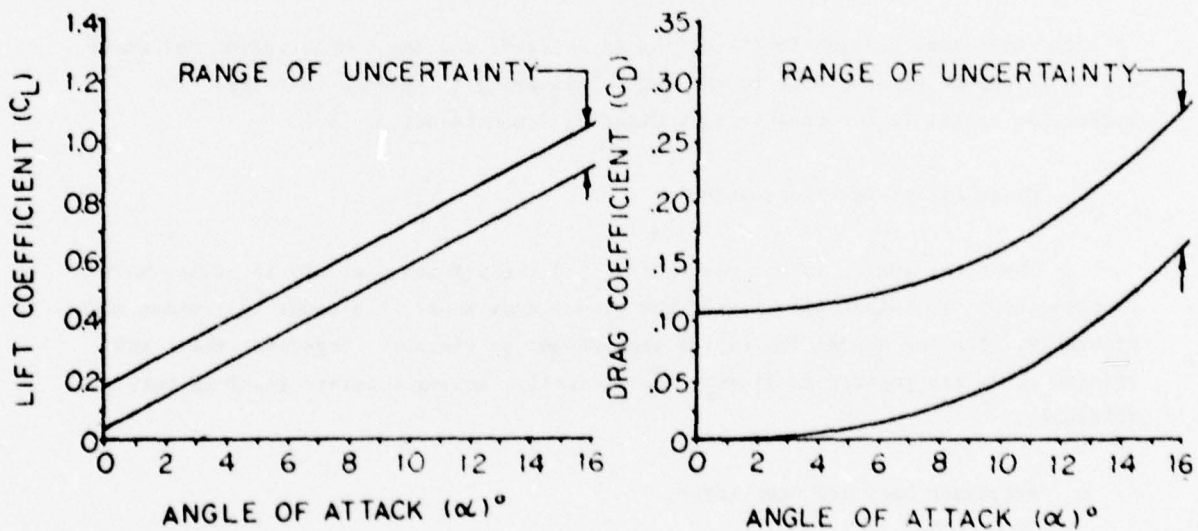
Figure 5. Mechanical Data Uncertainty

IV. Digital Measurement System

The use of electronic circuitry to solve the pointer fluctuation problem was chosen because of its simplicity and versatility. Voltage fluctuations caused by the wind tunnel vibrations can easily be smoothed into steady values with filters, and electronic signals can be easily controlled and measured.

A. Force Sensing

Strain guages were used to sense lift and drag forces. These devices measure the amount of bending that the steel springs experience. An enlarged strain gauge is shown in Figure 6. The foil pattern has a nominal resistance of 120 ohms. However, when the strain gauge is stretched, its resistance will increase by a slight amount.
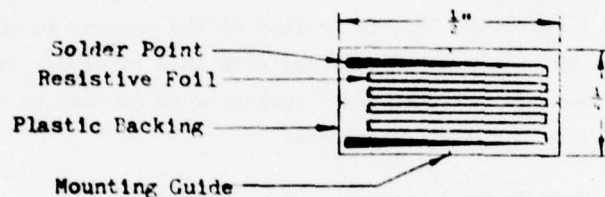
Figure 6.   Strain Gauge

Conversely, the resistance will decrease slightly if the strain gauge is compressed. The change in resistance is proportional to the amount of stretch or compression the strain gauge experiences. The strain gauges were mounted on the surfaces of the steel springs as shown in Figure 7.
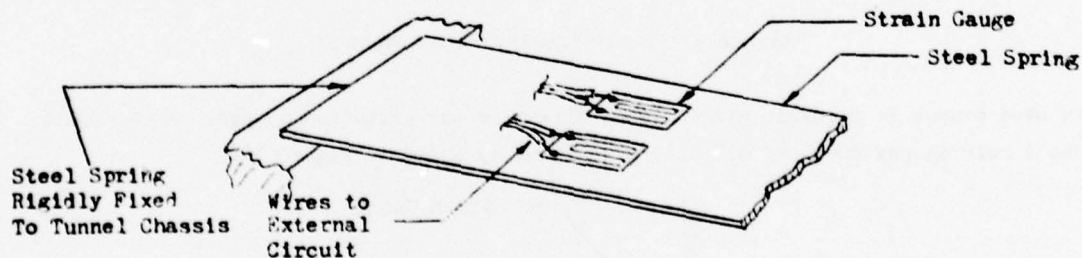
Figure 7.   Strain Gauge Mounting

In this configuration, as a spring is deflected downward, the strain gauges would be stretched, and their resistances increased. On the other hand, if the spring were deflected upward, the strain gauges would be compressed, and their resistances decreased. Figure 8 illustrates the stretching and compressing of the strain gauges upon bending of the springs.
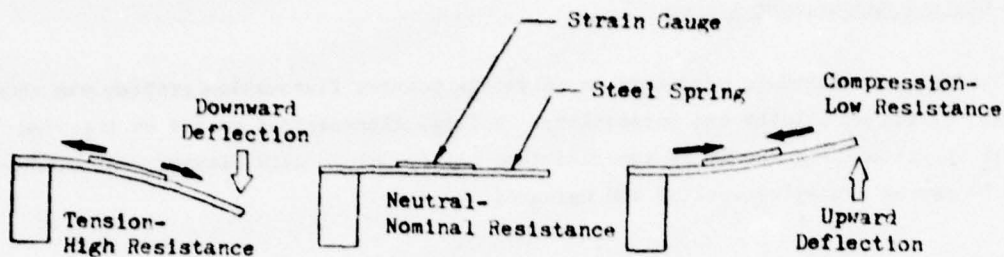
109

Figure 8.   Strain Gauge Stretch and Compression

B.   Strain Gauge Mounting Problems

Strain gauges must be precisely mounted to give proper indications of spring deflection.   Normally, a reference line is scribed on the surface to which the strain gauge is to be mounted, and the gauge is aligned with this reference line, as shown in Figure 9.   However, because the test stand springs were located in hard-to-reach locations, a reference line could not be scribed.
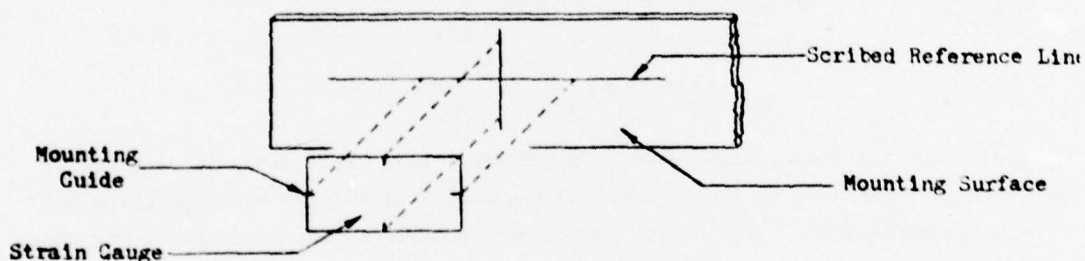

Figure 9.   Ideal Strain Gauge Mounting

As near proper as possible strain gauge alignment was estimated by eye.   As a result, the strain gauges ended up slightly misaligned as shown in Figure 10.
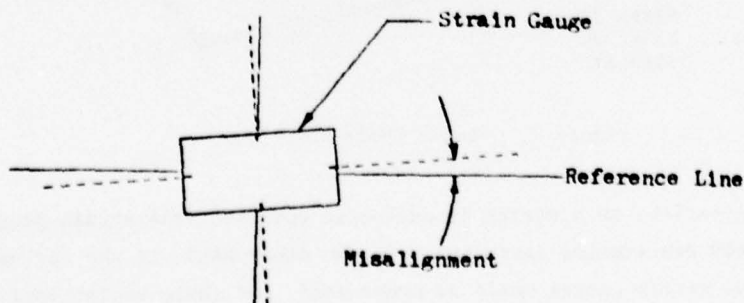
Figure 10.   Strain Gauge Misalignment

110

To properly mount the strain gauges in any future endeavors, the spring unit should be removed from the wind tunnel. If this were done the springs could then be placed on a suitable workbench where proper mounting procedures could be followed. This was not done in this first modification because of the time involved and the difficulty of disassembling the wind tunnels.

C. Conversion of Force to Electrical Signal

Through the use of these strain gauges, lift and drag forces on the model produced an electrical resistance in an electrical circuit. The strain gauge resistances changed linearly with the amount of force acting on the model. The gauges were arranged in a Wheatstone Bridge circuit as shown in Figure 11. A change in aerodynamic force caused a proportional change in voltage. The potentiometer was adjusted to provide zero output voltage under no-force conditions.
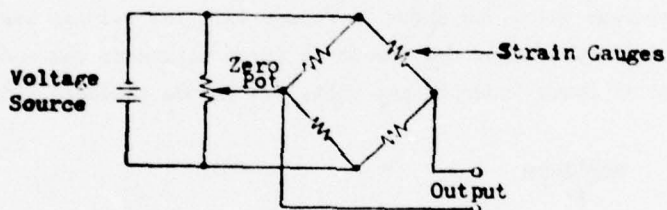
Figure 11. Strain Gauge Bridge Circuit

D. Temperature Compensation

Only two strain gauges were mounted to each steel spring in the wind tunnel. The other two strain gauges in each bridge circuit were dummy gauges, mounted on a strip of aluminum and placed in close proximity to the active gauges. As a result, all four gauges were always subjected to the same ambient temperatures.

(In many circuits using active and dummy strain gauges, the active gauges are remotely mounted, while the dummy gauges are mounted with other circuitry. The two types of gauges are then subjected to unlike temperatures, and they have different nominal resistances. As a result, the electrical characteristics of the circuit change as temperature changes. To avoid this problem, the dummy strain gauges were co-located with the active strain gauges.)

E. Electronic Filtering and Calibration

The strain gauge output signal with a 5 volt power supply was about 1 millivolt (mV) per pound of force acting on the model. However, the signal fluctuated as

111

the springs vibrated. The signal had to be filtered and amplified before the true
signal could be accurately measured. Figure 12 shows the voltage from the strain gauges
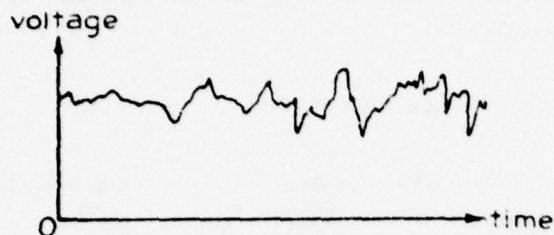with these random fluctuations over a period of time.

Figure 12. Unfiltered Strain Gauge Voltage

This signal could not be displayed as a fixed value. However, the fluctuations were
easily filtered with the proper electronic circuitry. The voltage then appeared smooth
and took on the average value, as shown in Figure 13. The voltage was also amplified
to a level which corresponded to the amount of force acting on the model, so that for
example, one pound of force produced one volt, 1.5 pounds produced 1.5 volts, etc.
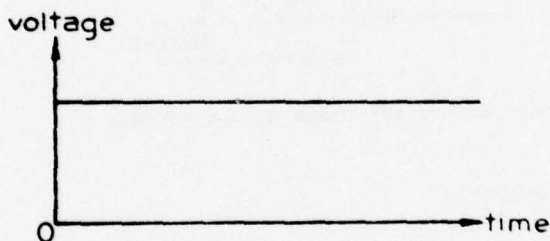
Figure 13. Filtered Strain Gauge Voltage

A low cost operational amplifier (op-amp) using a feedback resistor and a feedback
capacitor was used to accomplish the filtering and amplification. The op-amp circuit
is shown in Figure 14. Amplification, or gain, was adjusted by varying the value of
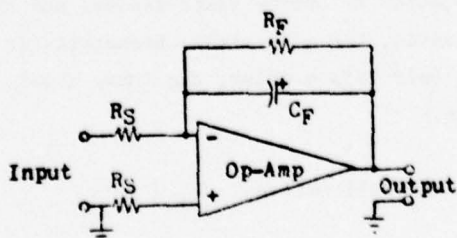feedback resistor R_F.

Figure 14. Op-Amp Circuit

112

Gain for the circuit in Figure 14 is given by the equation: Circuit gain = $\dfrac{R_F}{R_S}$. Filtering was accomplished by the parallel combination of R_F and C_F. The time constant formed by this circuit is the product of R_F (ohms) X C_F (farads) and is expressed in seconds. A larger time constant will allow the circuit to pass only lower frequencies. Therefore, it was desirable to have a very large time constant so that only direct current (DC) was passed. Consideration for values of R_F and C_F are discussed in Section III. J.

F. Digital Force Display

To read the voltage produced by the op-amp, a digital voltmeter (DVM) was used. If the amplifier is calibrated to produce one volt per pound of force, and there are 1.34 pounds of force acting on the model, the digital display would indicate *1.340*.

G. Lift Measure at Negative Angles-of-Attack

The mechanical pointers, as they come with the wind tunnels, are rigged so that they can only indicate lift in an upward direction, so the model can only be tested for lift at positive values of α. However, the test stand is adjustable from 20° nose-up to 20° nose-down. Fortunately, the digital measurement system produced a negative voltage which was proportional to lift acting in the downward direction, and the DVM used had the capability to indicate negative voltages; therefore, an added capability for negative lift measurements was achieved. For example, if the test model was oriented in the relative wind at $\alpha = -10^\circ$, giving rise to a 0.33 pound of force in the downward direction, the DVM would display *0.330-*.

H. Digital Measurement Uncertainty

The digital instrumentation circuitry was calibrated to produce 10 millivolts per pound of force. The amplification was kept low to reduce the cost of the circuitry; the DVM used, however, was precise when measuring low voltage signals. The DVM display fluctuated within a range of 0.010 pound. For example, a 0.43 pound of force would cause the DVM display to fluctuate from "0.425" to "0.435" over a period of time. This uncertainty is six times less than the 0.06 pound uncertainty experienced with the mechanical system. The digital system produced, therefore, 1/6 the data point scatter of the mechanical system. Figure 15 on the following page shows graphically how the digital system reduced data point scatter. Digital uncertainty at maximum values of lift and drag was under 1.5% for lift and under 5.0% for drag.
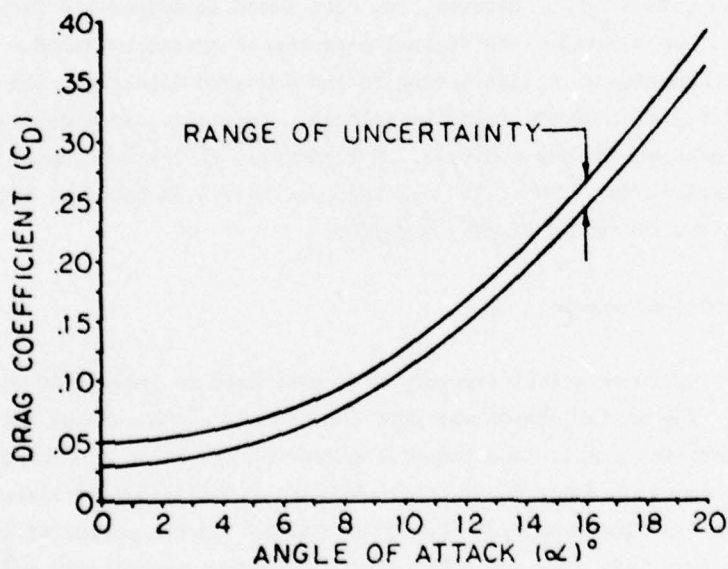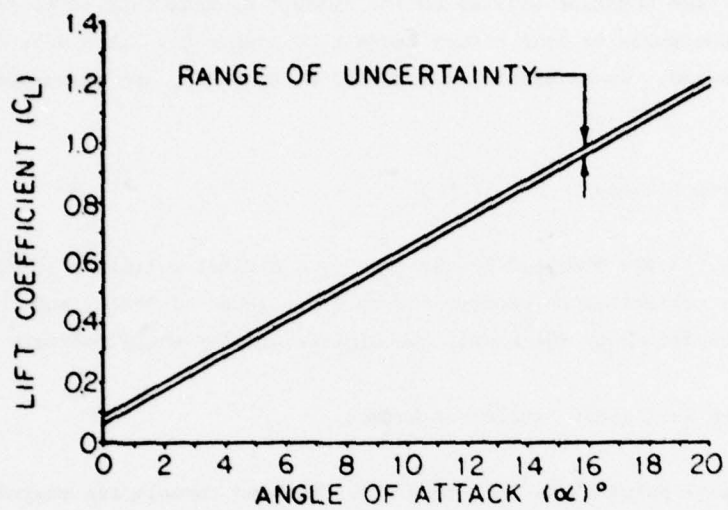
113

Figure 15. Digital Data Uncertainty

114

I. Digital Circuit Equipment Description

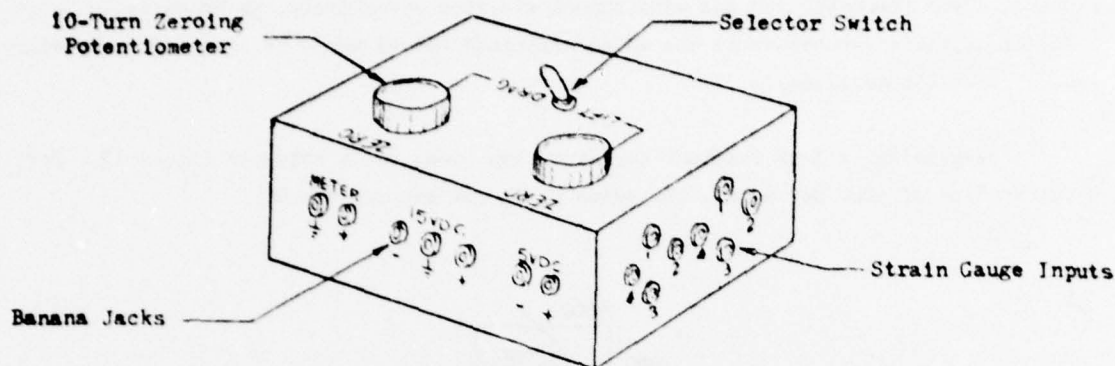The external features of the Filter/Amplifier are shown in Figure 16.

Figure 16. Filter/Amplifier

Refer to the Appendix A for the circuit schematic. Five volts were applied across the strain gauge bridge circuits. To zero under no-force conditions 5k Ω potentiometers were used to set the bridge circuit output voltages. Zeroing had to be accomplished because models of different weight deflected the steel springs by different amounts when they are mounted to the test stand. The potentiometers were 10-turn types to make zeroing easier, as this was a sensitive circuit.

The strain gauge bridge circuit acted as a variable voltage divider. As the active gauges were deflected, the bridge circuit output voltage changed. The selector switch selected lift or drag strain gauge voltages. This voltage was then applied to the op-amp inputs. The positive strain gauge signal was applied to the invert input, so the output was 180° out of phase with the input. For positive deflections, the lift gauges were in compression, and the drag gauges were in tension. For this reason, dummy and active strain gauge arrangements were opposite in the lift and drag circuits. The calibration resistors (500k Ω multiturn trim potentiometers) were selected by the selector switch in conjunction with the bridge circuit voltage selection. Varying the values of these resistors changed the gain of the amplifier. Therefore, amplification could be calibrated differently for lift and drag using only one op-amp. This kept parts costs to a minimum. The 1 μ F capacitor, in parallel with the 500k Ω resistors, formed an RC active filter with the op-amp. The DC Offset potentiometer was a multi-turn trim pot. It was adjusted so that the op-amp produced no output voltage when no input voltage was present.

J. Filtering vs Zeroing Problems

Theoretically, the digital system should be capable of filtering all of the strain gauge voltage fluctuations as shown in Figure 12. However, because the airspeed fluctuated and the model and the wind tunnel vibrated excessively, an excessively large feedback capcitor (excessive in the sense discussed below) would be needed to completely smooth these fluctuations.

Originally, a 5 μF feedback capacitor was used, as is shown in Figure 17. For a calibration of 10mV per pound, the value of R_F was set to 100k Ω.
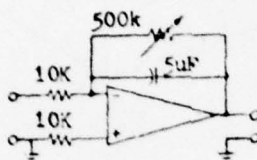

Figure 17. Feedback Circuit

The time constant was 100k Ω x 5 μF = 0.5 seconds. A typical time constant is shown in Figure 18. An impulse voltage at t = 0 would cause the output waveform shown.
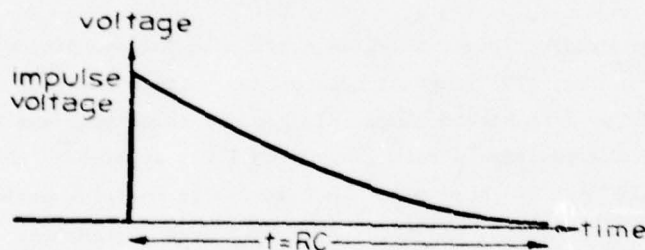

Figure 18. Time Constant

The time constant produces a lag in response time in the zeroing circuit. After the zeroing pots are stopped rotating, the output voltage would continue to rise or fall for the duration of the time constant. This time lag, coupled with the high sensitivity of the circuit, made zeroing a very difficult procedure.

To alleviate the situation, a tradeoff was made between filtering qualities and ease of zeroing. A 1 μF capacitor was substituted for the 5 μF capacitor. The resultant time constant was 100k Ω x 1 μF = 0.1. Zeroing was made easier because of

116

the smaller time lag. There was also very little difference in filtering quality between the two values of capacitors since most of the fluctuations were of shorter period than 0.1 second. (See Section V for an improved zeroing feature.)

V. Results

Figure 19 compares the uncertainty ranges of the mechanical pointers and digital display. The improved characteristics of the digital measuring system are quite evident. The test data showed that the digital measuring system did reduce the uncertainty error by a large amount (600% reduction in lift and as much as a 500% reduction in drag) resulting in a significantly improved data quality.

VI. Cost of Modification

The circuitry used in the modification was designed to be low cost. The price of all circuitry, excluding the DVM, was about $230. Because the circuit used very few components, it had low gain. Output was only about 7mV for a 1/72 scale model at maximum lift. To read this low voltage precisely, an expensive DVM (costing around $1400) needed to be used. The DVM used in this modification was used by the Department of Aeronautics for a variety of applications and therefore contained many features not required for this wind tunnel modification. The same digital accuracy can be maintained by further amplifying the strain gauge output voltage from our 10mV/lb to 1V/lb. This higher voltage could then be measured with a low cost DVM, available for about $150.

One drawback of the initial circuit was that the time constant changed when R_F was adjusted. This circuit was greatly improved by using only $3.00 worth of additional parts. The improved circuit is shown in Appendix B. During zeroing, the filter capacitor was cut out of the circuit. This resulted in no time lag during the zeroing operation, yet it permitted the capacitor to be large enough for improved filtering qualities. The gain of this circuit could be set to 1V/lb. or to 1V/Newton. This higher voltage could easily be read to the thousandths place by a low cost DVM.

Using the improved circuitry and a low cost DVM, the cost of a single modification would be $383. The classroom wind tunnels are currently available at a cost of about $2000. Therefore, the cost of the modification is only 19% of the total cost of a new wind tunnel.

VII. Conclusions

The classroom wind tunnels in their original configuration can only be used for basic aeronautical demonstrations with the mechanical measuring system. However, with the

117

improved accuracy of the digital measuring system described here, the wind tunnels could be used for more exact experimentation by undergraduate students.

The electronic circuitry used in the digital measurement system was inexpensive and readily available from electronic supply houses. A student could easily obtain the required parts and build a new measurement system in about one month.
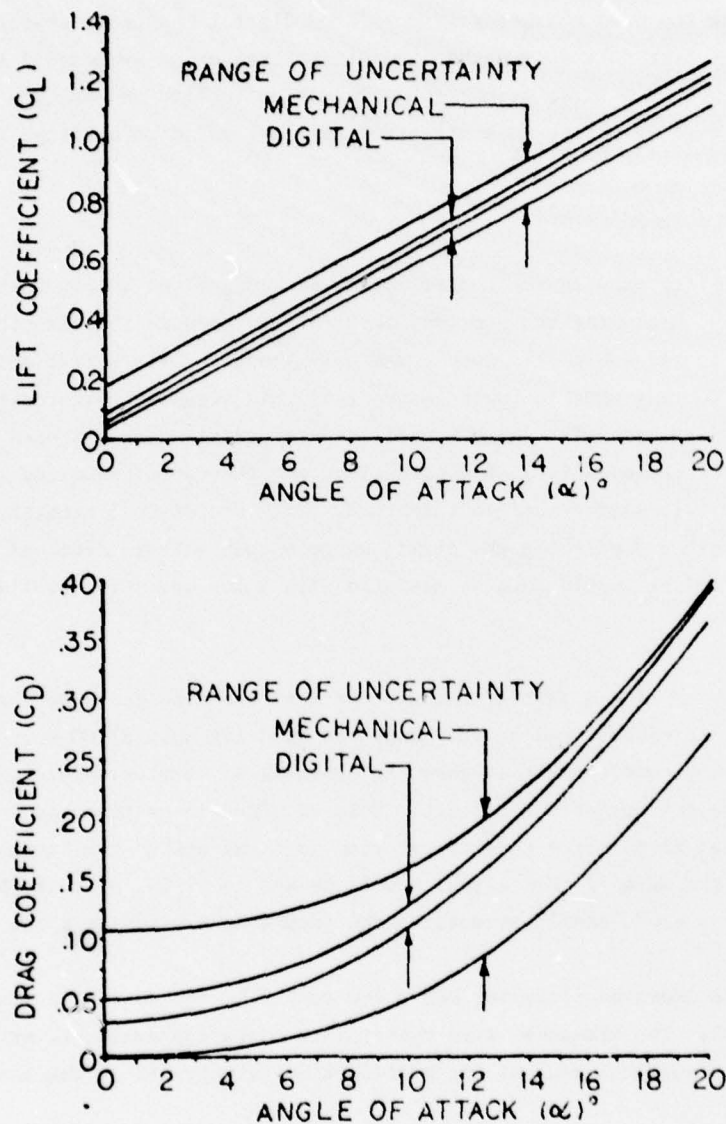

Figure 19. Direct Mechanical/Digital Data Uncertainty Comparison

VIII. <u>Recommendations</u>

The digital measurement system should be reconstructed using the improved circuitry provided in Appendix B. This improved circuit permits the use of a low cost DVM. If there are any future plans for using the 12" wind tunnels for precise experiments, I recommend that all wind tunnels committed for this purpose be modified to the Digital display system.

APPENDIX A

DIGITAL CIRCUIT SCHEMATIC

D-DUMMY STRAIN GAUGE
A-ACTIVE STRAIN GAUGE
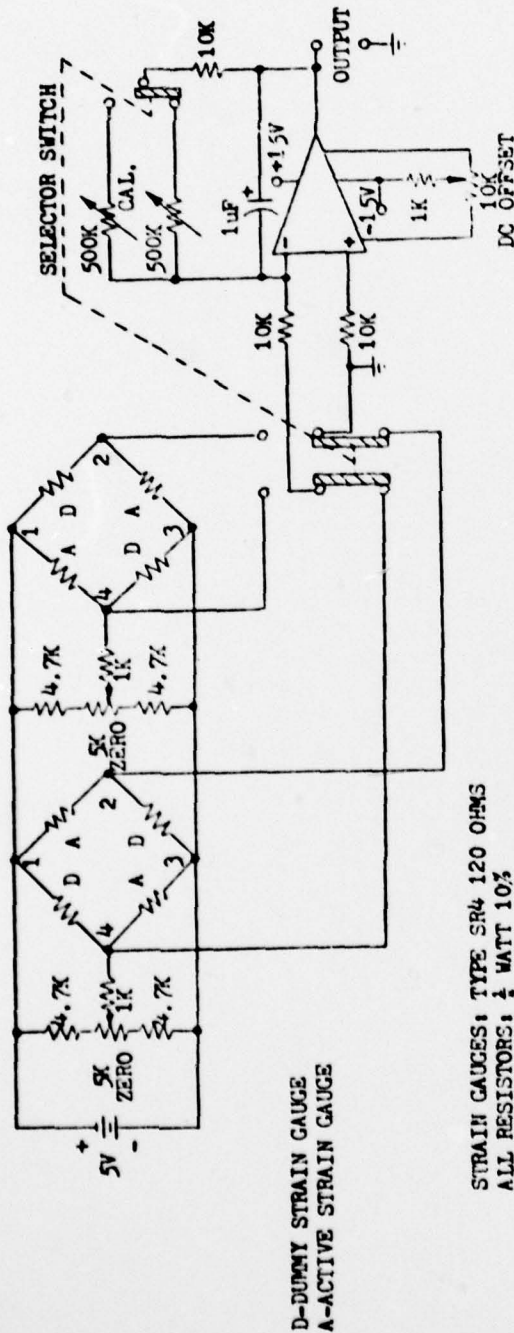
STRAIN GAUGES: TYPE SR4 120 OHMS
ALL RESISTORS: ¼ WATT 10%
POTENTIOMETERS: ZERO: 10-TURN PANEL MOUNT
                CAL., DC OFFSET: MULTITURN P.C. MOUNT

SELECTOR SWITCH: 3P2T TOGGLE
ALL GROUNDS ARE TO ±15V POWER SUPPLY
NOTE: DO NOT GROUND 5V POWER SUPPLY TO ±15V POWER SUPPLY.
      THIS WILL SHORT THE BRIDGE CIRCUITS.
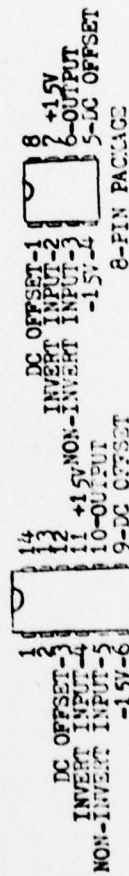
TYPE 741C INTEGRATED CIRCUIT
PIN CONFIGURATION

IMPROVED DIGITAL CIRCUIT SCHEMATIC

IC1, IC2: TYPE 741C
ALL RESISTORS: $\frac{1}{4}$ WATT 10%

CIRCUIT BOARD
(FOIL SIDE)
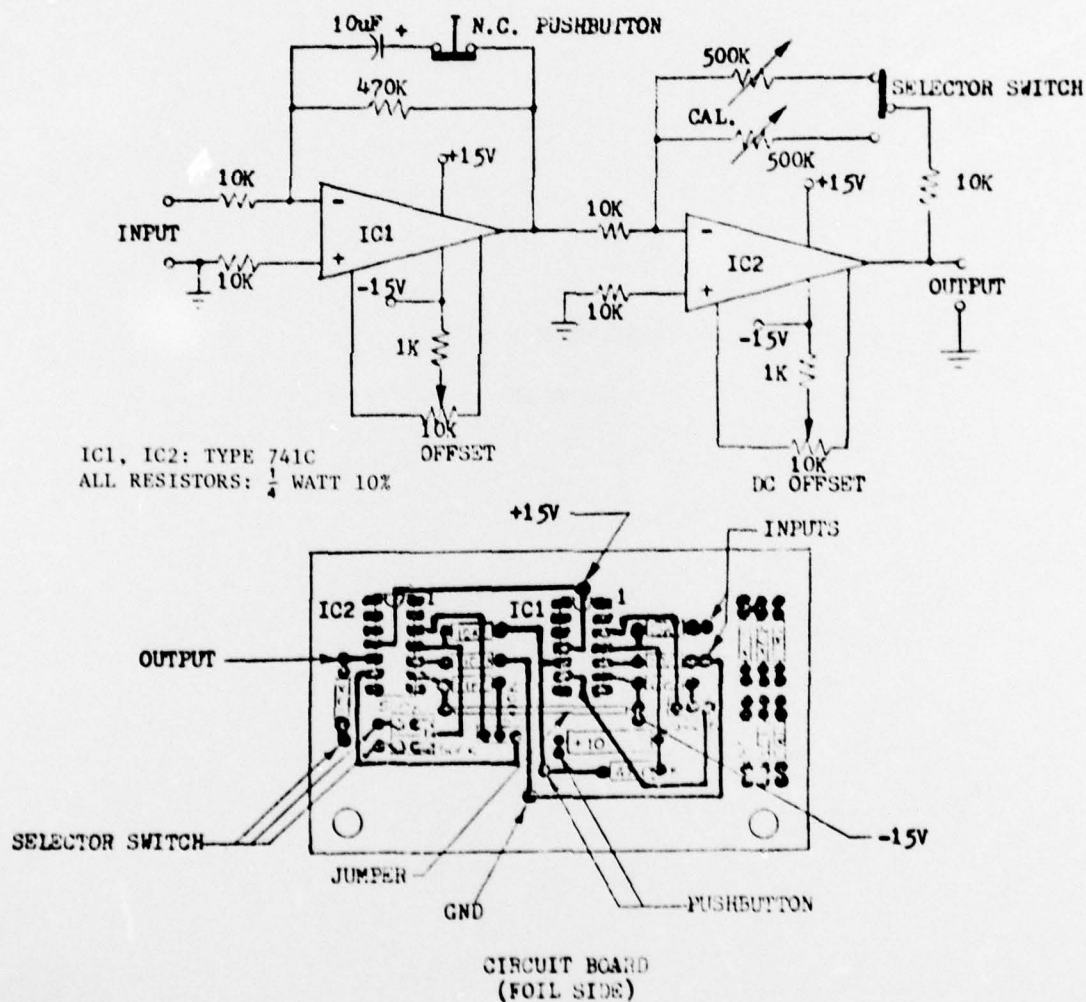
SECTION V

ABSTRACTS

A COMPUTERIZED UNDERGRADUATE AIRCRAFT DESIGN COURSE
G. T. Matsuyama[*]

ABSTRACT

The integration of computer programs with an undergraduate aircraft design course is described with emphasis placed on the computer program known as AERO464RPV, which was written specifically for the course. This approach to design education has proven highly effective at the Air Force Academy during the period 1975 through 1977.

The course is structured to require periodic tasks of students throughout the semester to include (1) an initial weight estimation, (2) wing, fuselage, and tail design, and configuration layout, (3) lift, zero-lift drag, and drag-due-to-lift determination, (4) a refined fuel and empty weight analysis, and, finally, (5) a final report. Manual calculations are required for all tasks, and extensive familiarity with the design process is emphasized. Computer programs may be used only after initial manual calculations have been completed.

Two computer programs are used. The program identified as AERO464RPV was written specifically for the design course and employs course methods. This program is discussed to some extent in the paper. It requires basic vehicle geometry, aerodynamic coefficients, and a mission profile to be entered as inputs. Output is controlled by an input variable, and progresses in complexity as further information becomes available. The program computes weight/fuel fractions and "flies" the vehicle while attempting to achieve convergence with a historical empty weight. Early in the semester, initial geometric data such as wing characteristics and fuselage volume are available as output. Centers of gravity follow after component locations are established. Fuel tank sizing is automatic and a refined weight analysis is possible. Finally, fuel sequencing, static margins, trim drags, and a time history of flight are all obtainable by the end of the semester when sufficient vehicle data is available. This program's value lies in the fact that (1) only course methods are employed, (2) its input and output structure allows

---

[*]Major, USAF, Assistant Professor of Aeronautics, DFAN

the student to develop an initial data deck and add to it as further information is gained, (3) rapid evaluation of design changes is possible, (4) previous output may be re-generated merely by changing one input variable and without having to disassemble or rearrange the data deck, and (4) its structure allows for modification to accomodate any fighter-type vehicle. The baseline vehicle is an advanced RPV using a J-85 turbojet engine. To date, the program has been successfully modified and used to investigate a manned, fighter/trainer/ECM vehicle, and now includes a TFE 731-2 turbofan.

The second program, known as DIGITAL DATCOM, predicts aerodynamic coefficients and stability derivatives for the wing, tails, and fuselage as well as for the integrated configuration. Its unique input and output capability allows the student to input either one component (e.g. wing) and receive all pertinent information or to input the entire configuration and still receive individual component results together with the total configuration results. The coefficients obtained here are used as inputs to AERO464RPV. It should be noted at this time that DIGITAL DATCOM is a 1973 version which was heavily modified for Academy use. A new and expanded version identified as AFFDL-TR-76-45 and documented in 3 volumes was recently published by the Flight Dynamics Laboratory, Wright-Patterson AFB, Ohio.

To date, AERO464RPV has:

1. Successfully been employed over 3 semesters to assist students in accomplishing rapid design changes, and to evaluate the effects of these changes.

2. Demonstrated a clear advantage over other computerized methods due to the fact that only course methods are programmed, thus allowing immediate duplication of manually acquired data and instilling confidence in the student.

3. Enhanced the student's learning process by providing adequate data upon which to base undergraduate design decisions.

4. Added to the student's appreciation of the interrelationships between configuration, center of gravity, and aerodynamic characteristics due to the building-up process of the data bank as well as the extensive capabilities of the program.

124

5. Given the student an appreciation of the usefulness of the computer as a tool.

6. Demonstrated an adaptability for conversion as evidenced by its successful modification and use where a multi-role, manned fighter was investigated.

In light of the above, it is concluded that the use of a baseline computer program employing only course methods offers significant advantages to an undergraduate aircraft design course.

125

A TECHNIQUE FOR VORTICITY MEASUREMENT IN UNSTEADY FLOW

John E. Keesee[*]

Michael S. Francis[**]

James D. Lang[***]

ABSTRACT

A technique is described for determining spatial vorticity distributions in non-stationary fluid flows exhibiting a periodic, time-varying mean velocity field. Although vorticity is one of the most significant physical variables in many complex flows involving shear, it is a quantity which has been difficult to measure accurately. The method discussed in the present paper is one based on a simple premise which involves no assumptions on the dynamic nature of the flow and is therefore inherently accurate.

The basis for the method lies in the generalized definition of circulation as follows:

$$\Gamma(t) = \oint_C \vec{U}(\vec{x},t) \cdot d\vec{\ell}(\vec{x}) \tag{1}$$

where

Γ is the circulation about a closed spatial contour, c.

$\vec{U} \cdot d\vec{\ell}$ is the inner product of the velocity vector with the local path vector on the contour, c.

Equation (1) can be related to the vorticity variable through Stoke's theorem:

$$\oint_C \vec{U}(\vec{x},t) \cdot d\vec{\ell}(\vec{x}) = \iint_A \vec{\xi}(\vec{x},t) \cdot d\vec{A}(\vec{x}) \tag{2}$$

where

$\vec{\xi} = \vec{\xi}(x,y,z,t)$ is the vorticity vector.

A is a capping surface of the contour, c.

If A is taken to be the planar area enclosed by the contour in the xy-plane, for example, one extracts an expression for the spatially averaged ($< >$) z-component of vorticity:

$$< \xi_z(t) > = \frac{1}{A} \oint_C \vec{U}(\vec{x},t) \cdot d\vec{\ell}(\vec{x}) \tag{3}$$

[*] Captain, USAF, Research Associate, FJSRL

[**] Captain, USAF, Chief, Mechanics Division, FJSRL

[***] Major, USAF, Associate Professor of Aeronautics, DFAN

If a number of contours are arranged in a relatively fine mesh configuration, the distribution of vorticity in the enclosed region can be inferred. The spatially averaged z-component of vorticity for the "i"-th element of the mesh can then be determined from the following relation:

$$< \xi_z(t)_i > = \frac{1}{A_i} \oint_{c_i} \vec{U}(\vec{x},t) \cdot d\vec{\ell}(\vec{x}) \tag{4}$$

Similar expressions for the other vorticity components can be obtained by orthogonal rotations of the integration plane.

The procedure involved in evaluating these integrals requires the accurate measurement of selective velocity components at various spatial locations. This can be accomplished with a number of velocity measurement devices currently available. A sufficient number of sampling locations must be employed along each contour segment for an accurate determination of the integral.

A primary consideration for most real flows of interest is the extraction of a time-varying mean value of the fluid velocity from a data signal which also contains random fluctuations caused by turbulence and noise. In this case, a velocity component, or other flow variable q, can be written in the form

$$q(t) = \overline{q(t)} + q'(t) \tag{5}$$

where $\bar{q}$ denotes the time-varying mean value of the variable q, and q' is a random fluctuation characterized by the relation

$$\overline{q'} = 0 \tag{6}$$

The time-varying mean value of the variable must then be extracted by a phase-locked ensemble averaging technique. In the present application, equation (4) can be rewritten

$$< \overline{\xi_z(t)_i} > = \frac{1}{A_i} \oint_{c_i} \overline{\vec{U}(\vec{x},t)} \cdot d\vec{\ell}(\vec{x}) \tag{7}$$

where the overbar represents an ensemble averaged time-varying value of the variable.

An evaluation of the entire time-varying, spatial vorticity distribution involves the determination of the ensemble average of velocity at each measurement location. A sample of an instantaneous cycle of data is constrasted with its corresponding ensemble average in Figure 1. Each averaged data set may require from a few to several hundred data "records" depending on the level of turbulence at that location. The

127

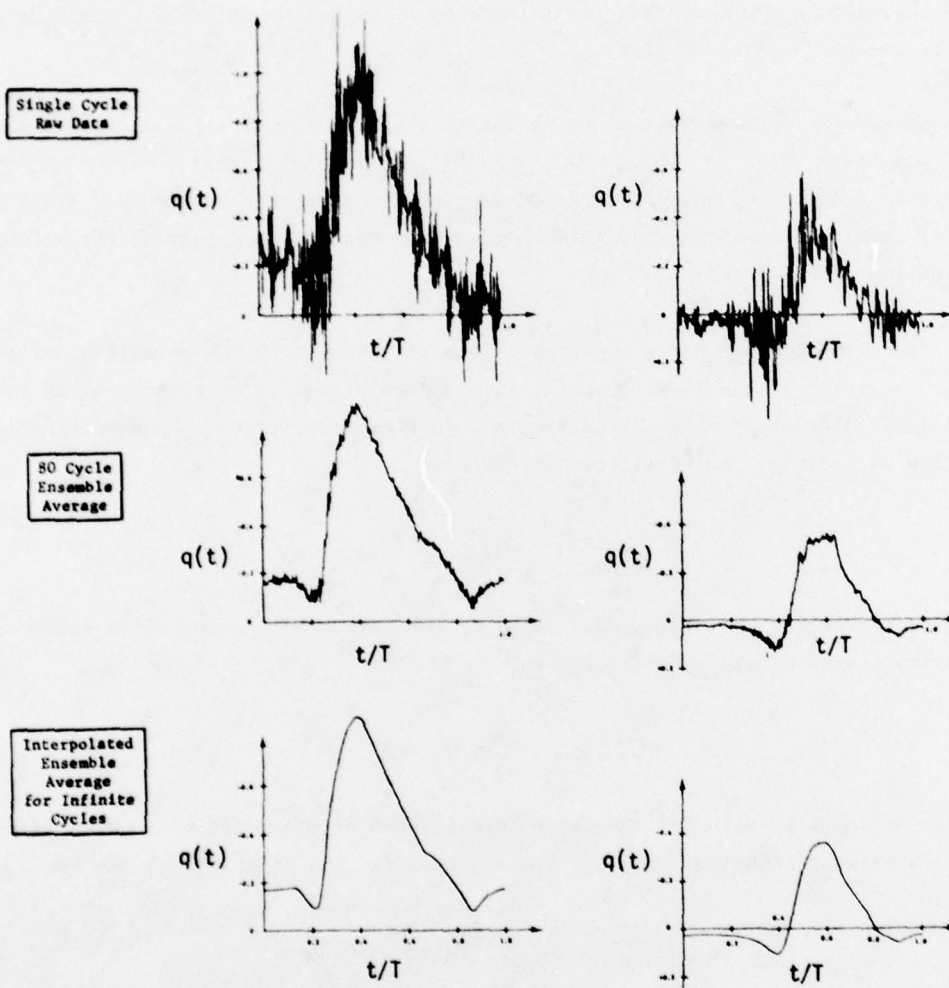Oscillation frequency, f = 8.2 Hz

Figure 1.   Comparison on Instantaneous Data Record with
Corresponding Ensemble Average

128

subsequent spatial integration around each contour requires that the individual temporal ensemble averages be stored for later examination as new measurements are taken. Since the mesh may involve a large number of elements, each itself a contour, there is a potential requirement for the handling of a massive amount of data, dictating a need for a digital computer-based data acquisition system.

To demonstrate the usefulness of the method, an experiment was constructed whereby an unsteady, separated flow was generated behind an oscillating fence-type spoiler on one surface of an airfoil (NACA 0012) in incompressible flow. The experiment was conducted in USAF Academy's .61 m (2 ft) x .91 m (3 ft) subsonic wind tunnel. The spoiler oscillation frequency could be fixed at values between 0-30 Hz. Spoiler mean height and amplitude could also be adjusted for a given series of measurements.

A multi-component constant temperature, linearized hot-wire anemometry system was employed for velocity field measurements in the region surrounding the reverse flow portion of the separation zone. An "x"-geometry probe was oriented to provide two orthogonal components of velocity in the integration plane. Analog output voltages directly proportional to the instantaneous velocity component magnitudes were then sampled by a PDP 11/45 data acquisition system. At each measurement location, data records having a length of one and one-half periods of oscillation were triggered into the computer by an inductive pickup whose pulsed output corresponded to a prescribed value of the spoiler height. This process had the effect of phase-locking the initiation of sampling to an event which corresponded to the periodic flow field drive. A general schematic of the experimental apparatus is presented in Figure 2.

The data reduction algorithm involves conversion of voltage to velocity, ensemble averaging as discussed above, and subsequent storage of the averaged data on disk. Each data set was tagged with the probe location and aerodynamic reference data (pressure, temperature, free stream velocity, etc.). The use of hot-wire anemometer probes presented certain limitations on the possible measurement locations due to the intermittent reversing nature of the flows. Data validation was, therefore, accomplished using both analog comparator circuits and a software-verification scheme in addition to flow visualization photographs. A complete discussion of these restrictions and the validation scheme is presented in the paper.

The probe was moved and accurately positioned by a motorized three-dimensional traversing mechanism having a continuous analog position output. Upon completion of the storage of each data set, program control was exercised to reposition the probe through a D/A converter voltage output. This voltage was employed to drive several sets of solid-state relays in a power distribution circuit. The data acquisition and repositioning process was accomplished until the entire contour sequence was completed.
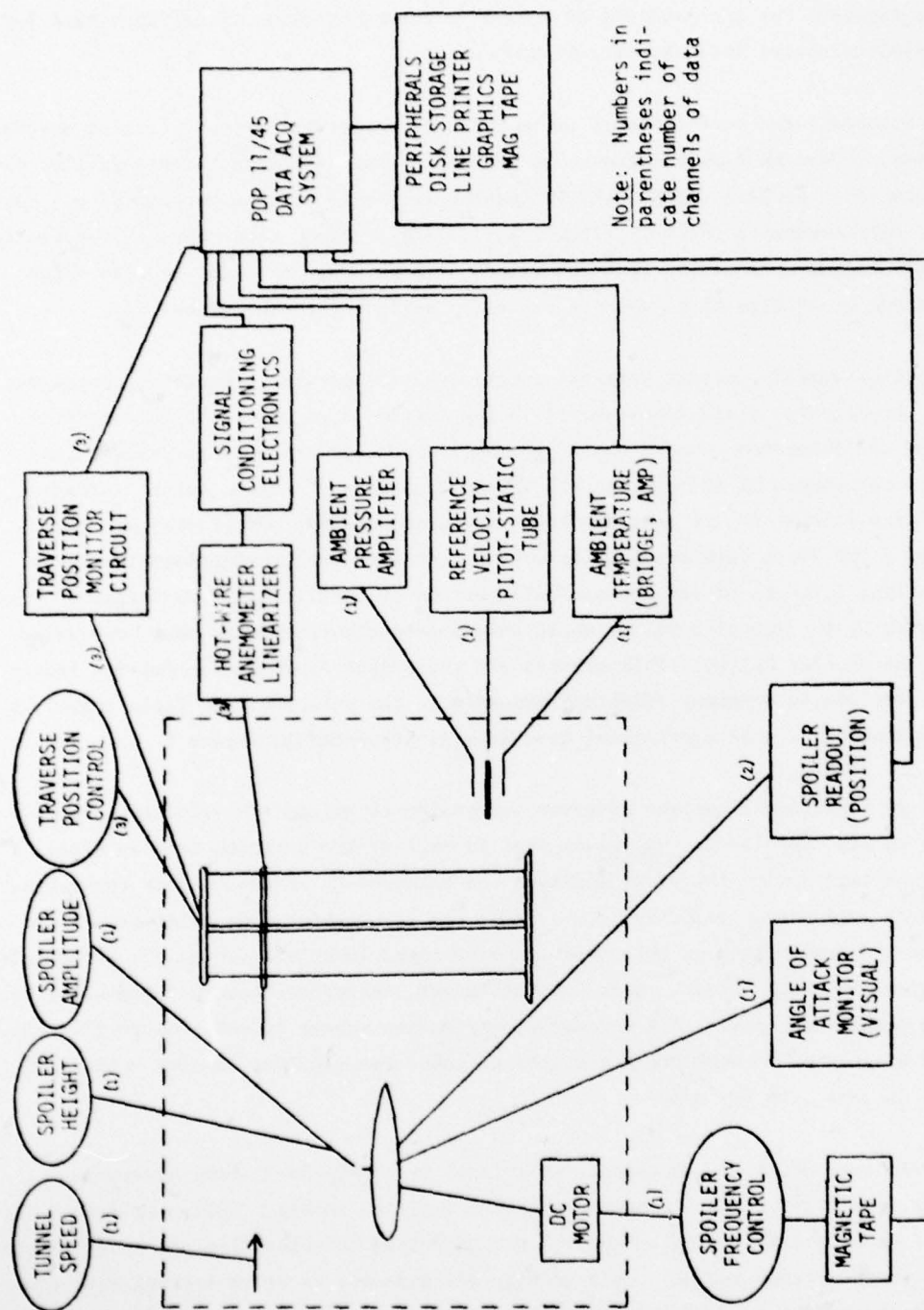
Figure 2. General Experimental Schematic

Finally, disk stored average data were recalled to core memory for the spatial integration calculations. Individual data points corresponding to common phase points of the oscillation were integrated to provide the circulation of various mesh elements at that time. Repetition of the integration procedure for other phase angles then provided the entire spatial and temporal distributions.

Results of preliminary measurements using this apparatus and technique are presented for a number of oscillation frequencies. A schematic of the rectangular mesh configuration is presented in Figure 3. Data from 225 separate locations were sampled for the 31 contour integrals. In the examples provided, between 25 and 100 records were used for the averages. Figure 4 displays the vorticity contained in the contour labeled "b" in Figure 3. Spatial distribution for given phase angles can then be obtained by suitable cross-plotting of these distributions. It is then possible to track regions of concentrated vorticity as they move spatially.

Tests currently being conducted employ a much finer mesh contour array and involve a laser doppler velocimeter for non-intrusive velocity measurements in the interior of the reverse flow separation vortex. These new measurements will also be discussed in the paper.

Results obtained to date indicate the capability of the method to accurately determine the vorticity distribution in a complex, unsteady flow. A major advantage of the technique is its ability to assess the average vorticity within a region without affecting measurements within it. The spatial resolution of resultant distributions is dictated by the minimum size of the individual contours which are employed. This factor is, in turn, often dictated as much by the capabilities of the available data acquisition system as by the nature of the flow itself.
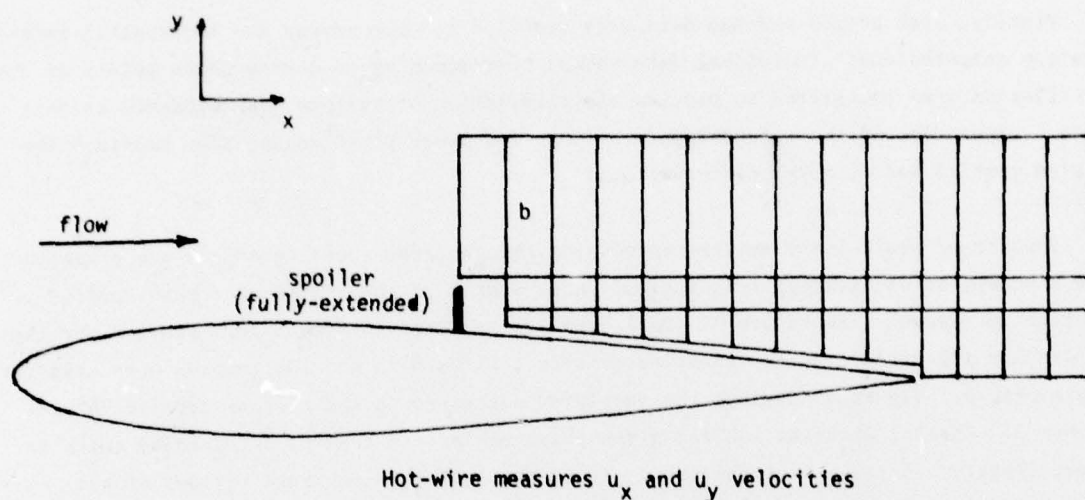
y ↑
└→ x

flow →

spoiler
(fully-extended)

b

Hot-wire measures u_x and u_y velocities

Figure 3. Typical Distribution of Spatial Contours (Course Mesh)

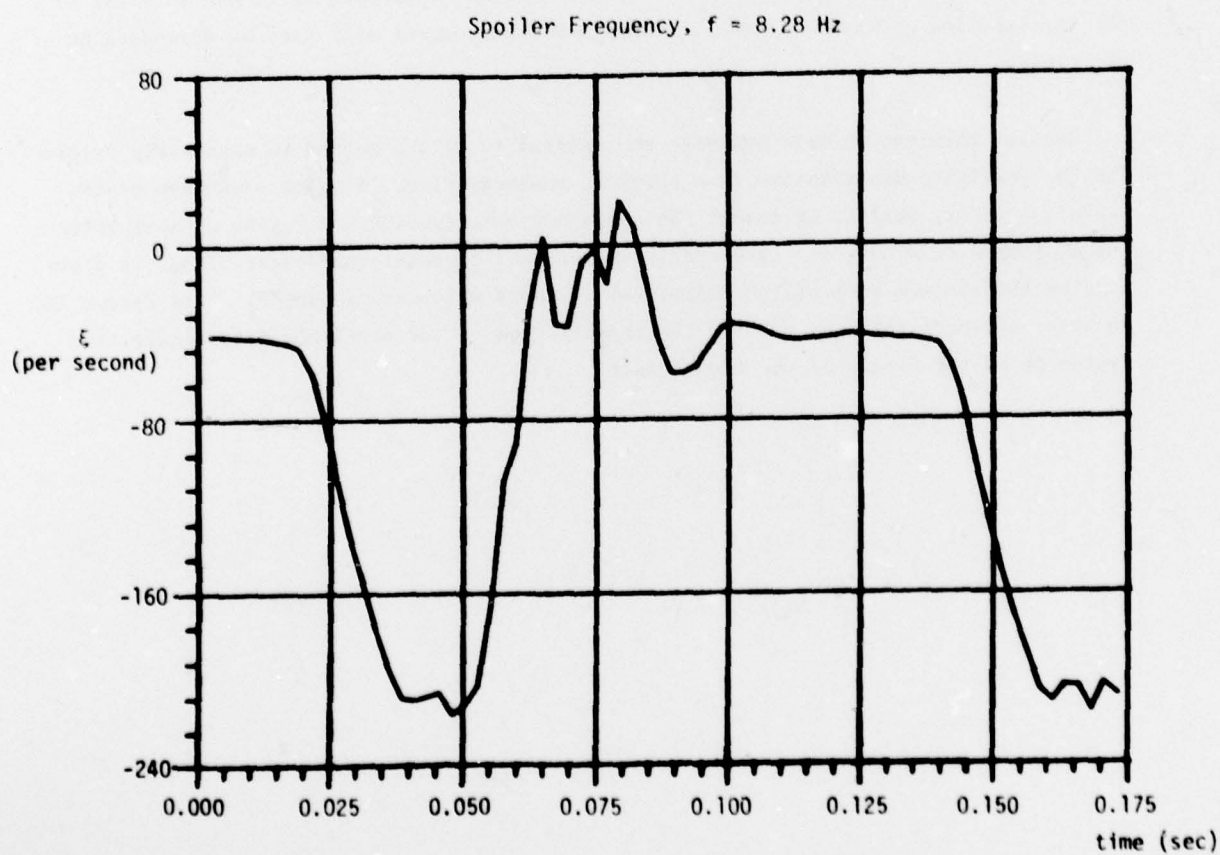Spoiler Frequency, f = 8.28 Hz

ξ
(per second)

time (sec)

Figure 4. Average Vorticity as a Function of Time
for an Individual Contour

132